8-2016

Ab initio based State Specific Modeling of N2+O System

Han Luo
Purdue University

Graduate School Form
30 Updated 12/26/2015

PURDUE UNIVERSITY
GRADUATE SCHOOL
Thesis/Dissertation Acceptance

This is to certify that the thesis/dissertation prepared

By Han Luo

Entitled

AB INITIO BASED STATE SPECIFIC MODELING OF N2+O SYSTEM

For the degree of Master of Science in Aeronautics and Astronautics

Is approved by the final examining committee:

Alina Alexeenko, Chair	Sergey O. Macheret
Jonathan Poggie	

To the best of my knowledge and as understood by the student in the Thesis/Dissertation Agreement, Publication Delay, and Certification Disclaimer (Graduate School Form 32), this thesis/dissertation adheres to the provisions of Purdue University's "Policy of Integrity in Research" and the use of copyright material.

Approved by Major Professor(s): Alina Alexeenko

Approved by: Weinong Wayne Chen 7/7/2016

Head of the Departmental Graduate Program Date

AB INITIO BASED STATE SPECIFIC MODELING OF N2+O SYSTEM

A Thesis

Submitted to the Faculty

of

Purdue University

by

Han Luo

In Partial Fulfillment of the

Requirements for the Degree

of

Master of Science in Aeronautics and Astronautics

August 2016

Purdue University

West Lafayette, Indiana

Dedicated to my parents,
Chen, Guimei and Luo, Hongwei
for their support of my growth

ACKNOWLEDGMENTS

During the pursuing of M.S. degree, there are many people providing important support for me. First of all, I would like to express my appreciations to my parents and friends. They provided an emotional anchor for me and helped me get out of the loneliness of studying abroad.

I would like to thank my advisor, Prof. Alina Alexeenko, for introducing me into the field of particle-based simulation methods and helping me study nonequilibrium gas dynamics. Her invaluable guidance opened the door of professional research for me. I also need to thank Prof. Sergey Macheret and Prof. Jonathan Poggie for providing invaluable ideas for my thesis and helping me to finish my work better.

Dr. Marat Kulakmetov needs to be acknowledged for his instructions on quasi-classical trajectory method and uncountable discussions on hypersonic aerodynamics, nonequilibrium gas dynamics and etc. He also taught me a lot about American culture and history which helped me to get integrated into the new life.

I am also grateful to my other lab mates, Andrew Strongrich, Dr. Andrew Weaver, Bill O'Neill, Cem Pekardan, Devon Parkos, Gayathri Shivkumar, Israel Sebastiao, Siva Tholeti and Dr. Tony Cofer for their support and countless valuable conversations. In particular, I would like to thank Israel Sebastiao for discussions on DSMC models and Devon Parkos for many fundamental theoretical problems.

TABLE OF CONTENTS

Page

LIST OF TABLES

LIST OF FIGURES

Figure Page

SYMBOLS

E_c	Total Energy
E_a	Activation energy
E_d	Dissociation energy
E_{rv}	Rovibrational energy
E_v	Vibrational energy
v	Vibrational level
J	Rotational level
N_i	Number density of state i
T	Equilibrium temperature
T_r	Rotational temperature
T_t	Translational temperature
T_v	Vibrational temperature
V_r	Relative velocity
V	Potential energy
Z	Nonequilibrium factor
g_n	Nuclear degeneracy
g_{elec}	Electronic degeneracy
g_J	Rotational degeneracy
k	Boltzmann constant
k_D	Dissociation reaction rate
k_{EX}	Exchange reaction rate
v'	Post collision vibrational level
μ	Reduced mass
χ	Scattering angle
b	Impact parameter

b_{max}	Maximum impact parameter
τ_v	Vibrational time constant
σ_r	Cross-section for process r
f	Distribution function

ABBREVIATIONS

CFD	Computational Fluid Dynamics
COM	Center of Mass
DSMC	Direct simulation Monte Carlo
FHO	Forced harmonic oscillator model
GCE	Generalized collisional energy model
LB	Larsen-Borgnakke model
MC	Monte Carlo
ME	Maximum Entropy model
ME-QCT	QCT-informed maximum entropy model
ODE	Ordinary differential equations
PES	Potential energy surface
QCT	Quasi classical trajectory
RK	Runge-Kutta
SSE	State-specific exchange
SSD	State-specific dissociation
TCE	Total collision Energy model
UV	Ultra-violet
VHS	Varible hard sphere model
VFD	Vibrationally-favored dissociation model
VT	Vibrational-translational transition
VRT	Vibrational-rotational-translational transition

ABSTRACT

Luo, Han M.S.A.A.E., Purdue University, August 2016. Ab initio based State Specific Modeling of N2+O System. Major Professor: Alina Alexeenko.

Nitrogen and atomic oxygen play an important role in high temperature gas systems. Their Zeldovich reaction product nitric oxide not only affects aerothermal loads and emissions of hypersonic vehicles, but also has the possibility to influence the efficiency of hypersonic propulsion. Atomic oxygen induced nitrogen dissociation is another reaction mechanism of the $N_2 + O$ system. However, due to the difficulty of conducting ground tests, there are no experimental data for this reaction now. Thermo-chemical nonequilibrium could make the problem more difficult since experiments could only track macroscopic gas properties instead of internal energy distribution. On the other hand, current reaction and internal energy exchange models are able to reproduce equilibrium condition. Whether their predictions at nonequilibrium conditions are reliable is still questionable. The work in this thesis employs quasi-classical trajectory (QCT) method based on an *ab-initio* chemistry calculated potential energy surface for the $N_2 + O$ system. Through QCT calculations of different initial condition, high fidelity cross sections and rates are obtained. The cross sections are further used to generate a ME-QCT-VT model for vibrational excitation/relaxation, a state-specific exchange (SSE) model and a state-specific dissociation (SSD) model. These models are verified by comparison with direct QCT calculated rates and other experimental data or models. Although there are no flowfield calculations in this work, the models are able to be applied easily in DSMC calculations.

1. INTRODUCTION

1.1 Background

High temperature gas dynamics has become one major concern in aerodynamics since the first rocket was launched. Considering a earth re-entry vehicle flying at an altitude of 53 km with Mach number 32.5, a shock-layer temperature of 11,600K can be estimated if local chemical equilibrium is assumed. [1] The massive kinetic energy of hypervelocity freestream passing through the shock is rapidly converted to internal translational energy of the molecules, which creates the high temperature. Once the molecules gain enough energy, translational energy can be transfered to rotational, vibrational and electronic energies through molecular collisions. In Fig.1.1, the temperature range of different molecular collision mechanisms is shown. Although there is no reaction at temperature around 800K, the vibrational excitation could lower translational temperature. Once the temperture becomes higher than 2500K, dissociation reactions take place from vibrationally excited states and continue driving the temperature down. Finally, the system can be equilibrated if the gas has enough time for the necessary collisions to occur. However, there are some cases that the system could not reach thermal equilibrium, 1) dissociation and exchange reaction rates approach convection mass transport rates and thermo-chemical nonequilibrium is generated as observed in Martian returning [2]; 2) high speed freestream condition or small geometries like a sharp leading edge results in a nonequilibrium region before gas comes to equilibrium [3]; 3) inadequate molecular collisions due to low number density. Therefore, state-specific rates and cross sections are needed to accurately model flows with such nonequilibrium. Since measurement of state-specific rates experimentally remains difficult and the exisiting equilibrium reaction rates data mainly comes from flight test or shock tube experiments conducted in last century, most cur-

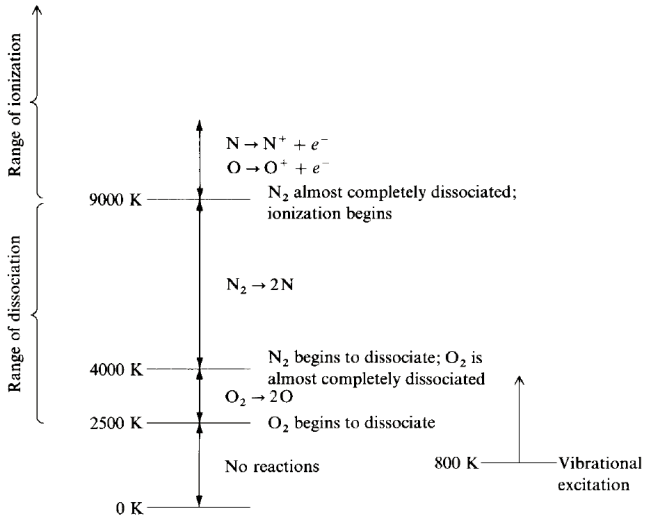

Figure 1.1. Ranges of vibrational excitation, dissociation and ionization for air at 1atm pressure. Taken from Ref. [1]

rently used nonequilibrium models are still phenomenological. These models were designed to reproduce reaction rates at equilibrium conditions and equilibrium post collision energy distribution. Their accuracy at nonequilibrium conditions is questionable. Quasi-classical trajectory calculations(QCT), based on accurate *ab-initio* potential energy surfaces (PES), have recently made it possible to calculate complete set of state-specific energy exchange cross sections. [4, 5] Researchers used these cross sections directly or reduced them to compact models for use in computational fluid dynamics (CFD) [6,7] and direct simulation Monte Carlo (DSMC) calculations [8–13].

In this work, the main motivation comes from the lack of state-specific models for $N_2 + O$ system. There are two reaction mechanisms for the system. One is the atomic oxygen induced dissociation reaction of nitrogen:

$$N_2(v, J) + O \rightarrow 2N + O. \tag{1.1}$$

the other is the Zeldovich exchange reaction:

$$N_2(v, J) + O \rightarrow NO(v', J') + N, \tag{1.2}$$

The nitrogen dissociation reaction is approximately a factor of three higher in collisions with atomic oxygen than in collisions with molecular oxygen or nitrogen. [14] Since the nitrogen dissociation energy is 9.8 eV while the oxygen dissociation energy is 5.2 eV, molecular oxygen is expected to be fully dissociated and the concentration of atomic oxygen should be significant by the time nitrogen starts dissociating. In addition, atomic oxygen can also be generated at low temperature through the dissociative attachment of low-energy plasma electron. [15] Therefore the dissociation reaction may have a significant contribution toward dissociating nitrogen in high temperature air flows. Despite its importance, this reaction has not been experimentally measured at high temperature conditions, to the best of authors' knowledge. The rate used to describe this reaction is typically extrapolated from rates of other reactions. [14, 16].

Although two diatom-atom Zeldovich exchange reactions have been identified as the primary sources of NO formation in air flows, the mechanism in reaction 1.2 is expected to be more significant at temperature higher than 4000K, where molecular oxygen is almost fully dissociated and concentration of atomic oxygen is high. Levin *et al.* [17] and Boyd *et al.* [18] have used CFD calculations and DSMC method with vibrational favored dissociation model to show that NO concentration in shock layers is highly sensitive to concentrations of atomic oxygen. NO is one of the significant gas species for hypersonic flow. NO formed in hypersonic shock layers is a critical source of ultraviolet radiation and it strongly contributes to reentry vehicle heating. [19] It can be ionized to NO^+ during re-entry at temperature ranging from 4000K to 6000K, which creates a plasma sheath and results in radio frequency blackout. Recent calculations by Parkos *et al.* [20] also suggest that NO formed in the wakes of hypersonic reentering spherules may have contributed toward the marine extinction at the end of the Cretaceous Period. Besides hypersonic re-entry, Cabell and Rock found that NO contamination has the possibility to increase thrust performance of scramjet by up to 10%. [21]

Early high temperature QCT calculations for the Zeldovich reaction were performed by Bose and Candler and they modeled the energy disposal mechanism for this reaction. [22, 23] These calculations were then used in CFD simulations of hypersonic flows. [24] Boyd *et al.* [25] calibrated the coefficients of generalized collisional energy model based Bose and Candler's QCT results and applied to the DSMC simulation of BSUV-2 flight condition. Wysong *et al.* [9] directly used the tabulated QCT results. Both of their DSMC calculations observed clear discrepancies between established phenomenological DSMC reaction models and QCT-calculated cross sections. Aknipar *et al.* [26] calculated a reduced set of state-specific cross sections for reaction 1.2 using both QCT and quantum wave packets method produce comparable results at hypersonic flight-relevant conditions. Armenise and Esposito [27] extended earlier calculations to include full state-specific exchange and state-to-state transition rates. Their CFD calculations of a hypersonic boundary layer with state-specific rates showed the importance of NO to N_2 and O_2 mass fraction and heat flux. Most of the recent work with reaction 1.2 focused on verifying already established models against QCT calculations. However, the QCT-calculated cross sections have not been made easily available to the research community or fit to high-fidelity models that can be adapted to CFD and DSMC calculations of highly nonequilibrium flows.

1.2 Thesis Object and Structure

The main goal of this thesis is to study $N_2 + O$ collision dynamics and build state-specific models for high temperature $N_2 + O$ system, that are able to be applied to DSMC and CFD calculations directly. The structure of the remaining parts is the following. In Chapter 2, the methodology of the work is presented. A brief introduction of ab-inito quantum chemistry in given, followed by a detailed comparison of current available potential energy surfaces for $N_2 + O$ system and the computation of rovibrational ladder of reactant molecule N_2 and product molecule NO. An introduction of procedures in the QCT code developed by Kulakhmetov [28] is latter given.

Studies related to convergence, accuracy and special treatment for electronic nonadiabtic transition are also shown. In Chapter 3, studies of equilibrium reaction rates, state-specific reaction rates, exchange cross sections, relaxation time and collisional dynamics are presented. These studies provide preliminary ideas of state-specific model and verify the calculations at the same time. In Chapter 4, ME-QCT-VT [28] model for vibrational excitation/relaxation, state-specific exchange (SSE) model for exchange reaction and state-specific dissociation (SSD) model for dissociation reactions are built based on QCT calculation results. These models could provide high-fidelity state-to-state VT transition cross sections and state-specific reaction cross sections with limited number of coefficients. The models are verified by comparing the integrated equilibrium, non-equilibrium and state-specific rates with direct QCT calculation results and other models, which implies the ability to use integrated rates in CFD calculation.

2. METHODOLOGY

In this chapter, the methodology of *ab-initio* based calculation is presented. A flowchart is shown in Fig.2.1. There are mainly three parts of the work including *ab-initio* quantum chemistry calculation, quasi-classical trajectory calculation, and flowfield calculation. They are introduced in the following sections.

2.1 Ab-initio Quantum Chemistry Calculation

An accurate multi-body potential energy surface (PES) is the foundation of molecular collision calculations. It serves to mediate the reaction product and reactants or the initial molecule and collision induced excited/relaxed molecules. Fundamentally, time independent Schrödinger equation is used to describe the particles' interaction,

$$\mathbf{H}\Psi(R,r) = E\Psi(R,r), \tag{2.1}$$

where $\Psi(R,r)$ is the total wave function, E is the energy eigenvalue, R is nuclear coordinates and r is electronic coordinates. $\mathbf{H}$ is the Hamiltonian of the system calculated as:

$$\mathbf{H} = \mathbf{T_e} + \mathbf{T_n} + \mathbf{V_{nn}} + \mathbf{V_{ne}} + \mathbf{V_{ee}}, \tag{2.2}$$

where $\mathbf{T_e}$ and $\mathbf{T_n}$ are the kinetic energy of nuclei and electrons, $\mathbf{V_{ne}}$, $\mathbf{V_{nn}}$ and $\mathbf{V_{ee}}$ are the Coulumb interaction of nuclei-electron, nuclei-nuclei and electron-electron. Considering the number of variables for Schrödinger equation is determined by the amount of electrons and nuclei, it's hard to solve it directly in most cases. The Born-Oppenheimer approximation [29] is usually applied, which assumes the coupling between the nuclear and electronic velocities can be neglected. [30] Thus nuclei are

stationary in the viewpoint of electrons and the electronic Schrödinger equation Eq.2.3 is first solved,

$$[\mathbf{T_e}(r) + \mathbf{V_{ee}}(r) + \mathbf{V_{ne}}(R, r) + \mathbf{V_{nn}}(R)]\Psi_e(r, R) = E_e(R)\Psi_e(r, R). \tag{2.3}$$

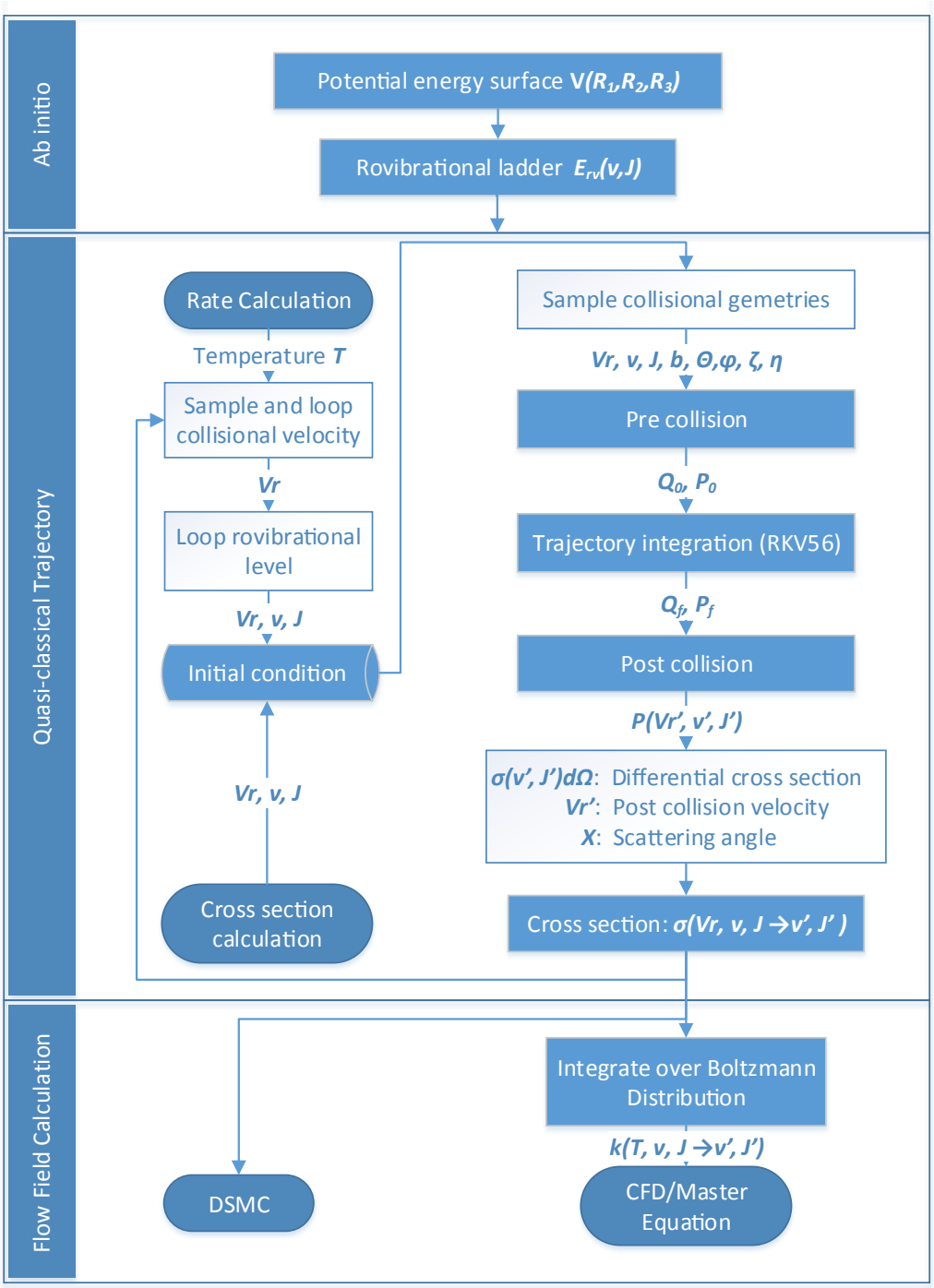

Figure 2.1. Methodology of *ab-initio* based calculation

The energy eigenvalue E_e depends parametrically on nuclear coordinates R now. Due to the multi-dimension property of the electronic wavefunction, it's hard to solve it directly. Usually, the electronic wavefunction is represented in certain finite basis sets and the Schrödinger equation is transformed to algebraic equation which can be solved numerically. By solving E_e for different discrete nuclear coordinates, the PES which governs the energy transfer mechanism of the atomic collision can be generated. Detail introduction of the PES of $N_2 + O$ will be presented in Sec.2.1.1.

Once the PES is generated, the motion of nuclei can be solved by either quantum mechanics calculation or quasi-classical trajectory (QCT) calculation. The idea of quantum mechanics calculation is to solve the time independent Schrödinger equation,

$$[\mathbf{T_n} + E_e(R)]\Psi_n(R) = E_{tot}(R)\Psi_n(R). \tag{2.4}$$

For atom-molecule collision, the total wave function at large separation can be expressed as [31]:

$$\begin{aligned}\Psi(r_1, r_2, E) = &\left(\frac{k_{vJ}\mu}{2\pi h^2}\right)^{\frac{1}{2}} [e^{ik_{vJ}Z}\chi_{vJ}(r_1)Y_{j,m_j}(\theta_{r_1}, \phi_{r_1}) \\ &+ \sum_{v'j'm'_j} f_{vJm_j\to v'J'm'_j}(\theta_{r_2}, \phi_{r_2})\frac{e^{ik_{v'J'}r_2}}{r_2}Y_{j',m'_j}(\theta_{r_1}, \phi_{r_1})].\end{aligned} \tag{2.5}$$

In general, the first term represents the initial incident wave function and the second term is an expansion of scattered wave going radially outwards from the scattering center. Once the wave function is solved, the inelastic differential cross sections can be calculated by:

$$\sigma_{vJm_J\to vJm_J}(\theta_{r_2}, \phi_{r_2}, E)\mathrm{d}\Omega = \frac{k_{v'J'}}{k_{vJ}}\left|f_{vJm_j\to v'J'm'_j}(\theta_{r_2}, \phi_{r_2})\right|^2. \tag{2.6}$$

It should be noticed that although quantum closed coupling calculation is more accurate since it could take tunneling effect and resonance phenomena into consideration, the computational load is high since all rovibrational transition are calculated and the load is increased with higher collisional energy. [32] QCT is a more appropriate method for engineering high enthalpy flow. It solves Halmilton's equantion with

the same Hamiltonian as Eq.2.4. A detail comparison of QCT and quantum calcultion of $H + HeH^+$ shows that a good agreement of integral cross sections can be obtained for collisional energy higher than 0.1eV with 1/3 of computational load and QCT produces equilibrium and state-specific rates accurately for temperature down to 300-2000K. [32] Detail introduction of QCT method will be presented in Sec.2.2.

Besides the PES, an accurate rovibrational ladder is another quantum mechanical information needed for QCT calculation. It requires a radial one-dimensional Schrödinger equation to be solved:

$$-\frac{\hbar^2}{2\mu}\frac{d^2\Psi_{v,J}(r)}{dr^2} + V(r)\Psi_{v,J}(r) = E_{v,J}(r), \tag{2.7}$$

where $V(r)$ is the potential energy of the molecule N_2 and NO, μ is the reduced mass, and $E_{v,J}$ is the rovibrational ladder. LEVEL program is employed in this work to obtain the ladder for the two kind of molecule. [33]

2.1.1 Potential Energy Surface for $N_2 + O$ System

For molecule nitrogen and atomic oxygen collision, there are three collisional mechanism, including inelastic transition:

$$N_2(v, J) + O \rightarrow N_2(v', J') + O, \tag{2.8}$$

exchange reaction:

$$N_2(v, J) + O \rightarrow NO(v', J') + N, \tag{1.2 revisited}$$

and dissociation reaction:

$$N_2(v, J) + O \rightarrow 2N + O. \tag{1.1 revisited}$$

An *ab-initio* based PES for $N_2 + O$ system is needed for accurate QCT calculations. A detailed description of adiabatic correlation diagram for the $N_2 + O$ system can be found in Ref. [34]. Part of the correlation diagram from Ref. [35] is shown in Fig.2.2. We are focused on the reactants at ground electronic state, i.e. $O(^3P)$ and $N_2(X^1\Sigma_g^+)$

as the ground level products are only correlated with them. As it can be found in Fig.2.2 one third of collisions proceed on the $^3A''$ PES and another third on $^3A'$ PES. Both of these surfaces adiabatically correlate to the N(^4S) and NO($X^2\Pi$) products. The remaining one third of collisions proceed on the $2^3A''$ surface and produce N(^2D) and NO($X^2\Pi$) products. The exchange reaction on this surface requires collision energy above 5.637 eV, compared to the 3.263 eV required by the prior surfaces. We ignore the $2^3A''$ in our work because it is less likely to produce the NO($X^2\Pi$) products.

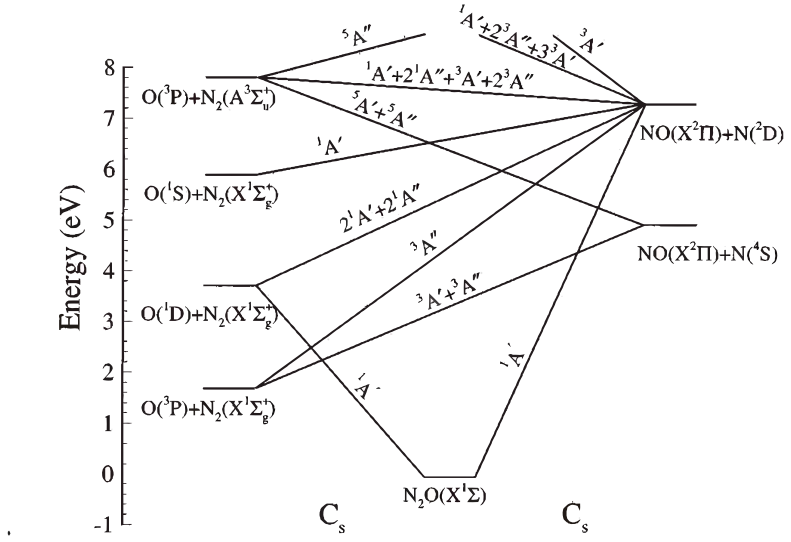

Figure 2.2. Partial correlation diagram of $N_2 + O$ system. Energies of N_2O electronic states are not shown for simplicity. Figure taken from Ref. [35] FIG 1.

The PES of $^3A''$ and $^3A'$ have been calculated by many researchers. We primarily analyze the work done by Walch and Jaffe [36], Gamallo *et al.* [37, 38] and Lin *et al.* [39].

Walch and Jaffe employed a complete active space SCF followed by a dynamic correlation using a multi-reference contracted configuration interaction method in the calculations. They focused on the saddle point in the NO + O channel. It was first found that there is no barrier for the $^3A''$ surface and the reaction favors collinear

collision channel. Analytical fits of $^3A''$ and $^3A'$ were obtained by Gilibert *et al.* [40] and Bose and Candler [23] separately using a Sorbie-Murrell function [23]. Gamallo *et al.* used a complete active-space self-consistent-filed wave function (CASPT2) [37,38]. The stationary points for the two lowest $N_2O(^3A'',^3A')$ triplet state were fit to analytical many-body expansion expressions. These PESs have been verified by variational transition-state theory(VTST) [37, 41], QCT [26, 37, 42] and quantum wavepacket calculations [26, 43, 44]. Lin *et al.* published new PESs for $^3A''$ and $^3A'$ surfaces in 2016 before this work was done. [39] They obtained the reference electronic wave function by dynamically weighted state-averaged complete-active-space self-consistent field (SA-CASSCF) calculations involving the three lowest-energy states of each symmetry. Dynamical scaling of external correlation method was used to improve the accuracy of the PESs. The calculated PESs were fit to a functions composed by sum of pairwise terms and permutationally invariant polynimials in bond orders. Due to the complexity of PESs, the analytical expressions of the PESs are not presented here. We'll focus on the comparison of some features of the PESs.

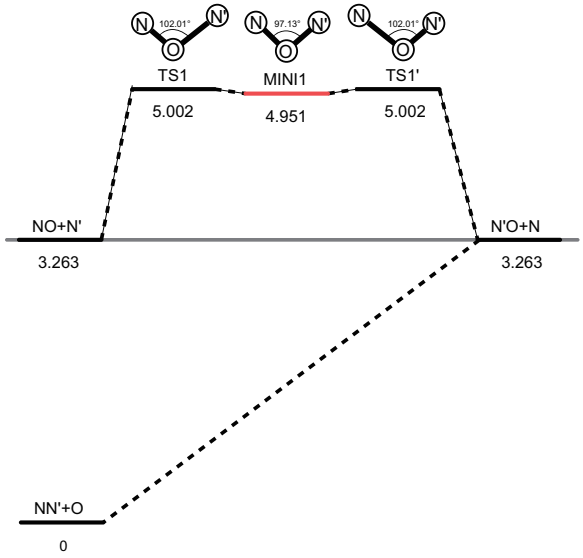

Figure 2.3. Energy Diagram and MEP for Gamallo *et al.*'s $^3A''$ PES. The energies are given in eV with relative to reactant $N_2 + O$

Table 2.1. Properties of stationarity points on the $^3A''$ and $^3A'$ PESs

PES	Source	E[a]	R_{NO} [b]	$R_{N'O}$	$R_{NN'}$	$\angle N'ON$ or $\angle N'NO$
$^3A''$						
MINI1'(C_s)	Walch	-6.5944	1.4190		2.1707	108.9°
MINI1(C_{2v})	Gamallo	-4.85676	1.322	1.322		97.1°
	Lin	-4.81775	1.321	1.321		109.5°
TS1(C_s)	Gamallo	-4.80472	1.3965	1.2609		102.01°
	Lin	-4.76875	1.460	1.239		109.5°
$^3A'$						
MINI1(C_s)	Lin	-8.178906	1.287		1.211	123.0°
TS2(C_s)	Walch	-5.9944	1.1695		1.8913	116.5°
	Gamallo	-6.25527	1.157		1.976	115.2°
	Lin	-6.16161	1.165		1.870	115.3°
MINI3(C_{2v})	Gamallo	-5.95734	1.2921	1.2921		114.13°
	Lin	-6.01243	1.290	1.290		125.4°

[a] Energies are given relative to 2N+O dissociation asymptote with unit eV

[b] All distance R is given in unit Angstrom Å

A comparison of the PESs for $^3A''$ surface with collinear configuration is shown in Fig.2.5. It can be found that there is an energy barrier at the NO+N exiting channel. It is expected that vibrational excitation will help to break the energy barrier. [45]. However, both Gamallo *et al.*'s and Lin et al.'s PESs predict an earlier appearance of the barrier than Walch and Jaffe's which may result in higher reaction probability for collinear collisions. An energy diagram of Gamallo *et al.*'s $^3A''$ PES for minimum energy path(MEP) is presented is Fig.2.3. A similar one for Lin *et al.*'s PES can be found in Ref. [39]. There are two mechanisms that can produce the exchange reaction (1.2). The first is through the N-abstraction channel, which has an energy barrier equivalent to the endothermicity. The other one is O-insertion channel, in which the

reaction proceeds through MINI1 and TS1 configuration. The energy barrier for this second mechanism is approximately 5 eV. The atomic positions for MINI1(C_{2v}) and TS1 (C_s) configuration are shown in Table 2.1. A comparison of the $^3A''$ PES with these two configurations is presented Fig.2.6. It can be found that Walch and Jaffe's PES doesn't have the saddle points as other PESs. Instead, there is an energy barrier around 6 eV on NO + N exiting channel. The lack of O-insertion mechanism makes the reaction probability lower, which will be proven in the comparison of earlier QCT studies [22, 40] and our results.

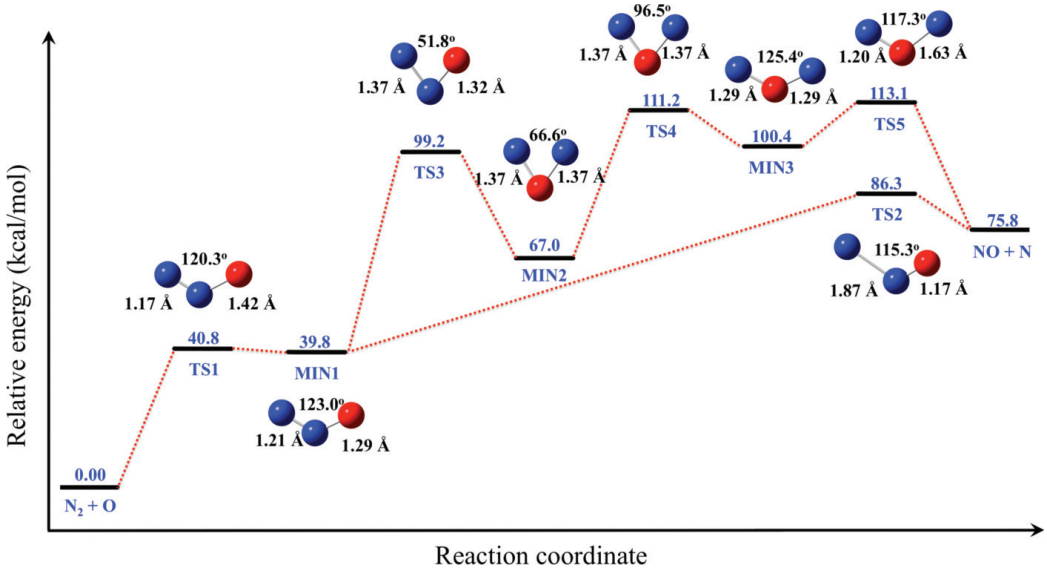

Figure 2.4. Energy Diagram and MEP for Lin *et al.*'s $^3A''$ PES. The energies are given in kcal/mol with relative to reactant $N_2 + O$. Cited from Ref. [39]

An energy diagram of Lin *et al.*'s $^3A'$ PES is shown in Fig.2.4. Some configurations are listed in Table 2.1. The PESs along MEP are presented in Fig.2.7. It can be found that all PESs show the existence of an energy barrier at TS2 configuration along MEP. The barrier is on the exiting channel thus it's expected larger vibrational energy will help exchange reaction proceed. Gamallo *et al.*'s PES predicts the value of barrier 1eV lower than others. In addition, Lin et al.'s *ab-initio* calculation found a MINI1 and TS1 on the entrance-channel. The energy barrier is around 0.2eV. It is unclear

how much difference it makes for the exchange reaction and collisional mechanisms since there is no QCT or quantum mechanics calculation based on this PES now as far as the author knows.

Although both $^3A'$ and $^3A''$ surfaces contribute to the reactions, the $^3A''$ surface is the dominant one as the ratio of electronically adiabatic exchange reaction rates, $k(^3A'')/k(^3A')$, for the two surfaces was reported ranging from 2 to 15 for different temperature. [22,37]. Therefore, only the $^3A''$ PES is considered in this work. Gamallo *et al.*'s PES is used. Calculations based on Lin *et al.*'s PESs can be done in the future to figure out new collisional mechanisms.

2.1.2 Rovibrational Ladder of N_2 and NO

The rovibrational energy ladder, used in this work, is calculated by the LEVEL program [33] using WKB method. The energy levels gotten are almost identical to those reported by Armenise and Esposito. [27] There are in total 60 vibrational states for N_2 and 53 vibrational states for NO. The WKB solutions of rovibrational energy ladders are fit to the following form:

$$E_{rv}(v,J) = E_v(v) + a_1(v,J)\cdot J(J+1) + a_2(v,J)\cdot J^2(J+1)^2 + a_3(v,J)\cdot J^3(J+1)^3 \quad (2.9)$$

where v and J are vibrational and rotational level. The vibrational energy E_v and parameters a_1, a_2, a_3 are in unit eV. The highest vibrational state $v = 60$ of N_2 doesn't exist classically in QCT. Maximum rotational levels and coefficients a_1, a_2, a_3 are tabulated in the appendix.

2.2 Quasi-Classical Trajectory

Quasi-classical trajectory method is a kind of classical description of nuclear collisional mechanism. In stead of solving Schrödinger equation, it treats the collisional particles as macroscale objects without internal structures and solves their motion under the interaction of potential energy. The following conditions need to be met

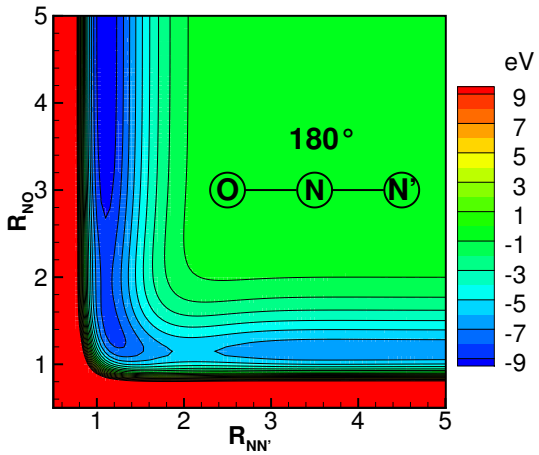

(a) Walch and Jaffe's PES [36]

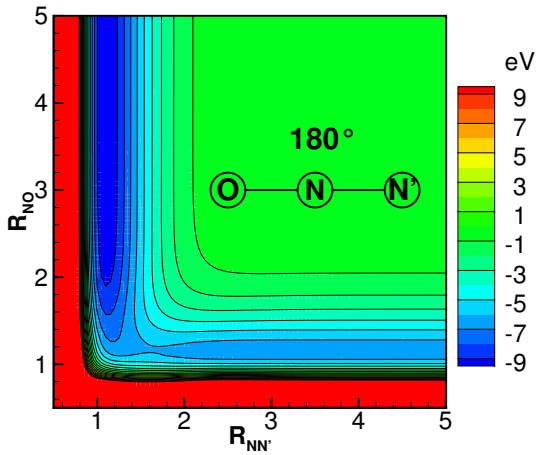

(b) Gamallo *et al.*'s PES [37]

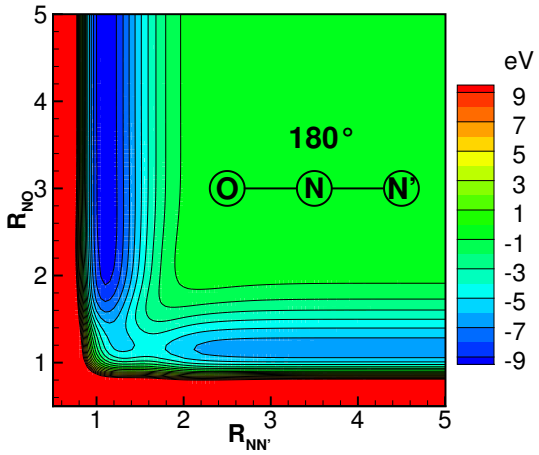

(c) Lin *et al.*'s PES [39]

Figure 2.5. Comparison of $^3A''$ PESs with collinear configuration

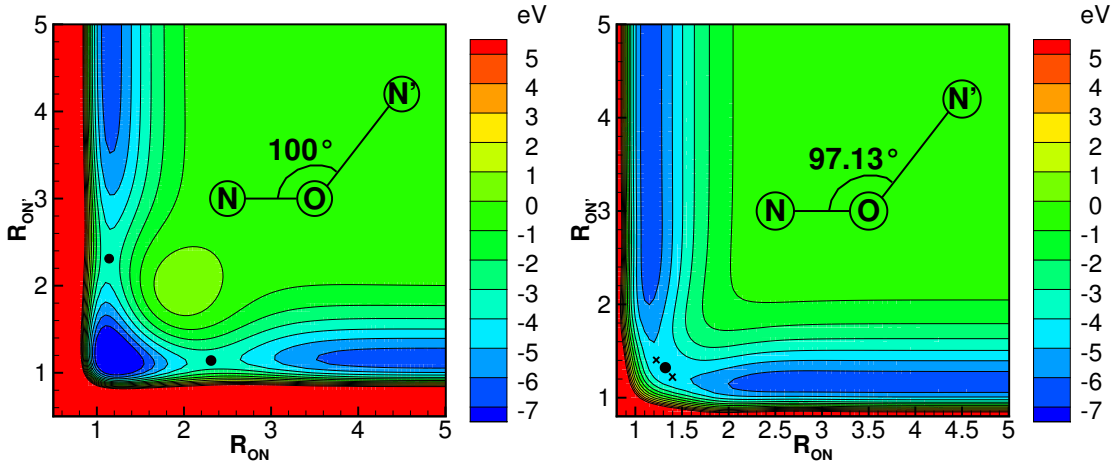

(a) Walch and Jaffe's PES [36]

(b) Gamallo *et al.*'s PES [37]

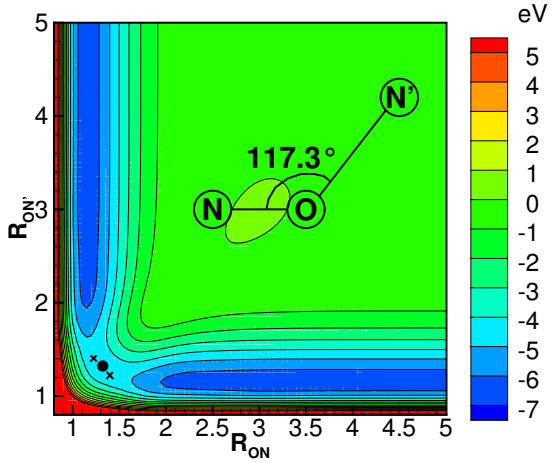

(c) Lin *et al.*'s PES [39]

Figure 2.6. Comparison of $^3A''$ PESs with MINI1(C_{2v}) configuration. The bending angle $\angle$NON$'$ for Walch and Jaffe's PES is chosen arbitrarily . Symbol $\bullet$ is MINI1 point and $\times$ is TS1 point.

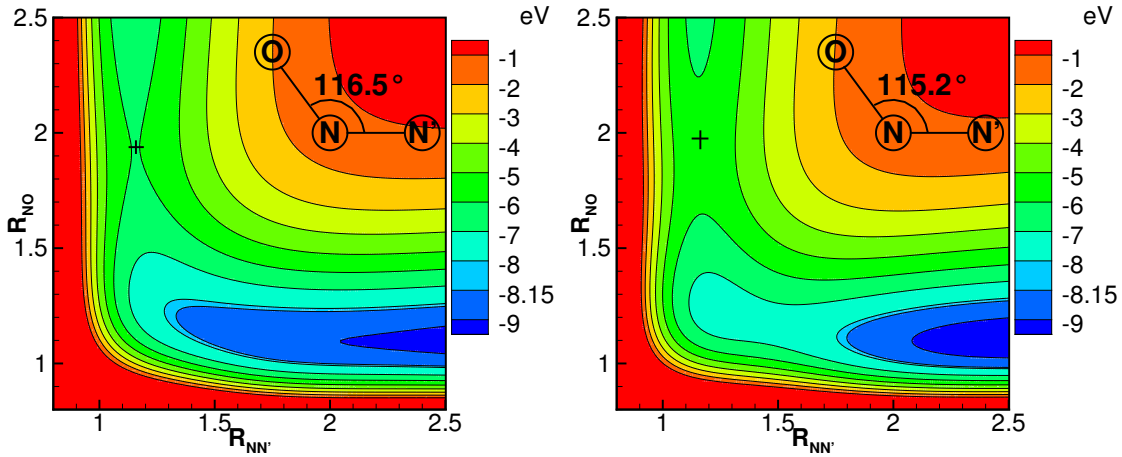

(a) Walch and Jaffe's PES [36]

(b) Gamallo *et al.*'s PES [37]

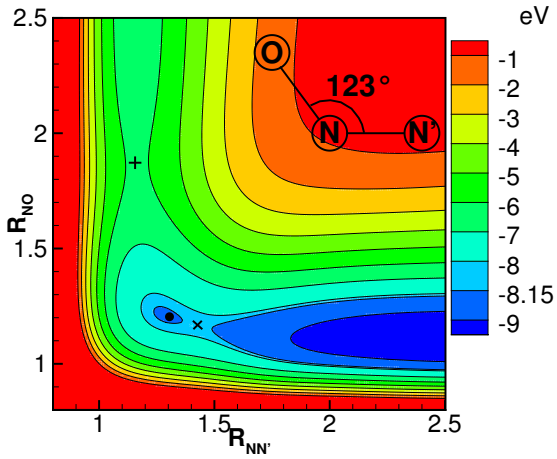

(c) Lin *et al.*'s PES [39]

Figure 2.7. Comparison of $^3A'$ PESs with C_s configuration along MEP. Symbol definition: •: MINI1; ×: TS1; +:TS2

to make QCT calculation results approximate the full quantum calculation: (1) the wave nature of the internuclear motion can be neglected (2) the desired information is highly averaged, (3) for calculation of reaction cross sections, the total energy of reactants should be much larger than the energy barrier to make sure the tunneling effect is not significant, (4) the importance of quantum interference phenomena should be small for transition. [5] We can check the validity of the conditions quantitatively by comparing de Broglie wavelength with the characteristic length of the PES. In table.2.2, the ratios of de Broglie wavelength to the equilibrium interatomic distance are presented for NO and N_2 molecule. It could be found for velocity higher than $3\,km/s$, the ratio is smaller than 0.1. Considering $3km/s$ is the most probable velocity for temperature around 5000 K, it is expected QCT is valid for T$>$ 5000K.

Table 2.2. Ratio of de Broglie wavelength to equilibrium interatomic distance

	Velocity (km/s)					
Specie	0.1	1	3	5	10	20
N_2	1.2983	0.1298	0.0433	0.0260	0.0130	0.0065
NO	1.1558	0.1156	0.0385	0.0231	0.0116	0.0058

A highly parallelized QCT code developed by Kulakhmetov for O_2 + O system [28] is used in this work. The code is extended to be able to calculate multi-species atom-molecule collision. For collisional pair atom A and molecule BC, the mass of each atom is denoted as m_A, m_B and m_C. We place the free atom A and molecule BC as it is shown in Fig.2.8. Since the center of mass (COM) for the whole system doesn't move during collision, the COM is placed at the origin. Plane ε is the collisional plane, which contains free atom A and COM of BC. Without loosing generality, the plane is set as $y-z$ plane and the initial collisional velocity is set parallel to axis z. b is the impact parameter of the collision. θ and ϕ are azimuth and polar angle of molecule BC.

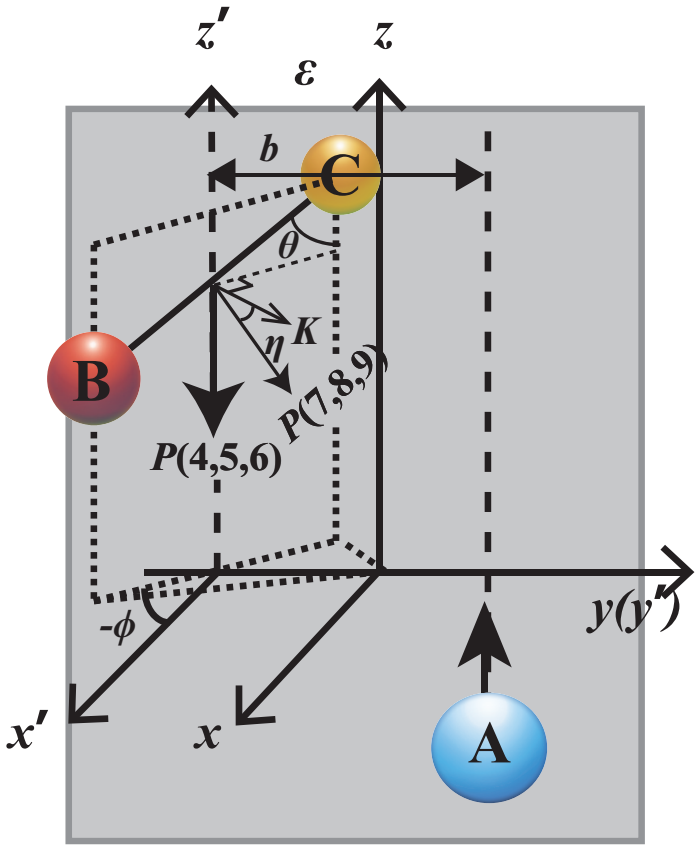

Figure 2.8. Collisional pair position in QCT calculation

In the above definition, the Cartesian system is a space-fixed system. The coordinates of particles A, B and C in such system can be denoted as (q_1, q_2, q_3), (q_4, q_5, q_6) and (q_7, q_8, q_9). The momentum can be denoted as (p_1, p_2, p_3), (p_4, p_5, p_6) and (p_7, p_8, p_9). Then the Hamilton's equations of the system are :

$$\begin{aligned} \frac{dx_i}{dt} &= \frac{\partial H}{\partial p_i}(i = 1, 2, ..., 9), \\ \frac{dp_i}{dt} &= -\frac{\partial H}{\partial q_i} = -\frac{\partial V}{\partial q_i}(i = 1, 2, ..., 9). \end{aligned} \tag{2.10}$$

There are 18 ordinary differential equations (ODE) to be solved. However, it is clear that 6 of the ODEs are redundant since they are constrained by the conservation of total momentum. By introducing generalized coordinates $Q_X = (Q_{iX}, i = 1, ..., 9)$, the ODE system can be reduced to 12 equations. Symbol X is used to denote the free atom. Taking $X = A$ as an example, then the new coordinates are used to describe

collision $A+BC$. Then (Q_{1A}, Q_{2A}, Q_{3A}) is the vector from atom B to C describing the molecular bond. (Q_{4A}, Q_{5A}, Q_{6A}) is the vector from COM of BC to A that describes the relative motion of free atom A and BC in COM frame. (Q_{7A}, Q_{8A}, Q_{9A}) describes the position of COM of the whole system, which is stationary at the origin. According to the above definition, the generalized coordinates can be transformed from original space-fixed Cartesian coordinates by:

$$Q_X = T_X q, \tag{2.11}$$

where T_X is the transformation matrix. For example, T_A can be calculated as:

$$T_A = \begin{bmatrix} 0 & 0 & 0 & -1 & 0 & 0 & 1 & 0 & 0 \\ 0 & 0 & 0 & 0 & -1 & 0 & 0 & 1 & 0 \\ 0 & 0 & 0 & 0 & 0 & -1 & 0 & 0 & 1 \\ 1 & 0 & 0 & -\frac{m_B}{m_B+m_C} & 0 & 0 & -\frac{m_C}{m_B+m_C} & 0 & 0 \\ 0 & 1 & 0 & 0 & -\frac{m_B}{m_B+m_C} & 0 & 0 & -\frac{m_C}{m_B+m_C} & 0 \\ 0 & 0 & 1 & 0 & 0 & -\frac{m_B}{m_B+m_C} & 0 & 0 & -\frac{m_C}{m_B+m_C} \\ \frac{m_A}{M} & 0 & 0 & \frac{m_B}{M} & 0 & 0 & \frac{m_C}{M} & 0 & 0 \\ 0 & \frac{m_A}{M} & 0 & 0 & \frac{m_B}{M} & 0 & 0 & \frac{m_C}{M} & 0 \\ 0 & 0 & \frac{m_A}{M} & 0 & 0 & \frac{m_B}{M} & 0 & 0 & \frac{m_C}{M} \end{bmatrix}. \tag{2.12}$$

In Eq.2.12, M is the total mass of the system (i.e. $M = m_A+m_B+m_C$). Consistently, condescending generalized momenta need to be defined. The Lagrangian of system A+BC can be calculated as:

$$L_A = \frac{1}{2}\mu_{BC}\sum_{i=1}^{3}\dot{Q_{iA}}^2 + \frac{1}{2}\mu_{A,BC}\sum_{i=4}^{6}\dot{Q_{iA}}^2 + \frac{1}{2}M\sum_{i=7}^{9}\dot{Q_{iA}}^2 - V(Q_A). \tag{2.13}$$

Then the generalized momenta are calculated as:

$$P_A = \frac{\mathrm{d}L_A}{\mathrm{d}\dot{Q}_A} = S_A\dot{Q}_A = S_A T_A(s^{-1}p), \tag{2.14}$$

where $\dot{Q}_A$ is the generalized velocities and s and S_A are vectors defined as:

$$s = I_9\begin{bmatrix} m_A & m_A & m_A & m_B & m_B & m_B & m_C & m_C & m_C \end{bmatrix}^T, \tag{2.15}$$

$$S_A = I_9\begin{bmatrix} \mu_{BC} & \mu_{BC} & \mu_{BC} & \mu_{A,BC} & \mu_{A,BC} & \mu_{A,BC} & M & M & M \end{bmatrix}^T, \tag{2.16}$$

where I_9 is a 9×9 identity matrix. The coordinates transformation is shown for A+BC system. Once exchange reaction happens, the free atom might become B or C

after the collision. The generalized coordinates might become Q_B or Q_C. They can be related by the following transformation:

$$\begin{aligned} Q_B &= T_B T_A^{-1} Q_A, \\ Q_C &= T_C T_A^{-1} Q_A, \\ P_B &= S_B T_B {T_A}^{-1} {S_A}^{-1} P_A, \\ P_C &= S_C T_C {T_A}^{-1} {S_A}^{-1} P_C. \end{aligned} \tag{2.17}$$

Once the new generalized coordinates in COM frame is gotten, the Hamilton's equations can be formulated. Considering the generalized momentum (P_{7X}, P_{8X}, P_{9X}) are always zero due to the conservation of total momentum, the Hamiltonian becomes:

$$H = \frac{1}{2\mu_m} \sum_{i=1}^{3} P_{iX}^2 + \frac{1}{2\mu_a} \sum_{i=4}^{6} P_{iX}^2 + V(Q_{1X}, Q_{2X}, Q_{3X}, Q_{4X}, Q_{5X}, Q_{6X}), \tag{2.18}$$

where μ_m is the reduce mass of the molecule (i.e. molecule AB, BC or CA) and μ_a is the reduced mass of the whole system as $\mu_a = \mu_m m_X/(\mu_m + m_X)$. The Hamilton's equations are:

$$\frac{\mathrm{d}Q_{iX}}{\mathrm{d}t} = \frac{\partial H}{\partial P_{iX}}, \tag{2.19}$$

$$\frac{\mathrm{d}P_{iX}}{\mathrm{d}t} = -\frac{\partial V}{\partial Q_{iX}}, \tag{2.20}$$

$$(i = 1,2,3,4,5,6)$$

There are 12 ODEs to solve in Eq.2.19 and Eq.2.20. The details about numerical methods to solve these ODEs are discussed in subsection 2.2.3. We'll first introduce the process of converting quantum states and collisional orientations to classical coordinates, i.e. Pre-collision.

2.2.1 Pre-collision

In quantum mechanics, the molecular state is uniquely determined by its vibrational, rotational and electronic state. Since electronically nonadiabatic transition is not considered in this work, the electronic state can be ignored. Considering a

molecule with rotational level J, its orbital angular momentum and rotational energy are

$$L^2 = J(J+1)\hbar^2, \tag{2.21}$$

$$E_r(J) = \frac{L^2}{2I}, \tag{2.22}$$

where I is the momentum of inertia calculated as:

$$I = \mu_m R^2. \tag{2.23}$$

The momentum of inertia is determined by the reduced mass μ_m and interatomic separation of the molcule R. For an isolated molecule, energy conservation requires:

$$E_{rv}(v, J) = E_t + E_{rot}(J) + V(R), \tag{2.24}$$

where $E_{rv}(v, J)$ is the rovibrational energy determined by vibrational and rotational quantum number v and J, E_t is the translational energy and $V(R_m)$ is the potential energy between atoms. Once the molecule reaches maximum vibrational stretch R_m, E_t reduces to zero and Eq.2.24 becomes:

$$\frac{J(J+1)\hbar^2}{2\mu_m R_m^2} + V(R_m) = E_{rv}(v, J). \tag{2.25}$$

Eq.2.25 can be solved numerically by secant method to get the maximum separation R_m. R_m can be related to the generalized coordinates as:

$$R_m = \max\sqrt{Q_{1X}^2 + Q_{2X}^2 + Q_{3X}^2} \tag{2.26}$$

We can integrate the Hamilton's equation of isolated molecule as the following

$$\frac{\mathrm{d}Q_{iX}}{\mathrm{d}t} = \frac{\partial H}{\partial P_{iX}}, \tag{2.19 reduced}$$

$$\frac{\mathrm{d}P_{iX}}{\mathrm{d}t} = -\frac{\partial V}{\partial Q_{iX}}, \tag{2.20 reduced}$$

$$(i = 1, 2, 3)$$

from maximum stretch with zero velocity to another appearance of maximum stretch to get a function $R = R(t)$ and vibration period τ_v as it is shown in Fig.2.9. Assume

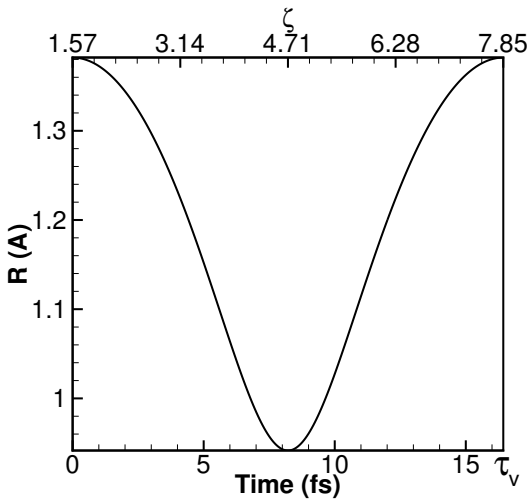

Figure 2.9. Molecular stretch during a vibrational period of N_2 with $(v, J) = (10, 0)$

the initial molecular phase angle is ζ , then the initial bond length, $R_0 = R(t/\tau_v = \zeta/2\pi - 0.25)$.

Once R_0 is found, the initial molecular coordinates collisions with atom A as free atom are defined as:

$$\begin{aligned} Q^0_{1A} &= R_0 \sin(\theta)\cos(\phi), \\ Q^0_{2A} &= R_0 \sin(\theta)\sin(\phi), \\ Q^0_{3A} &= R_0 \cos(\theta), \end{aligned} \tag{2.27}$$

where θ and ϕ are molecular orientation angles, that were already introduced at the beginning of Sec.2.2. As it is shown in Fig.2.8, the free atom, A, and the COM of molecule BC are placed in the Y-Z collision plane and the COM of the system is at origin, the initial Q^0_{4A} through Q^0_{6A} coordinates can be expressed as:

$$\begin{aligned} Q^0_{4A} &= 0, \\ Q^0_{5A} &= b, \\ Q^0_{6A} &= -\sqrt{\rho^2 - b^2}. \end{aligned} \tag{2.28}$$

where b is the impact parameter and ρ is the size of collision shell, which is chosen such that the attractive force outside this shell are insignificant. The convergence

study of collision shell can be found in Ref. [28]. A collision shell $\rho = 15$A is kept using here.

To find the initial generalized momentum, it can be noticed that at the maximum molecular stretch, there should be no momentum in the direction of molecular bond,

$$P_{1,2,3,A} \cdot Q_{1,2,3,A} = 0, \tag{2.29}$$

while the momentum can be related to angular momentum as:

$$|P_{1,2,3,A}|^2 = \frac{J(J+1)\hbar^2}{R_m^2}. \tag{2.30}$$

To define the direction of momentum vector, a reference vector defined as the cross product of molecular bond $\overrightarrow{BC}$ and axis z is introduced, $K = Q_{1,2,3,A} \times e_z$. Then the direction of rotational momentum can be uniquely determined by an angle η, which is the angle between vector K and the momentum since the vector of momentum is always in the plane normal to vector $Q_{1,2,3,A}$:

$$\eta = \arccos(\frac{P_{1,2,3,A} \cdot K}{|P_{1,2,3,A}||K|}). \tag{2.31}$$

The momentum at maximum stretch R_m are:

$$\begin{aligned} P_{1A}^m &= -\frac{\sqrt{J(J+1)}\hbar}{R_m}(\sin(\phi)\cos(\eta) + \cos(\phi)\cos(\theta)\sin(\eta)) \\ P_{2A}^m &= \frac{\sqrt{J(J+1)}\hbar}{R_m}(\cos(\phi)\cos(\eta) - \sin(\phi)\cos(\theta)\sin(\eta)) \\ P_{3A}^m &= \frac{\sqrt{J(J+1)}\hbar}{R_m}\sin(\theta)\sin(\eta). \end{aligned} \tag{2.32}$$

Then the angular momentum is calculated as:

$$\begin{aligned} L_x &= Q_{2A}^m P_{3A}^m - Q_{3A}^m P_{2A}^m \\ L_y &= Q_{3A}^m P_{1A}^m - Q_{1A}^m P_{3A}^m \\ L_z &= Q_{1A}^m P_{3A}^m - Q_{3A}^m P_{1A}^m \end{aligned} \tag{2.33}$$

For isolated molecule, the angular momentum is conserved as there is no torque. Thus the initial molecular momentum with phase angle ζ can be obtained by solving the following equations.

$$\begin{aligned} Q^0_{2A}P^0_{3A} - Q^0_{3A}P^0_{2A} &= L_x, \\ Q^0_{1A}P^0_{3A} - Q^0_{3A}P^0_{1A} &= -L_y, \\ Q^0_{1A}P^0_{2A} - Q^0_{2A}P^0_{1A} &= L_z, \end{aligned} \tag{2.34}$$

The atomic momentum relative to the molecule can be formulated as:

$$\begin{aligned} P^0_{4A} &= 0 \\ P^0_{5A} &= 0 \\ P^0_{6A} &= \mu_{a,bc}V_r, \end{aligned} \tag{2.35}$$

since the relative velocity is along direction e_z.

2.2.2 Sample Collisional Geometries

In Sec.2.2.1, the method about how to convert quantum states of collisional particles to classical coordinates and momentum was discussed. It should be noted that azimuth angle θ, polar angle ϕ, phase angle ζ, reference angle η, and impact parameter b are introduced to describe the initial collisional geometries. These initial conditions uniquely determine the initial positions of the colliding particles. However, we only care about state-specific transition cross sections $\sigma_r(V_r, v, J \to v', J')$ and state-specific transition rate $k_r(T_t, v, J \to v', J')$ in DSMC and CFD calculations. Thus, we need to integrate the differential cross sections $\sigma \mathrm{d}\Omega$ with respect to initial geometries to get the state-specific cross sections. Due to the high dimension of the initial collisional geometries, *Monte Carlo* integration is preferred to be used.

The first step of *Monte Carlo* integration is the sampling of points in integration domain Ω. According to geometric relations, the distribution functions of the angles and impact parameters are as the following:

$$\begin{aligned} f(b) &= \frac{2}{b_{max}^2} b, \qquad b \in [0, b_{max}] \\ f(\theta) &= 1/2 \sin(\theta), \quad \theta \in [0, \pi] \\ f(\phi) &= 1/2\pi, \qquad \phi \in [0, 2\pi] \\ f(\eta) &= 1/2\pi, \qquad \eta \in [0, 2\pi] \\ f(\zeta) &= 1/2\pi, \qquad \zeta \in [0, 2\pi] \end{aligned} \tag{2.36}$$

where b_{max} is a cut of impact parameter. It needs to be chosen so that there is no strong scattering once b becomes larger than b_{max}. We can choose b_{max} by a convergence study of cross sections or the study of scattering events. A study of b_{max} based on convergence of cross sections are shown in Fig.2.10. Case 1 has an initial condition $V_r = 15$ km/s with $(v, J) = (0, 100)$ and case 2 has $V_r = 5$ km/s with $(v, J) = (30, 50)$. It could be found that the cross sections at higher collisional energy converge more easily than low energy cases. $b_{max} = 3A$ is enough for exchange cross sections but higher value is needed for inelastic collision cross sections. A detailed discussion of the relation between impact parameter and scattering behavior will be discussed later. To resolve the scattering angle,$b_{max} = 6.5A$ is chosen in this work. For efficiency, it may be possible to change b_{max} with relative translational energy. If Boltzmann distribution is assumed, which is in the case of rate calculation, the relative velocity V_r follows the distribution function:

$$f(V_r) = \sqrt{\frac{8m_r}{\pi kT}} \left(\frac{m_r V_r^2}{2kT} \right) \exp\left(-\frac{m_r V_r^2}{2kT} \right), \quad V_r \in [0, +\infty] \tag{2.37}$$

where T is the translational temperature and m_r is the reduced mass of the system, $m_r = \mu_{X,m}$. Once the distribution functions are obtained, the initial collisional geometries can be sampled as:

$$\begin{aligned} b &= \sqrt{R_f} b_{max}, \\ \theta &= \arccos(1 - 2R_f), \\ \phi &= 2\pi R_f, \\ \eta &= 2\pi R_f, \\ \zeta &= 2\pi R_f, \end{aligned} \tag{2.38}$$

where R_f is a uniformly distributed random number generated for each appearance in Eq.2.38.

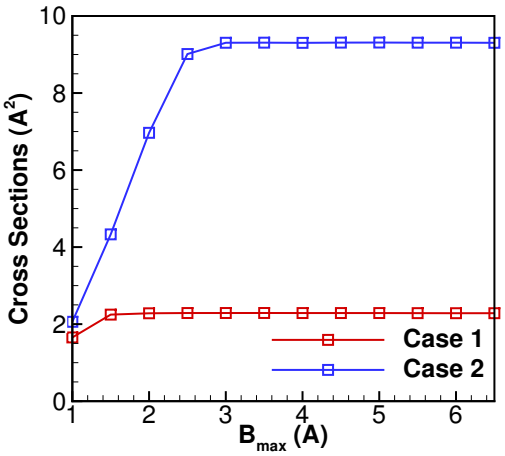

(a) Exchange cross sections

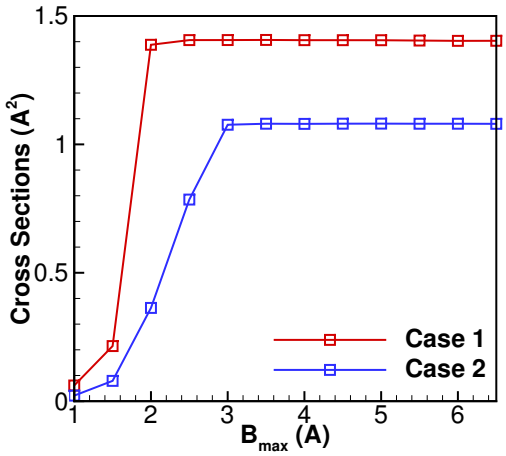

(b) Monaquantum transition cross sections $\sigma(V_r, v, J \rightarrow v + 1)$

Figure 2.10. Convergence study of cross sections with differen maximum impact parameter

The second step of *Monte Carlo* integration is the calculation of integrated function. Recall that the cross section is an area in which molecules with certain collisional

processes (excitation/relaxation or chemical reaction) happening pass, we can relate the cross sections $\sigma_r(V_r, v, J)$ to an opacity function $P_r(Vr, v, J)$:

$$\sigma_r(Vr, v, J) = \pi b_{max}^2 P_r(V_r, v, J) \tag{2.39}$$

and the opacity function can be obtained by integration:

$$P_r(V_r, v, J) = \int_{\zeta=0}^{2\pi}\int_{\eta=0}^{2\pi}\int_{\phi=0}^{2\pi}\int_{\theta=0}^{\pi}\int_{b=0}^{b_{max}} P_r(V_r, v, J, b, \theta, \phi, \eta, \zeta) \\ f(b)\mathrm{d}b f(\theta)\mathrm{d}\theta f(\phi)\mathrm{d}\phi f(\eta) f(\eta)\mathrm{d}\eta f(\zeta)\mathrm{d}\zeta. \tag{2.40}$$

where $P_r(V_r, v, J, b, \theta, \phi, \eta, \zeta)$ is a δ function defined as:

$$P_r(V_r, v, J, b, \theta, \phi, \eta, \zeta) = \begin{cases} 1, & \text{if event r happens} \\ 0, & \text{otherwise} \end{cases} . \tag{2.41}$$

We call this function as reactivity function in this work. Thus Eq.2.41 is the function needs to be evaluated in *Monte Carlo* integration. Similarly,the state-specific rates can be calculated by averaging the product of cross sections $\sigma_r(Vr, v, J)$ with relative velocities V_r as:

$$\begin{aligned} k_r^{v,J}(T) =& \overline{\sigma_r(V_r, v, J)V_r} = \int_0^\infty \sigma_r(V_r, v, J)V_r f(V_r) dV_r \\ =& \sqrt{\frac{8kT}{\pi m_r}} \int_0^\infty \sigma_r(\sqrt{\frac{2E_t}{m_r}}, v, J) \left(\frac{E_t}{kT}\right) \exp\left(-\frac{E_t}{kT}\right) \mathrm{d}\left(\frac{E_t}{kT}\right) \\ =& \sqrt{\frac{8\pi kT}{m_r}} b_{max}^2 \int_0^\infty P_r(\sqrt{\frac{2E_t}{m_r}}, v, J) f\left(\frac{E_t}{kT}\right) \mathrm{d}\left(\frac{E_t}{kT}\right) \end{aligned} \tag{2.42}$$

In Eq.2.42, E_t is the translational energy of the collision calculated as $E_t = 1/2 m_r V_r^2$. From Eq.2.42, it can be found that the reactivity function, Eq.2.41, is also the integrated function for state-specific rate calculation. However, the relative velocity should be sampled from function $f(E_t/kT)$ in Eq.2.42 instead of Eq.2.37. $f(E_t/kT)$ is defined as:

$$f(\frac{E_t}{kT}) = \frac{E_t}{kT} \exp\left(\frac{E_t}{kT}\right). \tag{2.43}$$

This is a $\Gamma(2, 1)$ distribution. E_t and V_r can be sampled from:

$$V_r = \sqrt{\frac{2E_t}{m_r}} = \sqrt{\frac{2kT}{m_r} \ln(R_f \cdot R_f)}, \tag{2.44}$$

where R_f is a uniformly distributed random number. Combing Eq.2.38, 2.44, 2.39 and 2.42 together, we can calculate the *Monte Carlo* integration as:

$$\sigma_r(V_r, v, J) = \pi b_{max}^2 \sum_{i=1}^{N} \frac{P_r^{(i)}(V_r, v, J, b, \theta, \phi, \eta, \zeta)}{N} = \pi b_{max}^2 \frac{N_r(V_r, v, J)}{N}, \tag{2.45}$$

$$k_r(T, v, J) = \sqrt{\frac{8\pi kT}{m_r}} b_{max}^2 \sum_{i=1}^{N} \frac{P_r^{(i)}(V_r, v, J, b, \theta, \phi, \eta, \zeta)}{N} = \sqrt{\frac{8\pi kT}{m_r}} b_{max}^2 \frac{N_r(T, v, J)}{N}, \tag{2.46}$$

where N is the total number of sampling and N_r is the counting number of times that process r occurs. To avoid ambiguity, the rates gotten by direct Monte Carlo integration will be called as direct-QCT in the following content in order to be distinguished from rates gotten by numerical integration of QCT cross sections.

Monte Carlo integration converges as $1/\sqrt{N}$. If the sampling error is defined as 1 standard deviation and the expectations of cross sections and state specific rates are estimated as:

$$\overline{\sigma_r(V_r, v, J)} = \pi b_{max}^2 \frac{N_r(V_r, v, J)}{N}, \quad \overline{k_r(T, v, J)} = \sqrt{\frac{8\pi kT}{m_r}} b_{max}^2 \frac{N_r(T, v, J)}{N} \tag{2.47}$$

then the cross section sampling error can be estimated as:

$$\Delta\sigma_r(V_r, v, J) = \pi b_{max}^2 \frac{N_r}{N} \sqrt{\frac{N - N_r}{N N_r}}, \tag{2.48}$$

and reaction rate sampling error can be estimated as:

$$\Delta k_r^{v,J}(T) = \sqrt{\frac{8\pi kT}{m_r}} b_{max}^2 \frac{N_r}{N} \sqrt{\frac{N - N_r}{N N_r}}. \tag{2.49}$$

These estimations can provide the uncertainty of the calculations if the number of samples is large enough. The required sample size is determined from convergence study. This study is conducted for $(V_r, v, J) = (5km/s, 30, 50)$ and $(V_r, v, J) = (15km/s, 0, 100)$. Fig.2.11 shows the vibrational state-specific cross sections, $\sigma(V_r, v, J \to v')$ and rotational state-specific cross sections Fig.2.12 shows the rovibrational state-specific cross sections, $\sigma(V_r, v, J \to v', J')$. It can be found that $\sigma(V_r, v, J \to v')$ is easier to converge than $\sigma(V_r, v, J \to J')$ due to the less energy bins. $\sigma(V_r, v, J \to v', J')$

is very hard to converge even with a million samples. However, a million trajectories can well resolve cross sections larger than 1E-3$\mathring{A}^2$. In table2.3, the reaction probability, average error of $\sigma(V_r, v, J \rightarrow v')$, $Error_v$ and $\sigma(V_r, v, J \rightarrow J')$, $Error_J$ are presented. The latter two ones are calculated as:

$$\begin{aligned} Error_v &= \frac{1}{v_{max}} \sum_{v'=1}^{v_{max}} \left(\frac{|\sigma(V_r, v, J \rightarrow v') - \sigma(V_r, v, J \rightarrow v')^*|}{\sigma(V_r, v, J \rightarrow v')^*} \right) \\ Error_J &= \frac{1}{J_{max}} \sum_{J'=1}^{J_{max}} \left(\frac{|\sigma(V_r, v, J \rightarrow J') - \sigma(V_r, v, J \rightarrow J')^*|}{\sigma(V_r, v, J \rightarrow J')^*} \right) \end{aligned} \tag{2.50}$$

where the terms with star superscript are results from calculations with a million samples. Total exchange reaction probability converges with around 1E5 trajectories. However, to keep the error of state-specific cross sections less than 10%, at least a million trajectories are needed.

In addition, the convergence of rate calculation is also studied here. Since the integration for rate is one dimension higher than for cross sections, it is expected that less samples are needed. A rate calculation for T=10,000K and $v = 0$ is conducted. 1E4 samples are calculated for each rotational state, which in summary generate more than 2 million samples. The equilibrium state-specific exchange reaction rates $k_{EX}(T, v = 0, J)$ and rotational nonequilibrium reaction rates $k_{EX}(T, T_R, v = 0)$ are presented in Fig.2.13. It can be found that at least 1E4 samples are needed to resolve state-specific reaction rates but the number can be reduced to a thousand if the nonequilibrium rates is interested. In general, the higher level state-specific rates are averaged, the less samples are needed for rates calculation. This conclusion is especially important for equilibrium rates calculation since there are in total 9751 rovibrational states for N_2 molecule and it is impossible to calculate $1E4 \times 9751 \approx 1E8$ samples. We will use 500 samples for rates calculation if there is no special explanations.

Table 2.3. Convergence study for number of sampling

				Number of samples		
	v	J	$V_r(km/s)$	1E4	1E5	1E6
Exchange Reaction	0	100	15	0.0201	0.0171	0.0172
Probability	5	30	50	0.0716	0.0707	0.0701
$Error_v$	0	100	15	53.19%	17.9%	0
	5	30	50	20.56%	6.89%	0
$Error_J$	0	100	15	64.72%	24.59%	0
	5	30	50	62.92%	25.47%	0

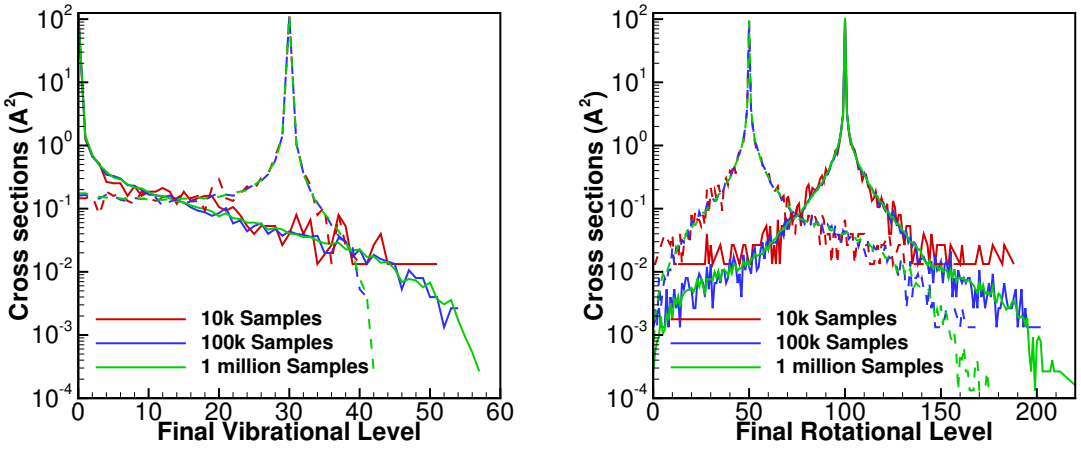

Figure 2.11. Sampling convergence of inelastic transition. Solid lines: case with $V_r = 5km/s$. Dashed lines:case with $V_r = 15km/s$

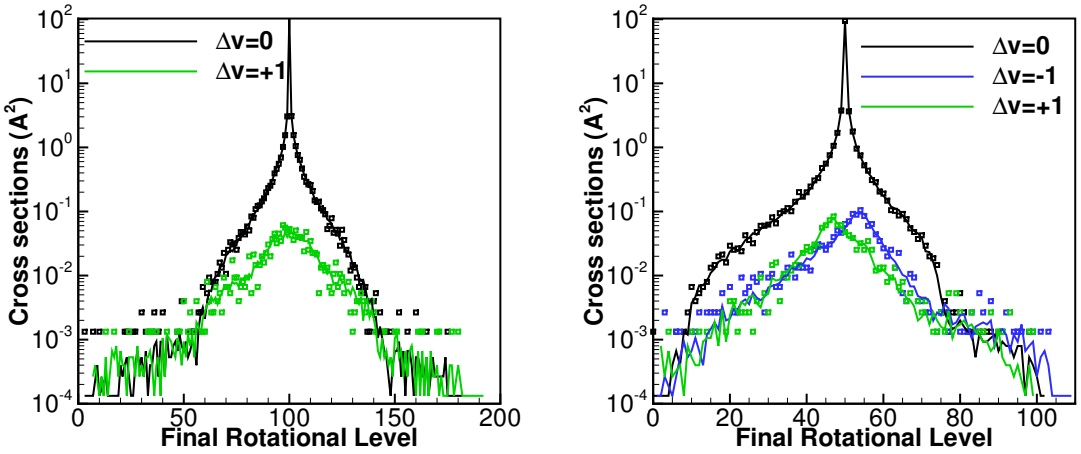

(a) V_r=15km/s, $(v, J) = (0, 100)$ (b) V_r=5km/s, $(v, J) = (30, 50)$)

Figure 2.12. Post-collision rotational distribution for monoquantum transition. Solid lines: 1 million samples. Symbols: 0.1 million samples

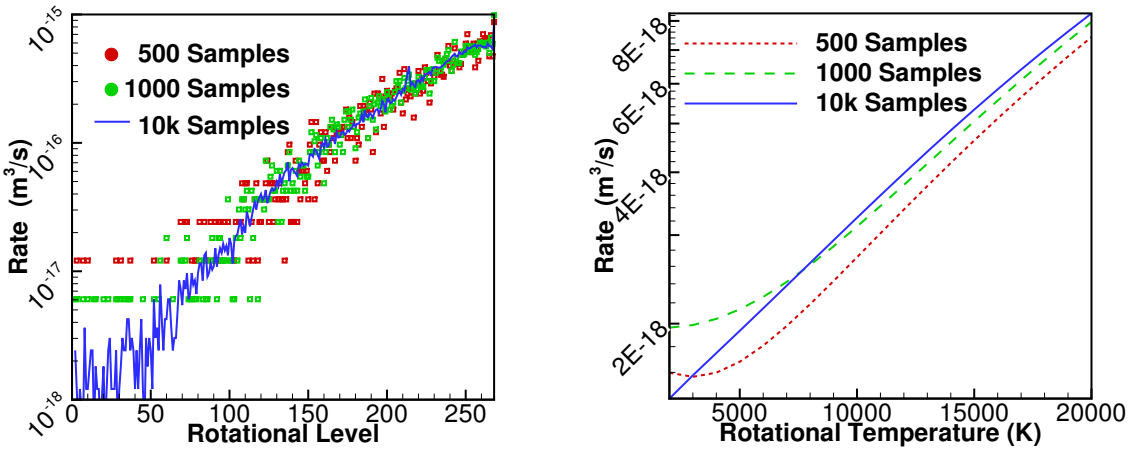

(a) $k_{EX}(T, v = 0, J)$ (b) $k_{EX}(T, T_R, v = 0)$

Figure 2.13. Equilibrium rotational state-specific exchange reaction rates and rotational nonequilibrium reaction rates for T=10,000K and $v = 0$

2.2.3 Trajectory integration

Once the initial conditions of collision are gotten, the Hamilton system Eq.2.19 and 2.20 need to be solved. Typically, velocity Verlet or leap-frog methods are used in Molecular Dynamics(MD) [46]. The scheme of velocity Verlet method is the following:

$$\begin{aligned} Q_X(t+\Delta t) &= Q_X(t) + {S_X}^{-1}\left(P_X(t)\Delta t - \left.\frac{\partial V}{\partial Q_X}\right|_t \frac{\Delta t^2}{2}\right) + O(\Delta t)^4, \\ P_X(t+\Delta t) &= P_X(t) - \frac{1}{2}\left(\left.\frac{\partial V}{\partial Q_X}\right|_t + \left.\frac{\partial V}{\partial Q_X}\right|_{t+\Delta t}\right)\Delta t + O(\Delta t^2), \end{aligned} \tag{2.51}$$

where Δt is the time step. It should be noticed that although the numerical error of the generalized coordinates and momenta scale up as Δt^4 and Δt^2, the global cumulative error scales up as Δt^2. [46] There are mainly three reasons why such scheme is preferred in MD. First the motions are invariant under time reversal, which could help to recheck the calculation. Second, the simplicity of the scheme helps accelerate simulations of hundreds of molecules in MD. Third, the integrator is symplectic, i.e. the symplectic two-form $\mathrm{d}p \wedge \mathrm{d}q$ is conserved. It could avoid long time energy drifting, which is essential for MD calculation since the first step of MD simulation is usually the thermostat and barostat of the system, which takes 1E3 to 2E3 time steps. However, these advantages don't benefit QCT since QCT uses more complex PES than MD and there usually exist several saddle points. QCT only calculates one interactive collisional pair. Short term energy drifting is more dangerous than long term energy drifting in QCT since it determines the details of collisional process. In this work, we continue using 5-6 order Runge-Kutta (RKV56) method as before. [28, 47]. For ODE $\dfrac{\mathrm{d}Y}{\mathrm{d}t} = f$, the fifth and sixth order Runge-Kutta solution can be represented as:

$$Y5_{i+1} = Y_i + 13/160k_1 + 2375/5984k_3 + 5/16k_4 + 12/85k_5 + 3/44k_6, \tag{2.52}$$

and

$$\begin{aligned} Y6_{i+1} = Y_i + 3/40k_1 + 875/2244k_3 + 23/72k_4 + 264/1955k_5 \\ + 125/11592k_7 + 43/616k_8, \end{aligned} \tag{2.53}$$

where

$$
\begin{aligned}
k_1 &= \Delta t f(Y_i) \\
k_2 &= \Delta t f(Y_i + 1/6 k_1) \\
k_3 &= \Delta t f(Y_i + 4/75 k_1 + 16/75 k_2) \\
k_4 &= \Delta t f(Y_i + 5/6 k_1 - 8/3 k_2 + 5/2 k_3) \\
k_5 &= \Delta t f(Y_i - 165/64 k_1 + 55/6 k_2 - 425/64 k_3 + 85/96 k_4) \\
k_6 &= \Delta t f(Y_i + 12/5 k_1 - 8 k_2 + 4015/612 k_3 - 11/36 k_4 + 88/255 k_5) \\
k_7 &= \Delta t f(Y_i - 8263/15000 k_1 + 124/75 k_2 - 643/680 k_3 - 81/250 k_4 + 2484/10625 k_5) \\
k_8 &= \Delta t f(Y_i + 3501/1720 k_1 - 300/42 k_2 + 297275/52632 k_3 - 319/2322 k_4 \\
&+ 24068/84065 k_5 + 3850/26703 k_7).
\end{aligned}
\tag{2.54}
$$

The cumulative error between 5-order and 6-order can be calculated as:

$$
\epsilon(\Delta t) = \frac{Y6_{i+1} - Y5_{i+1}}{\Delta t} = C \Delta t^5. \tag{2.55}
$$

If the time step is reduced to $q\Delta t$, the error decreases to:

$$
\epsilon(q\Delta t) = C(q\Delta t)^5 = q^5 \epsilon(\Delta t). \tag{2.56}
$$

Thus, we can change the time step to $q\Delta t$ if the current error ϵ is larger than integration tolerance TOL. q is calculated as:

$$
q = \left(\frac{TOL}{\eta \epsilon} \right)^{\frac{1}{5}}. \tag{2.57}
$$

The factor η is adjusted to compensate truncation error. It is chosen to be 2 in this work.

Since there are 6 ODEs for generalized coordinates and 6 ODEs for generalized momenta, the cumulative error is calculated as the $||x||_2$ norm of generalized coordinates and generalized momenta

$$
\begin{aligned}
\epsilon_1 &= \sqrt{\epsilon(1:6) \cdot \epsilon(1:6)}, \\
\epsilon_2 &= \sqrt{\epsilon(7:12) \cdot \epsilon(7:12)}.
\end{aligned}
\tag{2.58}
$$

However, considering the order of ϵ_1 and ϵ_2 are different, the relative error is used,

$$\epsilon_1' = \frac{\epsilon_1}{||Q||}, \quad \epsilon_2' = \frac{\epsilon_2}{||P||}, \tag{2.59}$$

and

$$\epsilon = \max(\epsilon_1', \epsilon_2') \tag{2.60}$$

It should be noticed that the definition of TOL is the tolerance of relative error now. Besides, the energy drifting is also tracked as the ratio of energy loose:

$$\Delta E/E_0 = (E - E_0)/E_0. \tag{2.61}$$

The energy drifting is checked every 500 time steps. Once it becomes larger than tolerance *TOL2*, the integration of Eq.2.19,2.20 is restarted with a smaller TOL.

A comparison of trajectory integration by Verlet and RKV56 method is shown in Fig.2.14. The time step of Verlet method is equal to the initial time step of RKV56 method. The solid lines represent the percentage of energy loose and the symbols are added on the lines every ten time steps. The dashed line at the bottom shows the $N-N$ bond distance. It can be found that although RKV56 method has larger time step during integration and the energy keeps decreasing, the energy drifting is much smaller than Verlet method due to its higher order. In addition, it is expected that RKV56 method is more accurate at the vibrational inner turning point since it has smaller time step.

A detail investigation for the influence of TOL to trajectory integration is presented in Table 2.4 and Fig.2.15. The initial conditions with collisional velocity $V_r = 5$, $15km/s$, vibrational level $v = 0$, 1 and rotational level $J = 0$, 50 are used. The rovibrational levels are selected since they are the most probable states for T=10,000K. The convergence of state specific inelastic cross sections $\sigma(V_r, v, J \to v')$ and $\sigma(V_r, v, J \to J')$ is studied, where v' and J' are post collision vibrational and rotational states. 100,000 initial collisional orientations are sampled for the calculation and the same conditions are used for different TOL to ensure that the only difference is the control of trajectory integration. The accurate cross sections are calculated

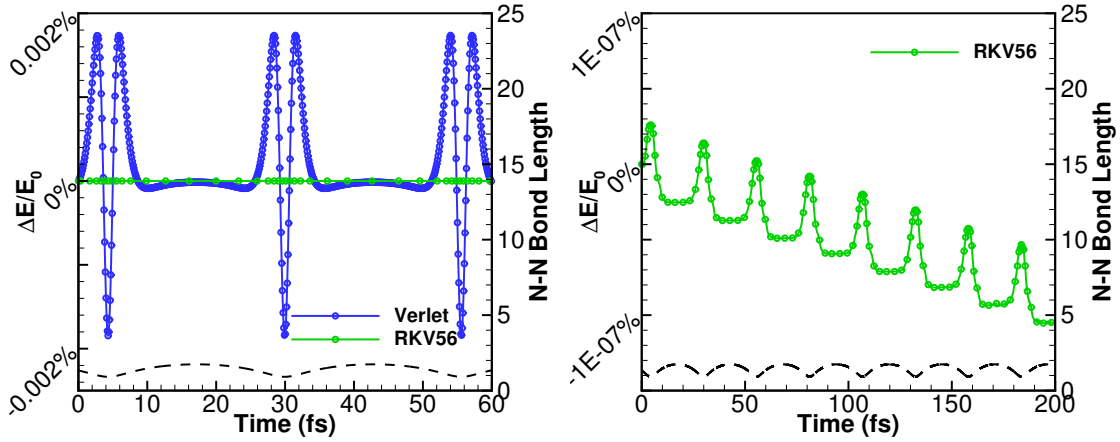

Figure 2.14. Comparison of energy loss for velocity Verlet and RKV56 method

with TOL=1E-12 and a million trajectories. In Table 2.4, the error of vibrational cross sections $Error_v$, rotational cross sections $Error_J$, percentage of trajectories with error $Error_{trj}$ and speedup S are compared. The definitions are the followings:

$$Error_v = \sum_{v'} \left[\log(\sigma_{TOL2}(V_r, v, J \to v')/\sigma_{Accurate}(V_r, v, J \to v'))\right]^2, \tag{2.62}$$

$$Error_J = \sum_{J'} \left[\log(\sigma_{TOL2}(V_r, v, J \to J')/\sigma_{Accurate}(V_r, v, J \to J'))\right]^2, \tag{2.63}$$

$$Error_{trj} = 1 - N(\Delta E/E_0 < TOL2 = 1E-6\%)/N \tag{2.64}$$

$$S = Time(TOL2)/Time(TOL2 = 1E-6\%), \tag{2.65}$$

where N is the number of sampled trajectories and $N(\Delta E/E_0 < TOL2)$ is the number of trajectories satisfying energy conservation conditions. From the table, we can find both inelastic state-specific vibrational and rotational cross sections get converged with TOL<1E-10, which is also presented in Fig.2.15 for initial condition $V_r = 15km/s$, $v = 0$ and $J = 50$. Collisions with lower total energy is easier to get converged with larger tolerance. In addition, the speedup changes less than 5% if TOL decreases from 1E-10 to 1E-12. Thus TOL with value 1E-12 is used for further calculations to maintain energy drifting less than 1E-6%.

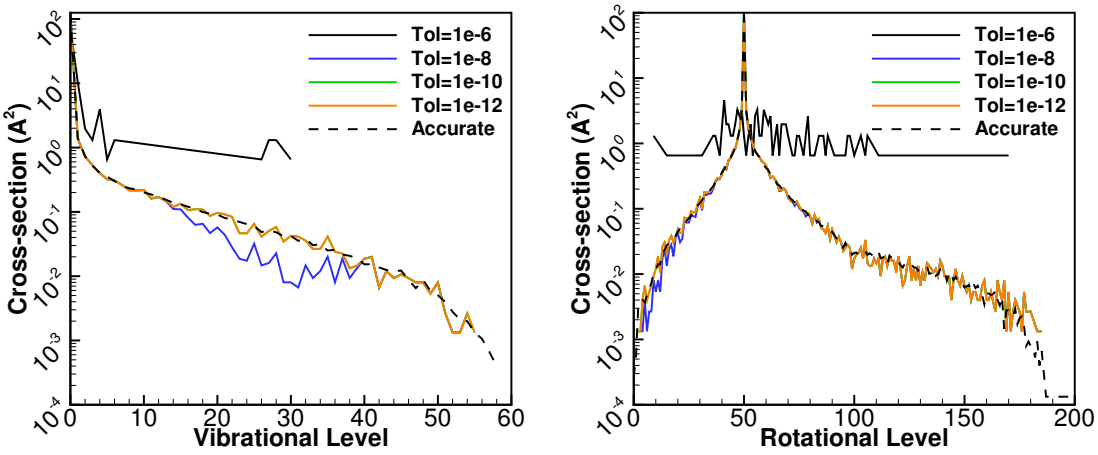

Figure 2.15. State-specific inelastic collision cross sections with different relative integration tolerance TOL. Initial condition $V_r = 15km/s$, $v = 0$ and $J = 50$

Table 2.4. Influence of TOL to state-specific inelastic cross sections

			J							
			0				50			
$V_r(km/s)$	v	TOL $\rightarrow$	1E-6	1E-8	1E-10	1E-12	1E-6	1E-8	1E-10	1E-12
5	0	$Error_v$	0	0	0	0	0	4.44E-31	4.44E-31	4.44E-31
		$Error_J$	1.03E-05	1.03E-05	1.03E-05	1.03E-05	1.60E-07	2.11E-07	2.11E-07	2.11E-07
		S	1	0.959	0.988	1.079	1	0.961	0.980	1.074
		$Error_{trj}(\%)$	0	0	0	0	0	0	0	0
5	1	$Error_v$	NaN	0	0	0	NaN	0	0	0
		$Error_J$	NaN	7.27E-06	7.27E-06	7.27E-06	NaN	3.57E-06	3.57E-06	3.57E-06
		S	1	1.442	1.454	1.617	1	1.432	1.435	1.588
		$Error_{trj}(\%)$	100	0	0	0	100	0	0	0
15	0	$Error_v$	3.88E+00	9.17E-05	1.24E-07	1.24E-07	2.83E-01	4.05E-05	4.01E-07	4.01E-07
		$Error_J$	7.05E+01	5.31E-05	3.57E-06	3.57E-06	1.65E+01	2.26E-05	7.61E-07	7.61E-07
		S	1	1.389	1.373	1.403	1	1.386	1.378	1.416
		$Error_{trj}(\%)$	100	1	0	0	100	1	0	0
15	1	$Error_v$	3.95E+00	6.39E-05	2.90E-06	2.90E-06	4.85E+00	3.05E-05	1.18E-07	1.18E-07
		$Error_J$	5.93E+01	1.05E-04	4.05E-07	4.05E-07	4.95E+01	2.85E-05	8.27E-08	8.27E-08
		S	1	1.437	1.531	1.420	1	1.516	1.722	1.559
		$Error_{trj}(\%)$	100	1	0	0	100	1	0	0

2.2.4 Post-collision

The trajectories can be integrated to infinitely long time. However, once the separation of particles reaches some limit, there is no strong interaction happening and the molecule becomes stable. Thus, an end of collision test is needed to be performed after a fixed number of integration time steps. In this test, the A+BC coordinate system is transformed to B+AC and C+AB coordinate systems by Eq.2.17. There are four possible collisional mechanisms with different criteria for post collision generalized coordinates Q'_X :

1. No reaction
$$|Q'_{1,2,3,A}| < \rho \quad \text{and} \quad |Q'_{4,5,6,A}| > \rho$$
2. A+BC→ AB+C
$$|Q'_{1,2,3,B}| < \rho \quad \text{and} \quad |Q'_{4,5,6,B}| > \rho$$
3. A+BC→ AC+B
$$|Q'_{1,2,3,C}| < \rho \quad \text{and} \quad |Q'_{4,5,6,C}| > \rho$$
4. A+BC→ A+B+C
$$|Q'_{1,2,3,A}| > \rho \quad \text{and} \quad |Q'_{4,5,6,A}| > \rho$$

If one of the above criteria is satisfied, the relative velocity of the free atom is further checked to make sure it is getting away from the stable molecule. Otherwise, the trajectory integration should be continued. Once the integration is finished, the quantum states of the molecule are obtained by relating quantum mechanical and classcial angular momentum and energy together. The post rotational level J' can be obtained by:

$$[Q'_{1,X}, Q'_{2,X}, Q'_{3,X}] \times [P'_{1,X}, P'_{2,X}, P'_{3,X}] = \sqrt{J'(J'+1)}\hbar. \tag{2.66}$$

By relating total energy of molecule to its quantum rovibrational level (v', J'), we can get the vibrational level from the solution of:

$$E_{rv}(v', J') = E_t + E_{rot} + V(R) = \frac{|P_{1,2,3,X}|^2}{2\mu_m} + V(|Q_{1,2,3,X}|) \tag{2.67}$$

It should be noticed that in classical mechanics the energy is continuous. Thus the solutions of v' and J' from Eq.2.67 and 2.66 are real numbers. To get quantum discrete level, we round the solutions to the closest integer. This treatment will result in energy leak, which has been studied by Varandas [48]. However, considering the number of rotational levels N_2 and NO have, we continue using this method.

Finally, the post collision relative velocity can be gotten from generalized momentum:

$$V_r' = \frac{P'_{4,5,6,X}}{\mu_{X,m}}. \tag{2.68}$$

The scattering angle follows:

$$\chi = \arccos\left(P'_{6X}/|P'_{1,2,3,X}|\right) \tag{2.69}$$

2.3 Application to Flow Field Calculation

Once we get the state-specific reaction rates and state-specific cross-sections, the results can be applied to flow filed calculations. Computational fluid dynamics (CFD) and direct simulation monte carlo (DSMC) are two kinds of typical flowfield calculation methods. Both of them can be used for nonequilibrium flow calculation.

In CFD method, the vibrational energy distributions of species are combined into a single vibrational energy or vibrational temperature, T_v [49]. Then an energy conservation equation for vibrational energy is added to the governing equations. The equation takes vibrational energy diffusion, vibrational-electronic energy exchange and vibrational energy relaxation ($V-T$) into account. The Landau-Teller vibrational relaxation model, which assumes the rate of vibrational energy relaxation is linearly proportional to its deviation from local equilibrium, is commonly used to model $V-T$ transition. If chemical reaction is also happening, Park's two temperature model is widely used to model the reaction. However, Landau-Teller's model assumes a harmonic oscillator and that the vibrational energy always follows a Boltzmann distribution function. Park's model results in zero reactions rates if the vibrational mode is not excited, i.e. $T_v = 0K$, which is unphysical. Besides, since there is only

limited experimental data for high temperature reaction, Park's model is often gotten by extrapolation, which may make the reaction rates lower than collisional rates. QCT method gives the ability to simulate nonequilibrium energy exchange and reaction rates at *ab-initio* level. The nonequilibrium reaction rates can be calculated as the following:

$$k_r(T,T_v,T_r) = \frac{\sum_{v=0}^{v_{max}} \sum_{J=0}^{Jmax(v)} \left[k_r(T,v,J)(2J+1) g_n \exp\left(-\frac{E_v(v)}{kT_v}\right) \exp\left(-\frac{E_{rv}(v,J)-E_v(v)}{kT_r}\right)\right]}{\sum_{v=0}^{v_{max}} \sum_{J=0}^{Jmax(v)} \left[(2J+1) g_n \exp\left(-\frac{E_v(v)}{kT_v}\right) \exp\left(-\frac{E_{rv}(v,J)-E_v(v)}{kT_r}\right)\right]} \tag{2.70}$$

where: T, T_v and T_r are translational, vibrational, and rotational temperatures. At equilibrium conditions, $T = T_r = T_v$. Here, g_n is the nuclear spin degeneracy. For N_2, g_n equals to 6 for even J value and 3 for odd J value. The relaxation time can be solved from master equation, which will be discussed later.

In DSMC method, stochastic molecular collisions are simulated and the flowfield properties are gotten from averaging the molecular properties in sampling cell. Different from MD and QCT calculations, the particles are not really colliding. The method only makes sure that the collisional frequency and macroscopic energy exchange is correct. Thus, no trajectories integration is needed and several phenomenological models are introduced. Different from CFD, DSMC uses cross sections instead of rates since it needs to perform stochastic collision. The output of QCT calculation directly provides us with cross sections. However, there are some reasons that make us unable to use the rates directly. We'll discuss this in detail in Chap.4.

Besides, we should note that QCT calculation is limited to electronically adiabatic transition since the *ab-initio* based potential energy surface is usually calculated for specific electronic state. Disregarding nonadiabatic transitions will lead to an incorrect prediction of rates. For example, without the electronic correction factor, equilibrium dissociation rates calculated by the Varandas and Pais potential are up to a factor of 4 lower than experimental rates by Shatalov [50] in the 5,000 K to 10,000 K temperature range. There are some methods [51–53] discussed in Ref. [28]. In this work, we followed the method by by Truhlar, [54] which was used by Gamallo

et al. [37] for $N_2 + O$ system. The method introduces an electronic degeneracy of rates, g_{elec} and assumes the reaction only happens on $^3A''$ PES, $k(T) = g_{elec}\, k_{^3A''}(T)$. The degeneracy is calculated as:

$$g_{elec} = Q^{elec}_{N_2O(^3A'')} / (Q^{elec}_{O(^3P)} \cdot Q^{elec}_{N_2(X^1\Sigma)}) \tag{2.71}$$

where Q is the electronic partition function for $N_2(X^1\Sigma)$, $O(^3P)$ and $N_2O(1^3A'')$. The spin angular momentum quantum number of $N_2(X^1\Sigma)$ is 0 thus $Q^{elec}_{N_2O(^3A'')} = 1$. $Q^{elec}_{O(^3P)}$ equals 3. The condition of $O(^3P)$ is more complex as there are three possible states with different total angular momentum quantum number $O(^3P_0)$, $O(^3P_1)$, and $O(^3P_2)$. The corresponding energy and electronic partition function are listed in table 2.5. Thus $Q^{elec}_{O(^3P)} = 5 + 3\exp(-227.76/T) + \exp(-326.6/T)$ and:

$$g_{elec} = \frac{3}{5 + 3\exp(-227.76/T) + \exp(-326.6/T)} \tag{2.71 revisited}$$

As the temperature increases, g_{elec} decreases asymptotically to 1/3. This correction is applied to equilibrium, nonequilibrium and state-specific rates. The correction could not be explicitly applied to cross sections since it's temperature dependent. Therefore the cross sections are divided by asymptotic value 3 in the following work if there is not special explanation.

Table 2.5. Electronic levels for $O(^3P)$

State	Energy (K)	Q^{elec}
$O(^3P_0)$	326.6	1
$O(^3P_1)$	227.76	3
$O(^3P_2)$	0	5

3. QCT CALCULATION RESULTS

In this chapter, QCT calculation results of cross sections and rates with Gamallo *et al.*'s $^3A''$ and $^3A'$ PES are presented. The aim of this chapter is to verify the calculations by comparison to other numerical and experimental results, provide preliminary idea of collision dynamics and build foundation for state-specific cross sections modeling.

3.1 Equilibrium Reaction Rates

One of the most fundamental usage of QCT calculations is the equilibrium reaction rates calculation. It expands the ability to estimate rates accurately in the case that there is no experimental device available to conduct high temperature experiments, i.e. $T > 5,000$K. For $N_2 + O$ system, two reactions are available. One is the dissociation reaction :

$$N_2 + O \rightarrow 2N + O, \qquad \text{(1.1 revisited)}$$

the other is the first Zeldovich exchange reaction:

$$N_2 + O \rightarrow NO + O. \qquad \text{(1.2 revisited)}$$

As far as the author knows, there is no available experimental data for reaction 1.1 now. The only existing estimations come from Park [14,55] and Baulch [16]'s analyses based on the rates for other colliding atom or previous theoretical work. However,the nitrogen dissociation rates is approximately a factor of three higher in collisions with atomic oxygen than in collisions with diatomic oxyegn or nitrogen. [14]. There are some available experimental data for reaction 1.2. The earliest experimental work was done by Glick *et al.* [56] with a single-pulse shock tube. They obtained the rates of this reaction for temperature ranging from 2,000 to 3,000K. Later, Wray and Teare did a

more rigorous shock tube study and predicted the rates for temperature range 3000-8000K. Livesey *et al.* studied NO formation using premixed oxypropane flames at 2,880 K. [57] Monat *et al.* obtained the equilibrium rates from shock tube experiments at temperatures of 2,384 K to 3,850 K. [58] Davidson *et al.* used a kinetic model combined with previous experimental data to estimate the rates for 2,000 K to 3,000 K. [59] Park proposed an empirical rate for arbitrary temperatures. [60]. Bose and Candler ran QCT calculations using the Walch and Jaffe's PES [36] for temperature ranging from 3,000 K to 20,000 K and fit their rates to an Arrhenius form. [23] Gamallo *et al.* conducted rates calculation with their PES by VSVT method. [38]

In this work, equilibrium rates are obtained by averaging state-specific rates over rovibrational Boltzmann distribution function as described in Sec.2.3:

$$k_r(T) = \frac{\sum_{v=0}^{v_{max}} \sum_{J=0}^{Jmax(v)} k_r(T,v,J) g_n(2J+1) \exp\left(-E_{rv}(v,J)/kT\right)}{\sum_{v=0}^{v_{max}} \sum_{J=0}^{Jmax(v)} g_n(2J+1) \exp\left(-E_{rv}(v,J)/kT\right)}. \tag{3.1}$$

where k_r equals k_D for dissociation reaction and k_r equals k_{EX} for exchange reactions. The correction factor for electronically nonadiabatic introduced in Sec.2.3 should be applied. The direct-QCT calculation results were fitted to the Arrhenius form reaction rates. For dissociation reaction 1.1, the fitted expression is:

$$k_{D,\,Direct-QCT} = 2.0398 \times 10^{-13} T^{-0.4167} \exp\left(\frac{-113,980\text{K}}{T}\right) \quad m^3/s. \tag{3.2}$$

For exchange reaction 1.2, the fitted rate is:

$$k_{EX,Direct-QCT}(T) = 7.0354 \times 10^{-19} T^{0.6495} \exp\left(\frac{-37,864\text{K}}{T}\right) \quad m^3/s \tag{3.3}$$

The dissociation reaction rates are compared in Fig.3.1. Park1 and Park2 correspond to Park's estimations in Ref. [55] and [14]. It can be found that the rate still follows Arrhenius's form with relative error less than 10%. The uncertainty range of the rate is less than half an order of magnitude. Comparing to previous estimation, Park's models over predict the rates by approximate an order of magnitude. Baulch's estimation is good at temperature higher than 10,000K. In addition, the experimental measurement [61] of $N_2 + N_2 \rightarrow 2N + N_2$ is also shown in the figure. Although, there

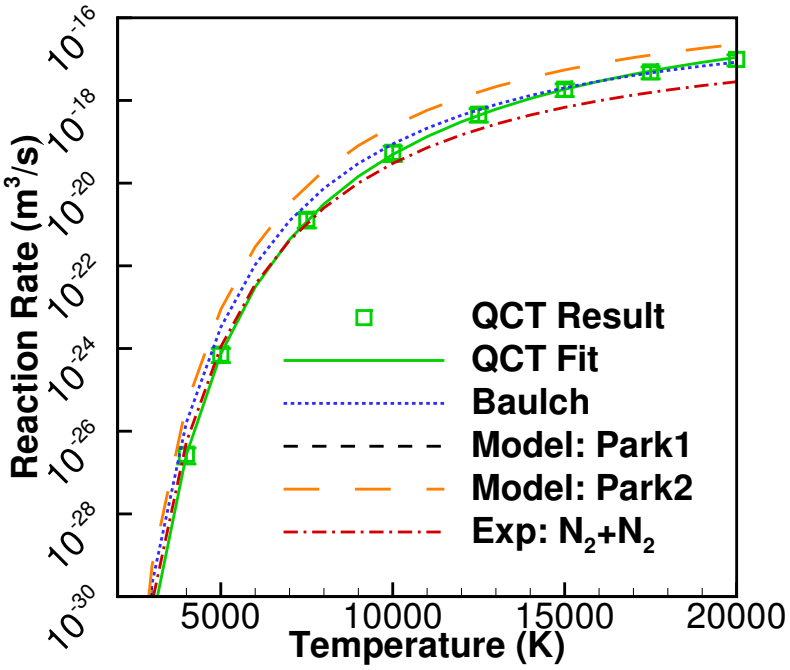

Figure 3.1. Comparison of $N_2 + O$dissociation reaction rates

is no significant difference found for $T < 7,000K$, the collision of N_2 with radical atomic oxygen is more efficient for dissociation at higher temperature with the rate increased by almost one order of magnitude.

The exchange reaction rates are compared in Fig.3.2. It should be noted that the uncertainty range of QCT results is more than an order of magnitude for temperature lower than 5,000K. This is mainly because the number of samples are not large enough to resolve such small reaction probability. Possible ways to improve include increasing number of samples and reducing maximum impact parameter at the same time or perform quantum mechanics calculation, which is more efficient for low energy collisions. [32]. Since the main interest of this work is high temperature reaction mechanisms, such methods are not applied. Nevertheless, the experimental-computed rates do fall within the uncertainty range of QCT results. In addition, although the contributions of $N_2O(^3A'')$ PES are not considered, the results are only 10% lower than the calculations done by Bose and Candler's, who considered both $^3A''$ and $^3A'$

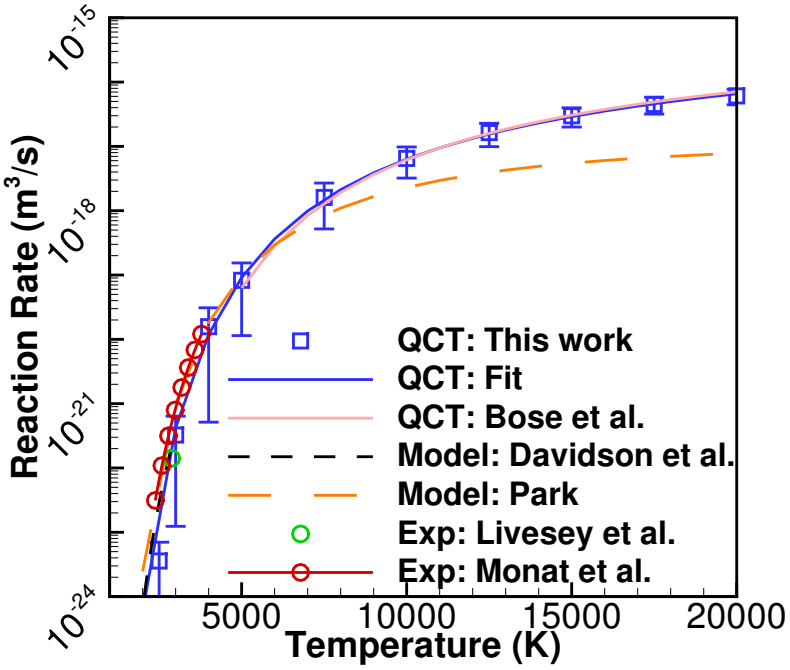

Figure 3.2. Comparison of $N_2 + O$exchange reaction rates

PESs. A possible reason is the missing O-insertion mechanism, which contributes to the reaction.

By comparing Fig.3.2 and 3.1, it can noticed that below a saturation temperature near 20,000K , the dissociation reaction rates are two orders of magnitude lower than exchange reaction rates. However, once the temperature becomes higher, dissociation reaction starts happening. This switching mechanism is essential for the modeling of cross sections, which will be shown in Chap.4.

3.2 State-specific Exchange Reaction Rates

In most shock tube experiments and shock dominated flows, there is a strong thermal nonequilibrium due to the finite-rate of internal energy relaxations. Under such conditions, the internal energy distribution no longer follows Boltzmann equilibrium distribution. Approximate forms of distributions can obtained by assuming the exis-

tence of quasi-steady state (QSS). It is well known that the QSS region of vibrational relaxation behind a shock wave can be characterized by a vibrational temperature, T_v different from the gas translational temperature T. One vibrational distribution function(VDF) commonly used when vibrational-vibrational(VV) energy exchange is dominant is Treanor VDF [62]. However, Treanor VFD doesn't take the depletion at high vibrational level due to rapid dissociation into account. [63]. In these years, there is a trend to solve complete master equations for all rovibrational levels to get accurate distribution functions and species concentrations. [64, 65] These calculations require a complete set of state-specific energy exchange and reaction rates. Although the calculation is still impracticable for engineering due to the calculation cost, it is valuable for theoretical study of nonequilibrium relaxation, like the calculation of relaxation time.

In this work, the QCT calculated state-specific exchange reaction rates based on Gamallo *et al.*'s $^3A''$ PES are compared with Akpinar *et al.*'s calculations based on Gamallo *et al.*'s $^3A''$, $^3A'$ PESs [26] and Bose and Candler's results based on Walch and Jaffe's $^3A''$ and $^3A'$ PESs [23]. The comparison of state-specific reaction rates, $k_{EX}(T, v, J)$ with Bose and Candler's results is shown in Fig.3.3. T equals 10,000K and $v = 0, 2, 6, 12, 20, 30$ and $J = 0, 20, 40, 60, 80, 100, 120, 150$. Four thousand trajectories are sampled for each rovibrational states. It can be found an increase of rotational level from 0 to 30 brings the state-specific reaction rates up by almost 3 orders of magnitude for ground vibrational level. However, for high vibrational level, this effect becomes weaker due to an increase of dissociation collisions. For instance, rovibrational state $(v, J) = (30, 150)$ is a quasi-bond state, therefore the rate is almost same as its value at $(v, J) = (20, 150)$. On the other hand, there exists strong vibrational favoring for exchange reaction as the rates differ by more than 2 orders of magnitude for $v = 0$ and $v = 30$. Comparing the results with Bose and Candler's data, our calculations generally underestimates the rates by less than 10%, which is consistent with the lack of $^3A'$ in calculation and the additional O-insertion mechanism. In table 3.1, the specific value of rates are compared. As it can be seen the

Table 3.1. Comparison of state-specific rates for T=10,000K. Rates are given in $\log_{10}(k)cm^3/s$

v	J	Akpinar *et al.*	Bose and Candler	This work	Error
5	0	-11.2	-11.5	-11.6781	4.27%
5	20	-11.2	N/A	-11.5429	3.06%
20	0	-9.95	-10.2	-10.4214	4.74%
20	20	-9.91	N/A	-10.3685	4.63%

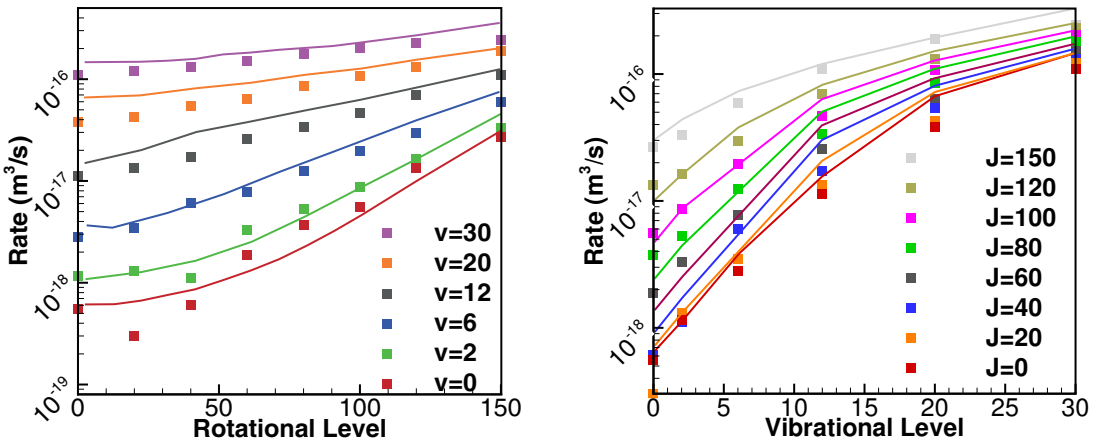

(a) Variation of rates with rotational level

(b) Variation of rates with vibrational level

Figure 3.3. Comparison of state-specific exchange reaction rates at temperature T = 10,000K. Solid lines: Bose and Candler's fit; Symbols: our result

relative error of log value of our calculation to Akpinar *et al.*'s results are less than 5%. These comparisons confirm that for QCT calculation of temperature around 10,000K, neglecting $^3A'$ PES shouldn't influence the result much.

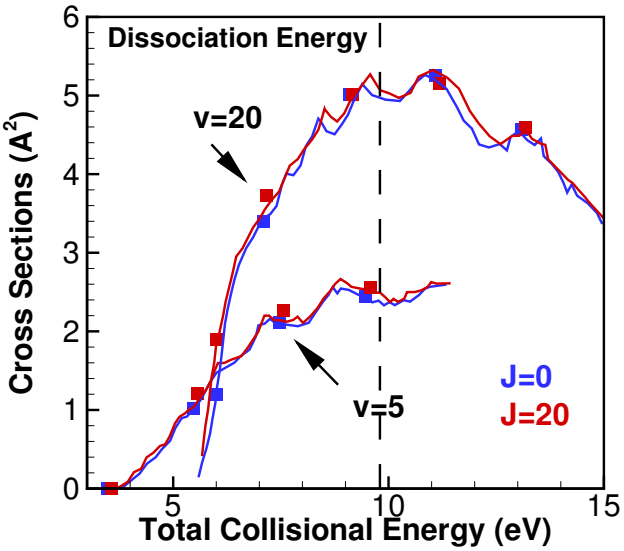

Figure 3.4. Comparison of exchange reaction cross sections with Akpinar *et al.*'s results for $^3A''$ PES. Lines: data extracted from Ref. [26]; Symbols: this work.

3.3 Exchange Reaction Cross Sections

Exchange reactions cross sections are compared with Akpinar *et al.*'s work. [26]. They conducted quantum wave-packet method and QCT calculations for exchange reaction based on Gamallo *et al.*'s PES. In the reference, limited data points are provided. We extract the QCT calculation results for $v = 0, 20$ and $J = 0, 20$ and show the comparison in Fig.3.4. Different from the figure in Ref. [26], the cross sections are plotted with total collisional energy, $E_c = E_t + E_{rv}$,as horizontal axis which makes the energy barrier clear. It can be found that the results agree with Akpinar *et al.*'s QCT data perfectly with the difference less than 0.1 A^2. The increase of vibrational level from 0 to 20 makes the cross sections doubled. However, rotational favorance is not strong for J less than 20 as the cross sections almost don't change if J is increased from 0 to 20. Although we find that there is no energy barrier for the exchange reaction along MEP in Sec.2.1.1, the calculations for $v = 20$ shows an energy barrier

larger than the endothermicity of the reaction, 3.26eV. An explanation is that the reaction mechanism switches from N-abstraction to O-insertion along MINI1-TS1. [26]. It implies that the reaction cross sections should be modeled with an effective activation energy dependent on internal states instead of a constant activation energy. In addition, a dropping of cross sections at dissociation limit can also be found in Fig.3.4. More detailed reaction cross section calculations and modeling methods will be presented in Chapter 4.

3.4 Vibrational Excitation and Relaxation

As it has been discussed in Chapter 1, thermal-chemical nonequilibrium is an important effect in high temperature gas dynamics. Several conditions including small geometries, high speed flow with inadequate molecular collisions and etc. could generate nonequilibrium. Compared to rotational energy, vibrational energy of molecule usually takes a longer time to reach equilibrium condition. Thus, vibrational excitation and relaxation is more dominant for modeling of nonequilibrium gas. There are mainly two categories of experimental data on vibrational excitation/relaxation. The first category is vibrational relaxation time, which describes the bulk equilibrium process of vibrational energy. The second category covers transition probability or rate constants, which could describe state-specific transition process. Relaxation time and state-specific rates will be discussed separately for $N_2 + O$ collisions in this section.

Relaxation time is an important factor to describe vibrational relaxation process. Following Landau-Teller vibrational relaxation model [66], it is assumed that the rate of vibrational energy relaxation is linearly proportional to its deviation from local equilibrium. The mathematical description is the following:

$$\frac{dE_v}{dt} = \frac{E_{v,Eq}(T) - E_v}{\tau_V}, \tag{3.4}$$

where $E_{v,Eq}(T)$ is the equilibrium vibrational energy at temperature T, and τ_V is the relaxation time. There are two widely used models for relaxation time. One is the

Millikan-White expression [67], which comes from the fitting of experimental results to the following expression:

$$p\tau_V = \exp[A(T^{-\frac{1}{3}} - 0.015\mu^{\frac{1}{4}}) - 18.42], \tag{3.5}$$

where p is the total pressure and μ is the reduced mass of collisional particles. The other one comes from the solution of state-to-state transition master equation with assumptions that 1) only monoquantum vibrational transitions are important, 2) the vibrational energy levels follow the harmonic oscillator (HO) distributions, $E_i = ih\nu$ and 3) rates for excited states can be related to the rate for the ground state via the Pauling and Wilson expression for harmonic oscillators, $k_{i,i-1} = ik_{1,0}$ [68]. By solving the system of kinetic equations for the non-equilibrium vibrational distribution function, the relaxation time can be given as Landau-Teller relation:

$$p\tau_V = \frac{kT}{k_{1,0}(1 - \exp(-h\nu/kT))}. \tag{3.6}$$

However, either of the methods is limited by unavailability of experimental data or the inaccurate assumptions for molecules under strong vibrational nonequilibrium. In this work, we get the relaxation time by first solving state to state master equations and then fitting the histogram of vibrational energy to Landau-Teller model.

The master equation describes the changing of particles' concentration in time by relaxation/excitation rates. If reactions are neglected, considering gas mixtures composed by N_2 and O, there exist two possible N_2 relaxation/excitation mechanisms:

$$N_2(v_i) + N_2(v_j) \underset{k_{N_2-N_2}(T,v_i',v_j' \to v_i,v_j)}{\overset{k_{N_2-N_2}(T,v_i,v_j \to v_i',v_j')}{\rightleftharpoons}} N_2(v_i') + N_2(v_j'), \tag{3.7}$$

$$N_2(v_i) + O \underset{k(T,v_i' \to v_i)}{\overset{k(T,v_i \to v_i')}{\rightleftharpoons}} N_2(v_i') + O, \tag{3.8}$$

where v_i, v_j are pre-collision vibrational states, v', j' are post-collision vibrational states, $k_{N_2-N_2}(T, v_i', v_j' \to v_i, v_j)$ and $k(T, v_i' \to v_i)$ are N_2 and O induced excitation/relaxation rates. If the number density of N_2 molecules at vibrational states

is N_v and the number density of atomic oxygen is N_O, the corresponding master equations are:

$$\frac{dN_v}{dt} = \sum_{v'} [-k(T, v \to v')N_v N_O + k(T, v' \to v)N_{v'} N_O]$$
$$-\sum_{v_j \neq v}\sum_{v_i' \neq v}\sum_{v_j' \neq v} k_{N_2-N_2}(T, v, v_j \to v_i', v_j')N_v N_{v_j} - 2\sum_{v_i' \neq v}\sum_{v_j' \neq v} k_{N_2-N_2}(T, v, v \to v_i', v_j')N_v N_v$$
$$+\sum_{v_i \neq v}\sum_{v_j \neq v}\sum_{v_j' \neq v} k_{N_2-N_2}(T, v_i, v_j \to v, v_j')N_{v_i} N_{v_j} + 2\sum_{v_i \neq v}\sum_{v_j \neq v} k_{N_2-N_2}(T, v_i, v_j \to v, v)N_{v_i} N_{v_j} \tag{3.9}$$

The rates $k(T, v \to v')$ can be calculated by averaging state specific over Boltzmann distribution as:

$$k(T, v \to v') = \frac{\Sigma_J\{[\Sigma_{J'} k(T, v, J \to v', J')]g_n(2J+1)\exp(-E_{v,j}(v, J)/kT)\}}{\Sigma_j g_n(2J+1)\exp(-E_{v,j}(v, J)/kT)} \tag{3.10}$$

This one automatically satisfies detailed balance:

$$k(v', J' \to v, J) = k(v, J \to v', J')\frac{2J+1}{2J'+1}\frac{g_n}{g_n'}\exp\left(\frac{E_{rv}(v', J') - E_{rv}(v, J)}{kT}\right). \tag{3.11}$$

However, it should be noticed that QCT calculations and calculated state to state rates have inherent statistical noise and truncation error which could lead to inaccurate equilibrium distribution functions. Usually, there is more noise for excitation rates than relaxation rates. To compensate for this, the excitation rates are recalculated by Eq.3.11 to force detailed balance satisfied. Since we don't have state-specific rate for $N_2 - N_2$ collision, all rates $k_{N_2-N_2}(T, v_i, v_j \to v, v_j')$ are equal to zero.

The master equation is solved for isothermal condition. Rotational energy is assumed to at equilibrium condition. The initial vibrational distribution is set as Boltzmann distribution characterized by a given vibrational temperature, T_v and translational, and rotational temperature T:

$$N_v(T_v) = \frac{\exp\left(-\frac{E_v(v)}{kT_v}\right)\sum_{J=1}^{Jmax(v)}(2J+1)\exp\left(-\frac{E_r(v,J)}{kT}\right)}{\sum_v \exp\left(-\frac{E_v(v)}{kT_v}\right)\sum_{J=1}^{Jmax(v)}(2J+1)\exp\left(-\frac{E_r(v,J)}{kT}.\right)} \tag{3.12}$$

where $E_r(v, J)$ is the rotational energy calculated as $E_r(v, J) = E_{rv}(v, J) - E_{rv}(0, J)$. During the calculation, quasi-steady-state is assumed and vibrational temperature is gotten from the equality of microscopic and macroscopic average vibrational energy:

$$E_{tot,v} = \sum_v E_v(v) N_v \tag{3.13}$$

$$E_{tot,v}(T_v) = \frac{\sum_v E_v(v) \exp\left(-\frac{E_v(v)}{kT}\right) \sum_{J=1}^{Jmax(v)} (2J+1) \exp\left(-\frac{E_r(v,J)}{kT}\right)}{\sum_v \exp\left(-\frac{E_v(v)}{kT_v}\right) \sum_{J=1}^{Jmax(v)} (2J+1) \exp\left(-\frac{E_r(v,J)}{kT_v}.\right)} \tag{3.14}$$

The total pressure is that as 1 atm and Moore fraction $X_{N_2} = 99\%$ and $X_O = 1\%$. To calculate relaxation time τ_{N_2-O}, an e-folding method [69] is used. Based on Landau-Teller model, the vibrational energy satisfies the following expression at isothermal condition:

$$\phi = \frac{E_v - E_{v,Eq}(T)}{E_v^0 - E_{v,Eq}(T)} = \exp\left(\frac{t}{\tau_{N_2}}\right) \tag{3.15}$$

where E_v is the average vibrational energy, $E_{v,Eq}(T)$ is the equilibrium vibrational energy, E_v^0 is the initial vibrational energy and τ_{N_2} is the total relaxation time. Thus τ_{N_2} is the time when $\phi = 1/e$. τ_{N_2} satisfies:

$$\frac{1}{\tau_{N_2}} = \frac{X_{N_2}}{\tau_{N_2-N_2}} + \frac{X_O}{\tau_{N_2-O}} \tag{3.16}$$

Since we assume rates $k_{N_2-N_2}(T, v_i, v_j \rightarrow v, v_j')$ are equal to zero, relaxation time $\tau_{N_2-N_2}$ equals infinity and τ_{N_2-O} can be calculated as:

$$\tau_{N_2-O} = X_O \tau_{N_2} \tag{3.17}$$

The master equations in Eq.3.9 are ordinary differential equations. They are solved by Runge-Kutta integration in this work. To get the variation of relaxation time with equilibrium temperature, T, master equations are solved with T ranging from 3,000K to 20,000K. The initial vibrational temperature, T_v^0 is always kept at 300K and total pressure, p, equals 1 atm, which represents gas subjected to sudden heating, like the environment behind a strong shock during high speed entry. The time evolution of vibrational temperature for T = 3,000K and 10,000K is shown in Fig.3.5(a). The

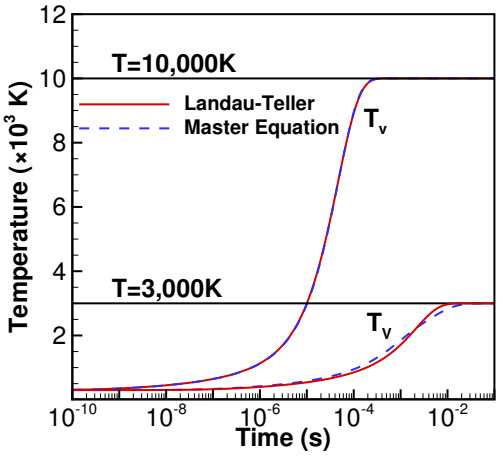

(a) Temperature history

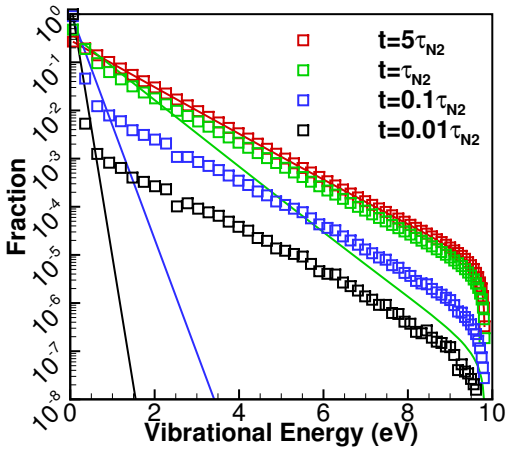

(b) Time evolution of vibrational energy distribution for T=10,000K

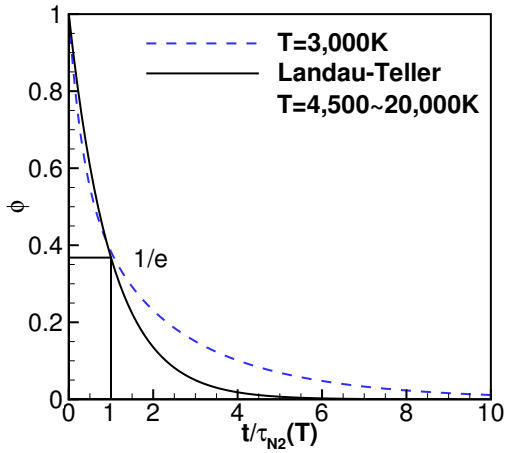

(c) Time evolution of deviation from equilibrium

Figure 3.5. Master equation solution of temperature variation, vibrational energy distribution and deviation from equilibrium state

dashed blue line is master equation solution and the solid black line is the analytical solution of Eq.3.15 with τ_{N_2} gotten by e-folding method. It can be found that for temperature as high as 10,000K, the simple Landau-Teller relation could predict quite accurate vibrational temperature with only one relaxation time, τ_V. However, when the temperature drops to 3,000K, Landau-Teller model predicts slower relaxation at the beginning and faster relaxation later. Similar effect has been found by Kulakhmetov *et al.* in their comparison of DSMC calculation with TCE and QCT based models for $O_2 + O$ system. [12] Such behavior can be found more clearly in Fig.3.5(c) which plots the time scaled by vibrational relaxation time, τ_{N_2} with ϕ defined in Eq.3.15. Except T =3,000K, all other curves collapse with the analytical solution. It takes more than $10\tau_{N_2}$ for T = 3,000K to get equilibrium, compared to others, around $6\tau_{N_2}$. Thus, state-specific calculation is considered important for low temperature VT transition modeling. Time evolution of vibrational energy distribution (VDF) for $T = 10,000$K is shown in Fig.3.5(b). The symbols are solutions of master equations and the lines are VDF with quasi-steady state assumption. At the beginning, the lower levels are frozen at initial vibrational temperature and the higher levels are governed by the translational temperature. As relaxation proceeds further, the higher levels are gradually populated and they are still thermalized by translational temperature. But the lower levels are governed by intermediate temperature. It confirms the unavailability of modeling internal state distribution by only vibrational temperature and translational temperature. In addition, it should be noticed that the assumption of quasi-steady state Boltzmann liked distribution always under predict the population of higher level, which will influence the prediction of dissociation reaction and ionization.

A comparison of relaxation time is shown in Fig.3.6. The experimental data include Eckstrom's results [70] for temperature ranging from 1,200K to 3,000K and Breshears and Bird's [71] results for temperature ranging from 3,000K to 4,500K. They both used incident shock tube. However the lowest temperature of Breshears and Bird's result was limited by fluctuation in the schlieren signal, which was improved

by Eckstrom with CO tracer technique. Fisher and Bauer [72] used a curve-crossing model to predict the relaxation time at high-temperature. It can be found that master equation predicts similar results to the extrapolation experimental measurement at temperature higher than 10,000K. However, it overestimates the relaxation time by more than an order of magnitude for temperature below 5,000K. Such effect has also been found by QCT calculation done by Esposito and Armenise [73] and quantum mechanics calculations done by Ivanov *et al.* [74]. This is mainly because that QCT calculation assumes all collisions happen electronically adiabatically. The assumption is good for chemical reactions since there usually exists high energy barrier blocking the reaction to proceed on excited electronic states. However, vibrational relaxation can occur as a result of electronically nonadiabatic transitions between intersecting vibronic surfaces. [75, 76] The vibronic surfaces for collinear configuration of $N_2(X^1\Sigma_g^+)$ colliding with radical $O(^3P)$ are shown in Fig.3.7. It can be found that the vibronic surface for $N_2O(^3A'')$ state is much flatter than $N_2O(^3A')$ state. The vibronic surface of $N_2O(^3A')$ for $v = 0$ crosses with both $v = 0$ and $v = 1$ of $N_2O(^3A'')$ state. Considering a colliding pair with N_2 at ground vibrational state, if the collision processes initially on $^3A'$ PES, the nitrogen will be more easily excited to $v = 1$ on $^3A''$ PES through the crossing point than $v = 1$ on $^3A'$. Thus the electronically nonadiabatic transition provides an additional mechanism for VT relaxation. Since we don't consider $^3A'$ PES and electronically nonadiabatic transition in this work, it's reasonable that the predicted relaxation time is longer than experimental measurements for low temperature. A comparison of monoquantum VT relaxation rates is also shown in Fig.3.8. Ivanov *et al.* performed quantum mechanical calculation for $^3A'$ PES and found the rate is of the order of $2 \times 10^{-20} m^3/s$. [74] Experimental data are calculated from relaxation time [70, 71, 77] by Eq.3.6. As it is expected, the electronically adiabatic calculation are around one order of magnitude lower than experimental measurement even if the rates of $^3A'$ and $^3A''$ PES weighted by electronic degeneracy are added together. A better match can be gotten by using surface hopping method [53] to take the electronically nonadiabatic transition among the triplet

states into consideration, which is currently beyond the aim of this work. The VT transition rates get closer to the extrapolation of experimental measurement, which may because chemical reactions become dominant at $T > 5,000K$.

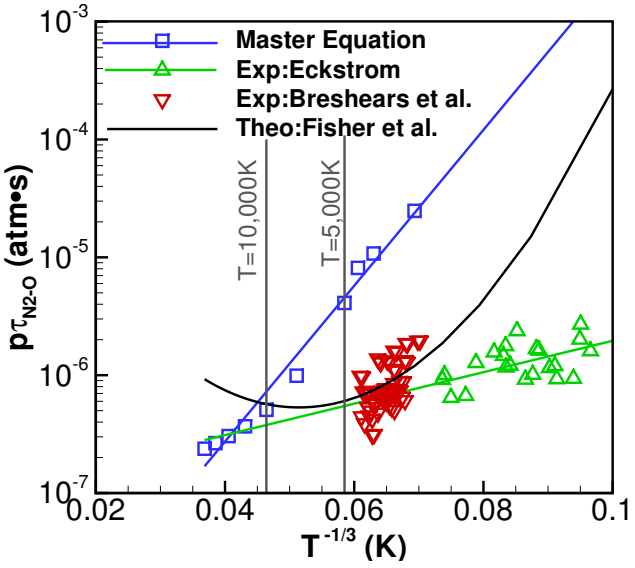

Figure 3.6. Comparison of relaxation time for $N_2 + O$ collisions

In addition, results predicted by Schwartz-Slawsky-Herzfeld (SSH) theory [78] and forced harmonic oscillator (FHO) [79–81] model are also compared in Fig.3.8 and Fig.3.9. Both of the models are based on the semi-classical solution of an harmonic oscillator moving under an exponential PES, $V(r) \sim \exp(-\alpha r)$. FHO provides an analytical nonpertubative solution than SSH theory, which makes it able to calculate accurate multi-quantum VT transition. The potential energy parameter α equals $3.31A^{-1}$ [82] in our cases and all other parameters are kept same as Adamovich *et al.*'s work. [80, 83]. Surprisingly, it can be found that although FHO model could predict similar dependence of monoquantum transition rates on temperature to QCT results, it over predicts the monoquantum transition rates by an order of magnitude. It also over predicts the decrease of the difference between different monoquantum VT rates as temperature increases. It is mainly because: (1) 1D-FHO model only

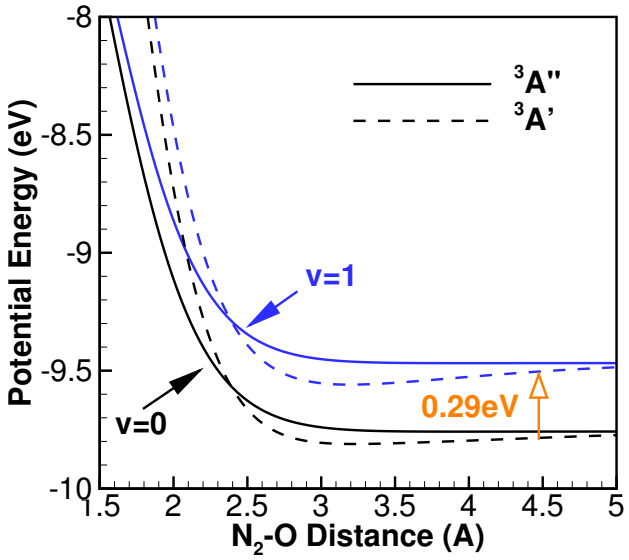

Figure 3.7. Vibronic surfaces for collinear configuration of $N_2(X^1\Sigma_g^+) + O(^3P)$

considers collinear collision and uses a constant steric factor to account 3D collisional effect. However, it can be found in Fig.3.10 that for non-collinear collisions, translational-internal energy transfer can happen efficiently for large impact parameter of vibrational excited states. (2) 1D-FHO model neglects vibrational-rotational coupling. In Fig.3.10, an increase of rotational level from $J = 0$ to $J = 100$ makes the average energy transfer become almost half of it original value. These two effects are taken into consideration by the new FHO-free rotational (FHO-FR) model [84–86]. Due to the complexity of the model, it is not compared here but future work will focus on the validation of FHO-FR model for $N_2 + O$ VT transition.

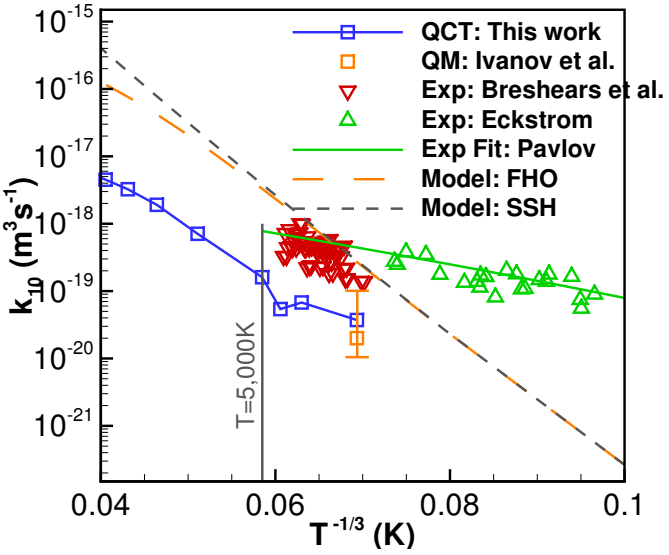

Figure 3.8. Comparison of monoquantum transition rate k_{10} for $N_2 + O$ collisions

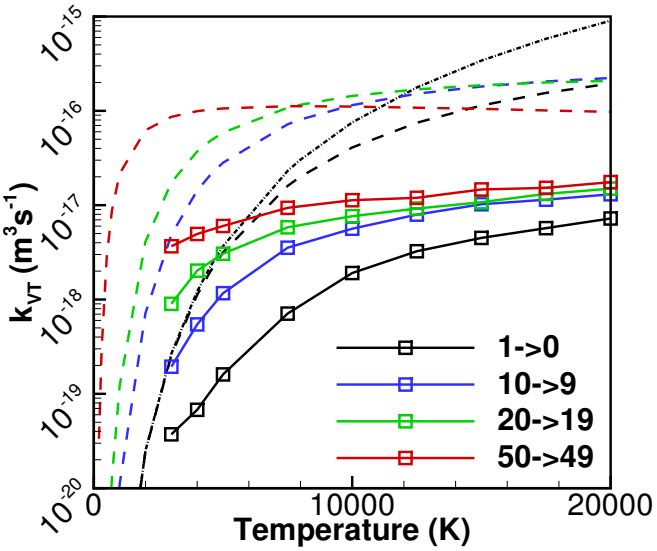

Figure 3.9. Comparison of monoquantum VT transition rate:solid lines: QCT results; dashed lines: FHO model; dash-dotted line: SSH theory

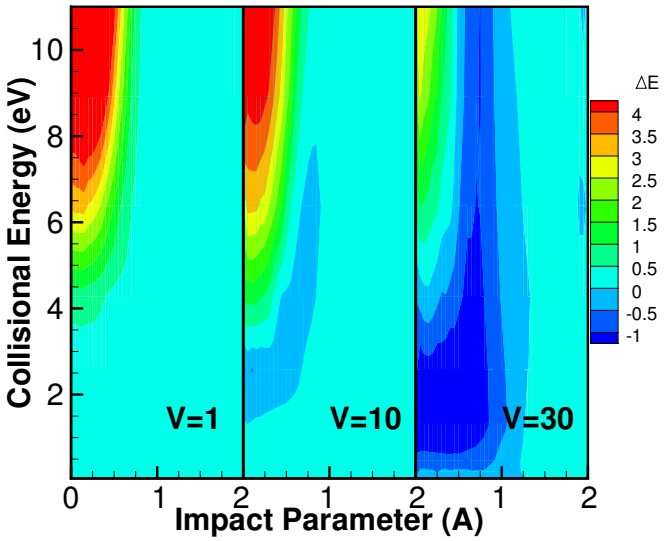

Figure 3.10. Comparison of translational-internal energy transfer for different vibrational level, $J = 0$

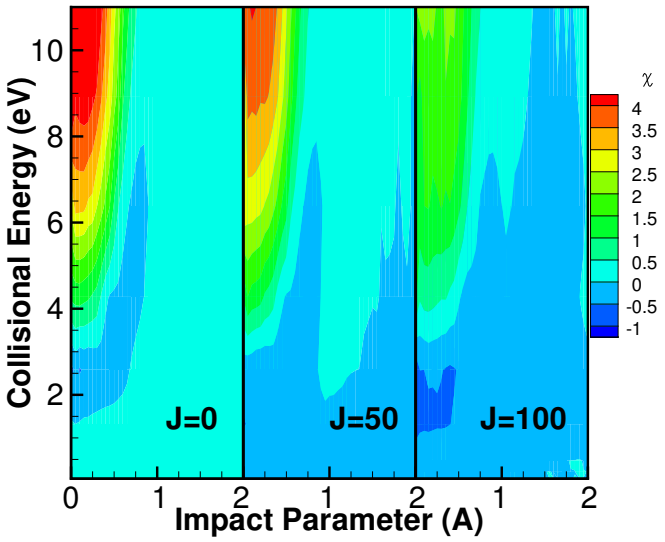

Figure 3.11. Comparison of translational-internal energy transfer for different rotational level, $v = 1$

4. DEVELOPMENT OF STATE-SPECIFIC CROSS SECTION MODELS

QCT calculations provide us with a large set of data including cross sections and rate for different energy transfer modes. Taking our case of N_2 colliding with O as an example, there exist 9751 rovibrational states for N_2 and 7321 rovibrational states for NO. The possible energy transfer modes including non-reaction collision (VRT transition), exchange reaction and dissociation reaction contain more than 10^8 ways of energy transfer. If we only consider VT transition and reaction, there still exists more than 10^4 energy transfer channels. If cross sections are stored as double precision, the size of data tabulated for N_{Et} translational energy bins will be $64bit \cdot 10^8 N_{Et} \approx 8GB \cdot N_{Et}$. With more gas mixtures taken in to consideration, the data volume will increase dramatically. In the past, researchers focused on speeding up processors following the Moore's Law to cope with the increasing volumes of data. However, a fundamental shift underway is the data volumes is scaling faster than compute resources and CPU speeds are static [87]. When the data are used in parallel CFD and DSMC calculation, massive message communication will further reduce the efficiency.

There are mainly three kinds of methods to combine QCT with DSMC or CFD flowfield calculation. The first approach is to fit cross sections calculated by QCT method to phenomenological models like TCE model [8] and integrate it to get reaction rate. The advantage of this approach is that no modification is needed for the existing code. But it could't make sure the model reproduces same Arrhenius rates and relaxation process. The second approach is to use an interpolated state-to-state transition and reaction cross sections look-up table [9,88]. However, the look-up table is hard to scale up to multiple species due to the large memory storage. This approach

is more suitable for verification of reduced state-resolved model. Another approach is hybrid Classical Trajectory Collision(CTC)-DSMC calcultion, which replaces phenomenological collision models by trajectory calculations [13, 89–91]. This method avoids the calculations of large number of trajectories for Monte Carlo integration in QCT and provides an intermediate method between DSMC and Molecular Dynamics. However, the computational efficiency requires simpler PES, which contradicts to demand of the accuracy. In addition, the method couldn't be applied to CFD simulations.

In the present work, vibrational-translational (VT) transition model is first built based on the idea of maximum entropy for $O_2 + O$ collisions [28]. The model could provide quite accurate state-to-state transition cross sections with limited numbers of coefficients and be applied easily in DSMC code. It also reproduces the state-to-state relaxation rate by including the rate during fitting. Then a preliminary state-specific exchange (SSE) cross sections model for $N_2 + O \rightarrow NO + N$ reaction and state-specific dissociation(SSD) cross sections model for $N_2 + O \rightarrow 2N + O$ reaction are built. The models could reproduce vibrational favoring effect, nonequilibrium factor and the reaction switching mechanism at dissociation limits.

The remain parts of this chapter will first introduce the maximum-entropy consideration and the formation of ME-QCT-VT model for $N_2 + O$ collision. Then the two reaction models are introduced with the comparison of rates to other avaible models.

4.1 Nonreaction Energy Exchange Model

4.1.1 Maximum Entropy Consideration

Maximum entropy consideration was originally proposed by Levin and Bernstein [45] and extended by Procaccia and Levin [92]. The main idea of maximum entropy consideration is that the relaxation or chemical reaction processes always happens in the trend to maximize the entropy of the system. Related models have been applied to CFD [93, 94], DSMC [95–97], and master equation [64, 65]. Considering the final

quantum states distributions of a system is characterized by function $P(f)$ (f is a nondegenerate state). If there are N_f possible states, the entropy is:

$$S = -\sum_{f}^{N_f} P_f \ln(P_f) \tag{4.1}$$

The distribution must normalized, i.e. the distribution P_f is subject to the zero-order-momentum constraint (E_f is the energy of f quantum state):

$$C_0(P_f) = \sum_{f=1}^{N_f} (E_f)^0 P_f = 1 \tag{4.2}$$

P_f can be solved by maximizing Lagrange function:

$$L(P_f, \lambda) = S - C_0(P_f) = -\sum_{f=1}^{N_f} P_f \ln(P_f) - \lambda \left(\sum_{f=1}^{N_f} P_f - 1 \right) \tag{4.3}$$

and the result is:

$$P_f^0 = \exp(-\lambda - 1) = 1/N_f; \tag{4.4}$$

Equation 4.4 shows that with zero-order-momentum constraint, all the post collision quantum states are equally likely. Let $g(v)$ be the degeneracy of quantum state v, then the corresponding distributions of the degenerated states are:

$$P_f^0 = P_v^0/g(v), \quad P_v^0 = \frac{g(v)}{\sum_v g(v)} \tag{4.5}$$

The distribution in Eq.4.5 is also called as prior distribution. It is the distribution of maximal entropy subjected to the ever present constraints (e.g. normalization, conservation of energy). The original prior distribution proposed by Levin and Bernstein [45] is based on the simplified assumption of quantum states. The degeneracy for translation mode is obtained from the solution of Schrödinger wave equation for particles in rectangular box [98] as:

$$g_T(E_t) = \frac{\mu^{3/2}}{\sqrt{2}\pi^2\hbar^3} \sqrt{E_t}. \tag{4.6}$$

The harmonic oscillator solution for rigid rotor shows the rotational mode has degeneracy for state J:

$$g_J(J) = 2J + 1. \tag{4.7}$$

If nuclear spin is not taken into consideration, the total degeneracy for nonreaction collision product $AB(v', J') + C$ can be written as:

$$g(v', J', E_c) = C(2J' + 1)\sqrt{E_c - E_{v'} - E_{r'}}, \tag{4.8}$$

Denote the rotation inertia of molecule AB as I, then the rotational energy is

$$E_{J'} = \frac{\hbar^2}{2I} J'(J' + 1) \tag{4.9}$$

Thus the degeneracy for vibrational mode alone can be obtained by integrating Eq.4.8 with respect to $E_{J'}$:

$$g(v', E_c) = C \int_{E_{J'}=0}^{E_{J'}=E_c-E_{v'}} \mathrm{d}E_{r'} \cdot \frac{\hbar^2}{2I} \sqrt{E_c - E_{v'} - E_{J'}} = C'(E_c - E_{v'})^{3/2} \tag{4.10}$$

Finally, the prior distribution can be obtained from Eq.4.5 and 4.10:

$$P_0(v', E_c) = \frac{g(v', E_c)}{\sum_{v'} g(v', E_c)} = \left(1 - \frac{E_v(v')}{E_c}\right)^{3/2} / \sum_{v'} \left(1 - \frac{E_v(v')}{E_c}\right)^{3/2}. \tag{4.11}$$

There also exist other kinds of prior distribution. Gallis and Harvey proposed to use an equilibrium distribution of collision pairs instead of single diatomic molecule [96]. The distribution is also know as Larsen-Borgnakke(LB) distribution for inelastic collision, which reassigns post collision energy based on degree of freedom (DOF). Bird generalized the model to the following form [99]:

$$P(E_a, E_b) = \frac{\Gamma(\zeta_a)\Gamma(\zeta_b)}{\Gamma(\zeta_a + \zeta_b)} \left(\frac{E_a}{E_a + E_b}\right)^{\zeta_a - 1} \left(\frac{E_b}{E_a + E_b}\right)^{\zeta_a - 1} \tag{4.12}$$

where ζ_a and ζ_b are the DOF for energy mode a and b. The DOF for translational energy is $\zeta = \frac{5}{2} - \omega$, which is selected based on variable hard sphere (VHS) or variable soft sphere (VSS) models in order to reproduce viscosity data. For vibrational-translational ($V - T$) energy exchange, assume vibrational energy is fully excited, then

$$P_0(v', E_c) = \left(1 - \frac{E_v(v')}{E_c}\right)^{3/2-\omega} / \sum_{v'} \left(1 - \frac{E_v(v')}{E_c}\right)^{3/2-\omega} \tag{4.13}$$

The above prior distributions will reproduce equilibrium post-collision states. However, there exist other constraints which limit the final entropy. The physical

explanation of the existence is because of different collision mechanics and features of PES. Thus, we can write the final entropy of the actual distribution in terms of the deviation from the prior one:

$$DS = S_{max} - S \tag{4.14}$$

where S_{max} can be calculated based on Eq.4.11,

$$S_{max} = -\sum_{v}^{N_v} P_v^0 \ln[P_v^0/g_v] = \ln[\sum_{v} g_v] \tag{4.15}$$

The the entropy deficiency is:

$$DS = \sum_{v}^{N_v} P_v \ln[P_v/g_v] - \sum_{v}^{N_v} P_v^0 \ln[P_v^0/g_v] = \sum_{v}^{N_v} P_v \ln[P_v/P_v^0] \geq 0 \tag{4.16}$$

We can further define a surprisal function based on information theory as the deviation of distribution from the equilibrium one which shows the difference for specific state:

$$I(v) = \ln\left(P_v/P_v^0\right) \tag{4.17}$$

The original surprisal function proposed by Levin Bernstein [45] is:

$$I(v) = \lambda_0 + \lambda_1 E(v) \tag{4.18}$$

It could be found the first part is used to normalize the distribution. The second part constrains the first-order-momentum, i.e. the average vibrational energy. Assume the average post vibrational energy is $\langle E_v \rangle$. We can maximize the Lagrange function with zero and first order momentum constrains to get the surprisal function:

$$L(P_v, \lambda_0, \lambda_1) = -\sum_{v}^{N_v} P_v \ln[P_v/g_v] - \lambda_0 \left(\sum_{v}^{N_v} P_v - 1\right) - \lambda_1 \left(\sum_{v}^{N_v} P_v E_v - \langle E_v \rangle\right) \tag{4.19}$$

which results in:

$$P_v = \frac{g_v}{\sum_v^{N_v} g_v} \exp(\lambda_0 + \lambda_1 E_v) \tag{4.20}$$

Gallis and Harvey further extended the work by including higher order momentum constraints [97]:

$$I(v) = \lambda_0 + \lambda_1 f_v + \lambda_2 f_v^2 + ... \tag{4.21}$$

where $f_v = E_v/E_C$. However, this model breaks micro-reversibility and has poor behavior near the threshold line for dissociation reaction. The optimized value coefficients for thermal rate lead to unphysical behavior with high vibrational energy [100]. Procaccia and Levin proposed a new function [92] $I_v = \lambda_v|E_v - E'_v|$. The function is generalized as [101]:

$$I(\Delta E) = \lambda_0 + \lambda|\Delta E|/kT, \tag{4.22}$$

where ΔE is the energy mismatch, i.e. the energy transfered into (or out of) translational energy. However, the changes of vibrational energy states $|\Delta v|$ in the cases Levin analyzed are usually less than 10. For N_2+O collisions with temperature higher than $5000K$, N_2 molecule is possibly excited or relaxed more than 10 levels. As shown later, the surprisal function for $|\Delta v| > 10$ does not develop linearly especially for the excitation tail.

4.1.2 ME-QCT-VT Energy Exchange Model

The first model proposed here is a state-specific vibrational and translational energy transition model (VT). The model is essential for describing vibrational relaxation and excitation for nonequilibrium flowfield calculations. The basic idea of the model comes from the ME-QCT-VT model proposed by Kulakhmetov [28] for $O_2 + O$ collision, which is introduced in previous section.An equilibrium post-collision distribution $P^0(v, E_t \to v')$ is first taken for VT process. In this case, we take LB distribution Eq.4.13. Then the surprisal function is calculated as:

$$I(v, J, E_t \to v') = \ln\left[\frac{\sigma_{QCT-VT}(v, J, E_t \to v')}{\sigma_{TOT} \cdot P^0(v, E_t \to v')}\right] \tag{4.23}$$

where σ_{TOT} is the total collision cross sections. Here we choose a form similar to VHS cross sections:

$$\sigma_{TOT} = \sigma_{ref} E_t^{\nu-1} \tag{4.24}$$

where σ_{ref} is a reference cross section and ν is model coefficient. The QCT calculated vibrational translational transition cross sections (QCT-VT) is gotten by summing up

all possible QCT calculated vibrational rotational translation cross sections (QCT-VRT).

$$\sigma_{QCT-VT}(v, J, E_t \to v') = \sum_{J'=1}^{J'_{max}} \sigma_{QCT-VRT}(v, J, E_t \to v', J'). \tag{4.25}$$

With above information, a preliminary idea of the surprisal function can be gotten. The surprisal function for initial state $v = 20, J = 0$ is plotted in Fig.4.1. It could be found there is strong favorance to small ΔE_v transition. The surprisal function drops exponentially near $\Delta E_v = 0$. There are mainly two possible reasons for this. First, the distribution function of impact parameter b is a linear increasing function, which means most collisions are glancing collisions. They are not efficient for energy exchange. The other reason is that the strong coupling of rotation-vibration energy makes molecule hard to break the vibrational barrier to be excited or relaxed. The favoring effect is also sensitive to translational energy. As it is shown in Fig.4.2, with translational energy increasing, translational-internal energy exchange becomes efficient at large impact parameter. Thus the slope of surprisal function at $\Delta E = 0$ decreases and the favoring effect becomes moderate.

Because the total collision energy is determined by the initial translational and ro-vibrational energy, it is expected there exists a maximum possible post-collision vibrational level. Thus for $\Delta E_V > 0$, the surprisal function decays asymptoticly to negative infinity near the limit. For extremely high energy collisions like $V_r = 0.11$ A/fs, $(v, J) = (20, 0)$, the total collision energy $E_c = E_t + E_{rv} = 11.4754$ eV is larger than dissociation limit $E_d = 9.8216$ eV. The surprisal function should be limited by dissociation energy since there is no possibility to get a post-collision vibrational energy higher than that. The surprisal function will collapse to same shape for these cases.

In addition, the ME-QCT-VT model has to satisfy micro-reversibility,

$$g_n g_J \mu E_t \sigma(E_c, v, J \to v', J') = g_{n'} g_{J'} \mu E'_t \sigma(E_c, v', J' \to v, J). \tag{4.26}$$

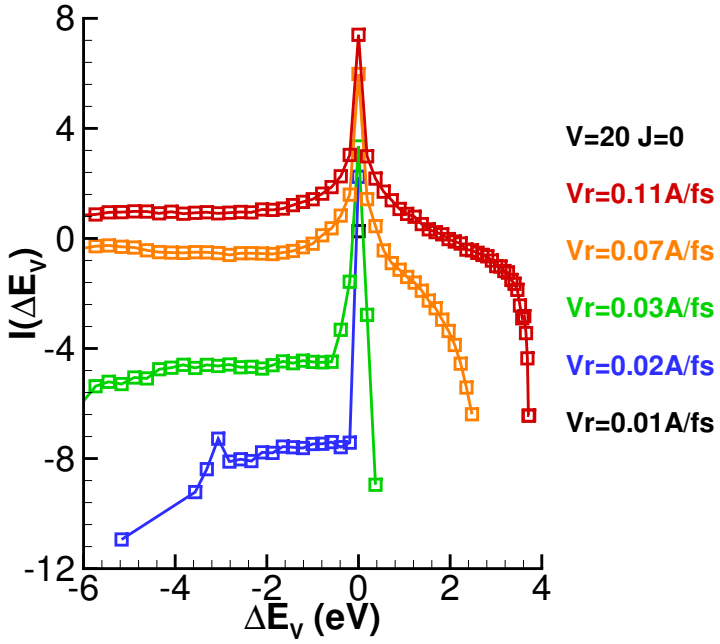

Figure 4.1. Surprisal function calculated by QCT method for $(v, J) = (20, 0)$. Preliminary coefficients $\sigma_{ref} = 39.8419A^2$, $\nu = -0.1951$

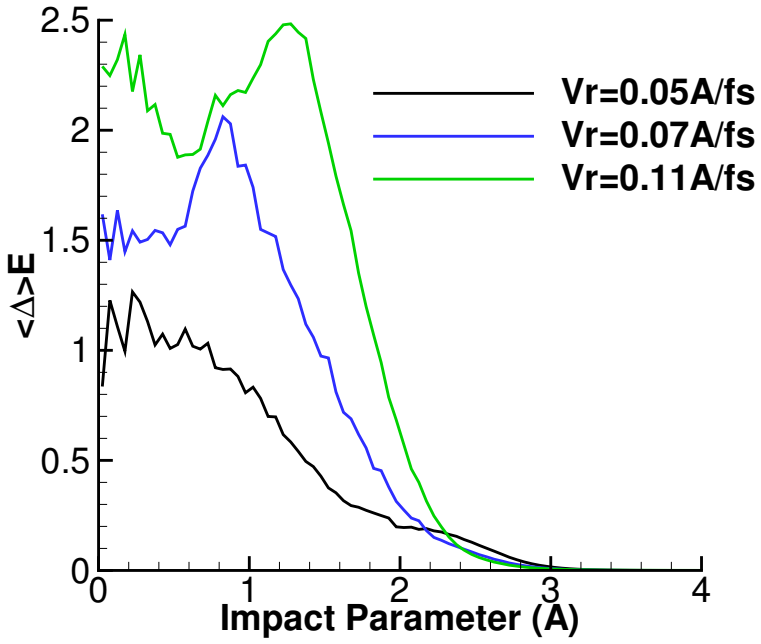

Figure 4.2. Average internal energy change v.s. impact parameter for non-reaction collision $(v, J) = (20, 0)$.

where g_n is the nuclear-spin degeneracy and g_J is the rotational energy degeneracy:

$$g_J = 2J + 1,\ g_n = \begin{cases} 6, & \text{if } J \text{ is even} \\ 3, & \text{if } J \text{ is odd} \end{cases} \tag{4.27}$$

μ is the reduced mass of collision pair, E_t is the translational energy involved in the collisions. $\sigma(E_c, v, J \to v', J')$ is the cross section for transition from the initial level (v, J) to the final level (v', J') with total collision energy E_c. Primed variables in this and all subsequent equations refer to post-collision states. By satisfying Eq.4.26, detail balance will automatically be satisfied and the system could relax to equilibrium if there only exist the forward and reverse collisions [102]. In the ME-QCT-VT model, we only consider VT transition. Although average VT transition cross sections weighted by equilibrium rotational energy distribution have been used by some researchers [103], we assume VT transition cross sections are same for different rotational energy levels with same vibrational and translational energy. This assumption has been verified by Kulakhmetov et al. [104] to work well with LB model for rotational energy in DSMC. Thus the micro-reversibility relation is reduced to:

$$E_t \sigma(E_c, v \to v') = E_t' \sigma(E_c, v' \to v). \tag{4.28}$$

The proposed form for the ME-QCT-VT model [28] is:

$$\sigma_{ME-QCT-VT}(E_c, v \to v') = \sigma_{ref} E_t^{\nu-1} \frac{\left(1 - \frac{E_v(v')}{E_c}\right)^{\nu}}{\sum_{v'} \left(1 - \frac{E_v(v')}{E_c}\right)^{\nu}} \exp\left(S_v(E_c, v, v')\right) \tag{4.29}$$

where E_t is the translational energy, E_v is the vibrational energy, E_c is the collision energy and S is the surprisal function. In the ME-QCT-VT model the total collision energy only counts for vibrational energy and translational energy $E_c = E_t + E_v = E_{t'} + E_{v'}$. Reference cross section, σ_{ref}, and the exponent, ν, parameters are fitted to QCT-calculated cross sections. With surprisal function equal to zero, Eq.4.29 automatically satisfies micro-reversibility. To maintain micro-reversibility $(S(E_c, v, v') = S(E_c, v', v))$, the surprisal function needs to be formulated by collision invariant variables including total collision energy E_c and change of energy

$|E_v(v) - E_v(v')|$ or constant like dissociation energy E_D. The proposed surprisal function has the following form:

$$S_v(E_c, v, v') = A|E_v(v) - E_v(v')| + B\exp\left(-\left|\frac{E_v(v) - E_v(v')}{C}\right|^D\right) + E\left[\frac{1}{1\text{eV}^2}(E_l - E_v(v))(E_l - E_v(v'))\right]^F \quad (4.30)$$

$$E_l = \min(E_c, E_D) \quad (4.31)$$

This surprisal function could reproduce the features we mentioned above about QCT observations. It tries to keep the constraint of average vibrational energy change by first term and vibrational favoring effect by second term. The last term works as a limit for the possible maximum post-collision vibrational energy level. To capture the influence of translational energy on vibrational favoring effect, the coefficients A, B and C are changed by total collision energy:

$$\begin{aligned} A &= A_1 + A_2 E_c, \\ B &= B_1 + B_2 E_c, \\ C &= C_1 + C_2 E_c. \end{aligned} \quad (4.32)$$

There are in total eleven coefficients fitted to QCT calculations. The details of fitting are discussed in Sec. 4.1.3. For the application of ME-QCT-VT to DSMC, benefited from the similarity to $O_2 + O$ model [105], it can be applied with the same method.For the application of ME-QCT-VT to CFD, state-to-state transition rates can be gotten by numerical integration of cross sections.

4.1.3 Model fit for $N_2 + O$ collisions

The ME-QCT-VT energy exchange model, presented in Eq.4.29, has eleven coefficients needed to be fitted to QCT calculations. These coefficients are optimized by Simulated Annealing algorithm. An error function defined as the following is minimized:

$$E_{Total} = E_{XSection} + W_{Rate} \cdot E_{Rate}. \quad (4.33)$$

The model error of both cross sections $E_{XSection}$ and state-to-state transitions rates E_{Rate} are counted. A weight W_{Rate} for state-to-state transition rate model error is set as 5 here. It aims to increase the model accuracy for rate since the error of rate is usually larger than that of cross sections.

The model error of cross sections is defined as the logarithm of relative error between QCT calculated cross sections and ME-QCT-VT modeled cross sections, i.e. $\log(\sigma_{ME-QCT-VT}/\sigma_{QCT-VT})$. The unbiased square error is gotten by summing up model error of all cross sections with the same initial state and dividing by the number of possible post-collision vibrational states (N_{vib}). This could avoid high energy collisions weighing higher than others since they are more possible to excite molecule to higher states or relax to lower states.

$$E_{XSection} = \sum_{E_t}\sum_{J}\sum_{v}\left[\frac{1}{N_{vib}}\sum_{v'\neq v}\left(\log\left(\frac{\sigma_{ME-QCT-VT}(v, E_t \rightarrow v')}{\sigma_{QCT-VT}(v, J, E_t \rightarrow v')}\right)\right)^2\right] \tag{4.34}$$

The QCT calculated cross sections $\sigma_{QCT-VT}(v, J, E_t \rightarrow v')$ we fit have the following initial conditions: The initial states considered in Eq.4.34 are:

$$\begin{aligned} v &= [0, 1, 5, 7, 10, 15, 20, 25, 30] \\ J &= [0, 20, 50, 100, 150] \\ V_r &= [1, 2, 3, 5, 7, 9, 11, 13] \text{ km/s} \\ E_t &= [0.0528, 0.2111, 0.4749, 1.3191, 2.5854, 4.2738, 6.3844, 8.9170] \text{ eV} \end{aligned} \tag{4.35}$$

The model error of rates are calculated as the summation of logarithm of relative magnitude:

$$E_{Rate} = \sum_{i}\sum_{v}\sum_{v'\neq v}\left|\log\left(\frac{k_{ME-QCT-VT}(v \rightarrow v', T_i)}{k_{QCT-VT}(v \rightarrow v', T_i)}\right)\right| \tag{4.36}$$

For the QCT results of rate, instead of numerically integrating cross sections , we directly sample collision velocities based on Boltzmann equilibrium distribution and integrate cross sections with respect to translational energy by *Monte-Carlo* integration in QCT code. Since the efficiency of Monte Carlo integration is not influenced by dimension, this method could provide smaller numerical error. It also reduces the

number of trajectories need to be calculated and avoid the calculation of all state-to-state transition cross sections. The VT state-to-state specific rates are calculated with the assumption of equilibrium rotational energy distribution:

$$k_{QCT-VT}(v \to v', T_i) = \frac{\Sigma_J\{[\Sigma_{J'} k_{QCT-VRT}(v, J \to v', J', T_i)] g_n g_J \exp(-\varepsilon_{v,J}/kT_i)\}}{\Sigma_J g_n g_J \exp(-\varepsilon_{v,J}/kT_i)} \tag{4.37}$$

where g_J and g_N are mentioned in Sec.4.1.2 , $\varepsilon_{v,J}$ is rovibrational energy of state (v, J) and $k_{QCT-VRT}(v, J \to v', J', T_i)$ is QCT calculated state specific transition rate from state (v, J) to (v', J') at temperature T_i. The ME-QCT-VT rate is calculated as the following:

$$k_{ME-QCT-VT}(v \to v', T_i) = \sqrt{\frac{8k_B T_i}{\pi\mu}} \int_0^{+\infty} \sigma_{ME-QCT-VT}(v \to v', E_t) \frac{E_t}{k_B T_i} \exp\left(-\frac{E_t}{k_B T_i}\right) \frac{dE_t}{k_B T_i} \tag{4.38}$$

where v and v' are the initial and final vibrational states. T_i is the temperature of interest and E_t is translational energy. μ is the reduced mass of collision pair and k_B is Boltzmann constant. Similar to the fit of cross sections, rate with $v = v'$ is not fitted. The rates are fitted for the transition with the following initial and final states.

$$\begin{aligned} v &= [0, 1, 5, 10, 20] \\ v' &= [0, 1, 5, 10, 20] \\ T_i &= [5000, 7500, 10000, 12500, 15000, 17500, 20000]\text{K} \end{aligned} \tag{4.39}$$

The optimized ME-QCT-VT model coefficients are presented in Table 4.1.3. Cross sections have the unites of Angstrom squared and all energies are presented in electron volts. Retrospectively, to account for the limitation that QCT calculations are done for one electronic states PES, we need to multiply the reference cross sections by electronic degeneracy with the assumption that electronic-excitation and nonadiabtic transition won't happen. We suggest using asymptotic $g_{elec}(T \to +\infty) = 1/3$ for ME-QCT-VT cross sections and Eq.2.71 for equilibrium ME-QCT-VT rate.

Table 4.1. Optimized ME-QCT-VT model coefficients

Coefficient	Value	
σ_{ref}	$24.2788 \cdot g_{elec}$	$A^2/eV^{\nu-1}$
ν	0.3994	-
A_1	0.1253	-
A_2	0.0221	eV^{-1}
B_1	5.8506	-
B_2	0.1398	eV^{-1}
C_1	0.2493	eV
C_2	-0.2075	-
D	0.6988	-
E	-5.0131	-
F	-0.0868	-
E_D	9.8216	eV
g_{elec}	1/3	

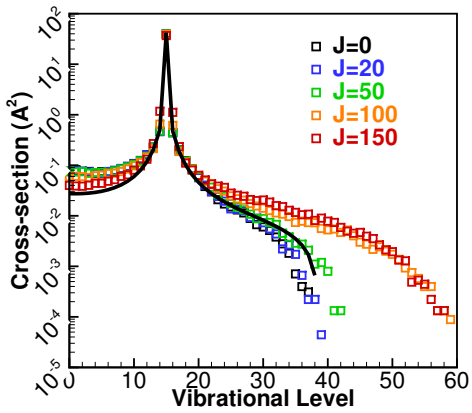

(a) $v = 15$, $V_r = 9km/s$, $E_t = 4.2738$eV

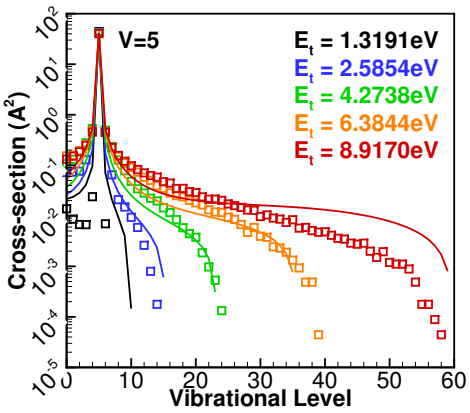

(b) $v = 5$, $J = 50$

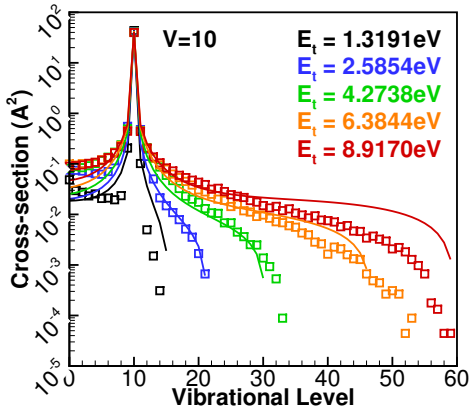

(c) $v = 10$, $J = 50$

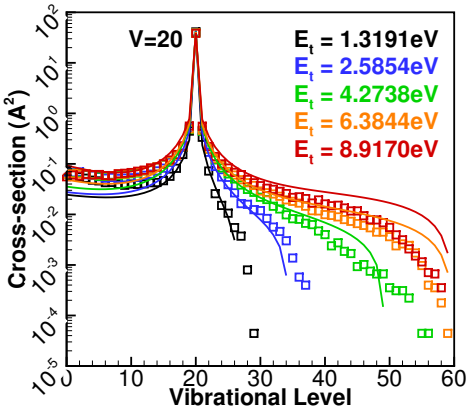

(d) $v = 20$, $J = 50$

Figure 4.3. Comparison of QCT-VT cross sections and fitted ME-QCT-VT cross sections. The solid lines are ME-QCT-VT predictions and symbols are QCT results. Initial conditions are in the captions.

4.1.4 Model Prediction

ME-QCT-VT predictions and QCT calculated results are compared in Fig.4.3. The former ones are shown with solid lines and the latter are shown with symbols. Fig.4.3(a) shows the comparison of QCT cross sections with different initial rotational levels J and ME-QCT-VT results. As it is expected, collisions with higher initial rotational level have more energy to dispose in vibrational mode, which results in larger cross sections for excitation ($\Delta v > 0$). Although the ME-QCT-VT model neglects the contributions of rotational energy to vibrational-translational energy exchange, it provides a satisfactory estimation of excitation cross sections for intermediate rotational levels. However, the model underestimates the relaxation cross sections. Fig.4.3(b), 4.3(c) and 4.3(d) show the comparison of cross sections with different initial collision velocity for vibrational level v equal 5, 10 and 20 and rotational level equal to 50. The ME-QCT-VT model reproduces the features including vibrational favoring for small Δv, the sensitivity of vibrational favoring to translational energy and the limit at $E_t' + E_v(v')$ approaching E_c or E_D. For $E_t \leq 4.2739$eV (i.e. $V_r \leq 9$km/s) , the model could predict cross sections quite accurately. For higher speed collisions, the model over predicts excitation cross sections. Considering the range of fitted collisional energy is more than two order of magnitude and collisions with $V_r > 9$km/s are mainly important for equilibrium temperature around 20,000K as the Boltzmann distribution shown in Fig.4.4 , the result is acceptable. In addition, the model could also predicts that VT cross sections for $E_t < 1.3191$eV are almost zero, which are not shown in the figure.

VT transition rates for temperature ranging from 5,000 K to 20,000 K are compared in Fig.4.5. For excitation rates ($\Delta v > 0$), Fig.4.5(a) shows that mono-quantum transition rate is more than two orders of magnitude higher than multi-quantum transition rates. The model error increases as temperature becomes lower than 7,500 K. But it is still less than an order of magnitude. Fig.4.5(b) shows the relaxation rates i.e. $\Delta v < 0$. According to QCT calculated results, mono-quantum transition rate is half

an order higher than multi-quantum transition rates. For temperature higher than 17,500 K, VT transition with lower initial vibrational level is easier to happen as the corresponding transition rate is higher. However, for temperature lower than 17,500 K, it presents different monotonicity. For example VT transition $v = 20 \rightarrow 0$ has transition rate twice the value of VT transition $5 \rightarrow 0$. ME-QCT-VT model doesn't capture the trend. It overestimates the rates for low temperature and underestimates the rates for high temperature by less than an order of magnitude. A better fit might be gotten by binning the translational energy and optimizing the model coefficients for each bin.

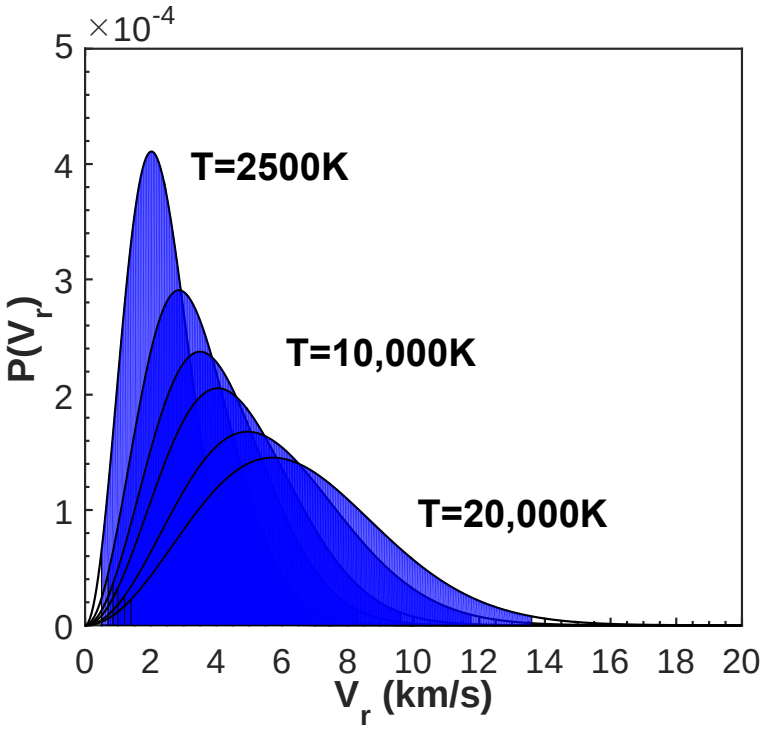

Figure 4.4. Boltzmann equilibrium distribution of collisional velocity

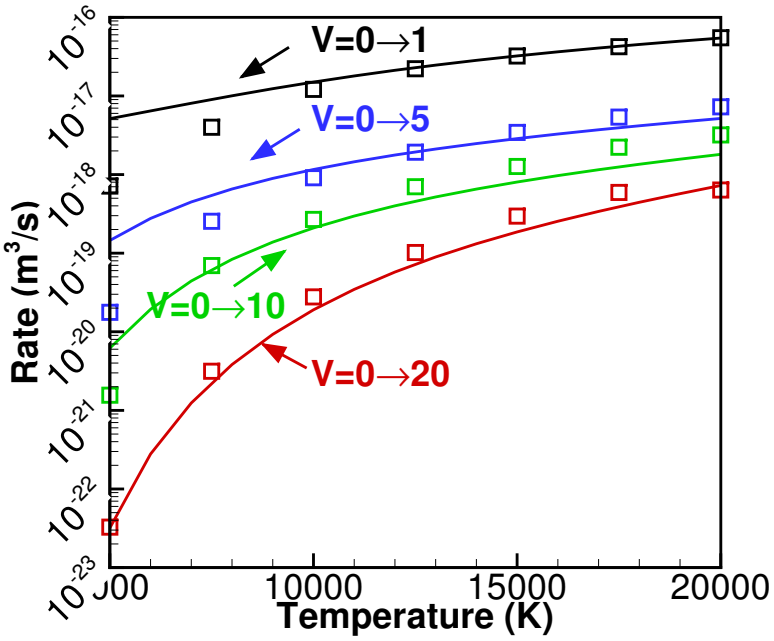

(a) Excitation from v=0 level

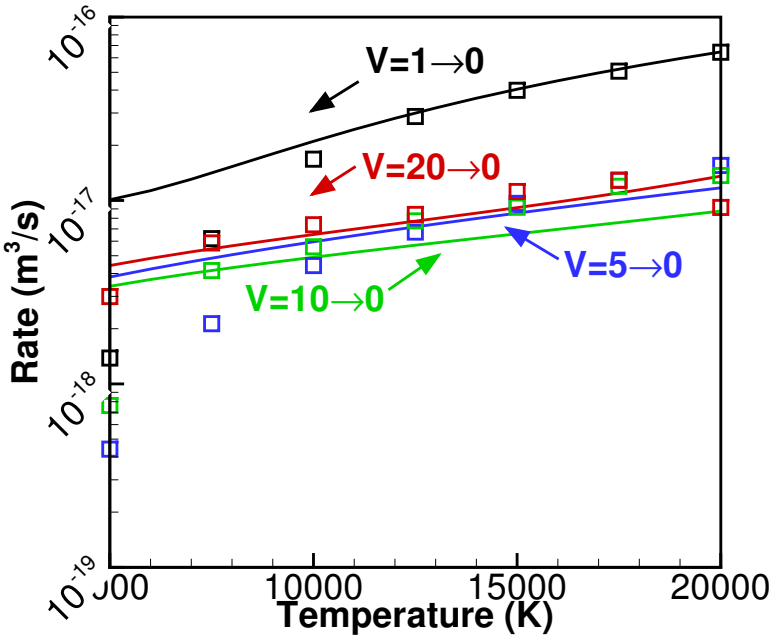

(b) Relaxation to v=0 level

Figure 4.5. State-to-state transition rates predicted by ME-QCT-VT model (shown by lines) and calculated by QCT method (shown by symbols) for equilibrium temperature ranging from 5,000 K to 20,000 K

4.2 State-Specific Reaction Cross Section Models

As it is discussed in Chapter 1, the Zeldovich reaction $N_2 + O \rightarrow NO + O$ and atomic oxygen induced dissociation $N_2 + O \rightarrow 2N + O$ play important roles in hypersonic nonequilibrium flow. Although the related studies have lasted for more than 20 years, there is still not much change for the models used in flowfield simulation. Taking DSMC as an example, total collision energy model (TCE) is still widely used although some problems have been mentioned by researchers including the assumption of continuous internal energy distribution [106], ambiguity of energy mode participating reactions, thermal nonequilibrium due to reaction product population [107] and *etc.* Comparisons of QCT calculated reaction cross sections and TCE modeled results are shown in Fig.4.6 and Fig.4.7. It can be found that TCE model is problematic at modeling state-specific reaction cross sections. There is an unphysical peak for exchange reaction cross sections at high vibrational energy level. It is because TCE model only considers total collision energy. There is possibility that internal energy is already larger than activation energy but translational energy is almost zero, which results in infinite collision cross sections. Besides, TCE model doesn't predict the vibrational favoring effect.

It should be noted that as a phenomenological model, TCE provides a feasible method to model equilibrium chemical reaction with only Arrhenius rates parameters. However, in order to simulate high temperature nonequilibrium flow accurately, better state-specific models are needed.

4.2.1 State-Specifc Dissociation Model

The $N_2 + O \rightarrow 2N + O$ dissociation reaction is studied first in this work. We calculated dissociation cross sections and rates using the QCT method with translational energies ranging between 0.1 eV and 23 eV, rotational levels [0,20,50,100,150] and vibrational levels [0,1,5,7,10,15,20,25,30,50,55]. A survey of selected cross sections is presented in Fig.4.8. The dissociation cross sections exhibit both vibrational and

rotational favoring. Dissociation cross sections for the 30th level is 5 to 10 times

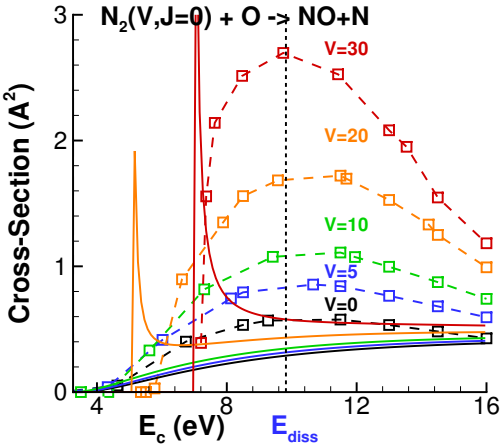

Figure 4.6. Comparison of TCE and QCT exchange reaction cross sections. Dashed lines and symbols: QCT result. Solid lines: TCE. Initial rotational level $J = 0$ for all the cases

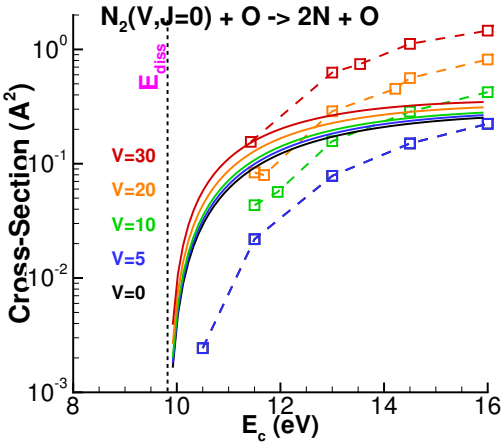

Figure 4.7. Comparison of TCE and QCT dissociation reaction cross sections. Dashed lines and symbols: QCT result. Solid lines: TCE. Initial rotational level $J = 0$ for all the cases

higher than for the ground level. These cross sections can be accurately fit to the state-specific dissociation model proposed by Kulakhmetov *et al.* [11]:

$$\sigma_D(v, J, E_c) = \begin{cases} 0, & \text{if } E_c \leq D \\ A(v, J)(E_c/D)^{\alpha_1(v,J)}(1 - D/E_c)^{\alpha_2(v,J)}, & \text{if } E_c > D \end{cases} \tag{4.40}$$

In Eq.4.40, D and E_c are dissociation and total collision energy respectively. The total collision energy includes pre-collision translational, rotational and vibrational energies, $E_c = E_t + E_v + E_r$. The coefficients: A, α_1, and α_2, are fit at fixed vibrational, v, and rotational, J, levels using the simulated annealing algorithm. The fitting function used in this work is:

$$E(v, J) = \sum_{E_c} \left[\sigma_{QCT-SSD}(v, J, E_c) - \sigma_{QCT}(v, J, E_c)\right]^2, \tag{4.41}$$

where $\sigma_{QCT-SSD}$ are modeled cross sections and σ_{QCT} are cross sections calculated directly by QCT. The summation in Eq.4.41 is over all available translational energies at a given rovibrational levels. The fit coefficients are linearly interpolated for intermediate levels. These coefficients for the $N_2 + O \rightarrow 2N + O$ reaction are presented in Table 4.2 through and 4.4. Note that the coefficient A in table 4.2 is explicitly divided by 3 to compensate for multiple electronic surfaces. The model fit is also presented as lines in Fig.4.8. As can be seen, the model reproduces all calculated dissociation cross sections.

State-specific dissociation rates can be calculated by integrating the dissociation cross sections, presented in Eq.4.40, over the corresponding translational energy distribution functions,

$$k_D(v, J, T) = \sqrt{\frac{8kT}{\pi\mu_{O,N_2}}} \int_0^\infty \sigma_D(v, J, E_t) \frac{E_t}{kT} \exp\Big(-\frac{E_t}{kT}\Big) \frac{dE_t}{kT}, \tag{4.42}$$

where μ_{O,N_2} is the $N_2 + O$ reduced mass and k is the Boltzmann constant. We can then obtain vibrational state-specific rates by assuming that the rotational levels follow the equilibrium distribution,

$$k_D(v, T) = \frac{\sum_{J=0}^{Jmax(v)} k_D(v, J, T) g_n (2J + 1) \exp\left(-E_{rv}(v, J)/kT\right)}{\sum_{J=0}^{Jmax(v)} g_n (2J + 1) \exp\left(-E_{rv}(v, J)/kT\right)}, \tag{4.43}$$

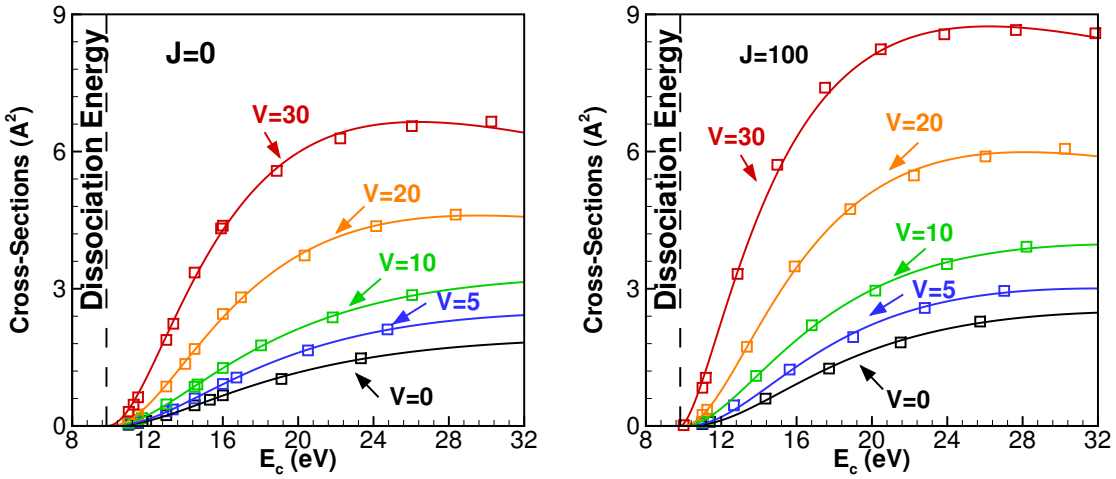

(a) $J = 0$ (b) $J = 100$

Figure 4.8. Comparison of $N_2(v, J) + O \rightarrow 2N + O$ dissociation cross sections from the QCT-SSD model (shown by lines) and QCT calculations (shown with squares) for initial vibrational levels between 0 and 30

Table 4.2. QCT-SSD dissociation model coefficient $A(v, J)$ (in A^2)

	Rotational Level				
Vibrational Level	0	20	50	100	150
0	13.6954/3	3.8612/3	8.8992/3	32.0071/3	22.7469/3
1	15.9766/3	16.6928/3	10.1433/3	18.1889/3	20.5395/3
5	21.7207/3	28.8407/3	14.1536/3	43.3566/3	33.4931/3
7	17.5769/3	15.7801/3	27.7189/3	29.9199/3	45.3146/3
10	21.7649/3	23.5739/3	29.0426/3	33.5678/3	50.3760/3
15	46.4568/3	38.8535/3	47.1537/3	44.6373/3	66.0602/3
20	62.2184/3	53.2935/3	55.2718/3	71.2303/3	67.1038/3
25	58.4835/3	67.2176/3	59.4007/3	65.7182/3	76.9170/3
30	76.7714/3	70.4267/3	46.9692/3	55.4398/3	62.7420/3
50	52.5293/3	52.5709/3	56.9886/3	-	-
55	34.5883/3	33.3195/3	40.4456/3	-	-

Table 4.3. QCT-SSD dissociation model coefficient $\alpha_1(v, J)$

	Rotational Level				
Vibrational Level	0	20	50	100	150
0	-0.8562	0.1535	-0.4418	-1.1983	-0.7820
1	-0.9275	-0.9514	-0.5159	-0.7844	-0.6867
5	-0.9779	-1.1816	-0.6282	-1.3260	-0.9121
7	-0.7563	-0.6698	-1.0632	-1.0196	-1.0701
10	-0.8428	-0.9005	-1.0460	-1.0323	-1.0748
15	-1.2716	-1.1245	-1.2475	-1.0968	-1.1749
20	-1.3609	-1.2548	-1.2502	-1.3362	-1.1218
25	-1.2437	-1.3355	-1.2301	-1.2168	-1.1619
30	-1.3797	-1.3113	-1.0134	-1.0469	-0.9061
50	-0.9389	-0.9274	-0.9389	-	-
55	-0.4158	-0.3554	-0.2485	-	-

where g_n is the nuclear spin degeneracy. In general, the rotational mode equilibrates faster than the vibrational mode and the assumption in Eq.4.43 is often valid. These vibrational state-specific rates for translational temperatures between 2,500 K and 20,000 K are shown in Fig.4.9. The state-specific rates calculated directly from QCT are shown as symbols in the same figure. The rates span 20 orders of magnitude and the model reproduces the trends established by QCT calculations. The model does over predict reaction rates from low vibrational states at low temperatures; however, at these conditions the reaction is not expected to be significant.

Equilibrium dissociation rates are obtained by averaging state-specific rates over the rotational-vibrational Boltzmann distribution function,

$$k_D(T) = \frac{\sum_{v=0}^{v_{max}} \sum_{J=0}^{Jmax(v)} k_D(v, J, T) g_n (2J+1) \exp\left(-E_{rv}(v, J)/kT\right)}{\sum_{v=0}^{v_{max}} \sum_{J=0}^{Jmax(v)} g_n (2J+1) \exp\left(-E_{rv}(v, J)/kT\right)}. \tag{3.1}$$

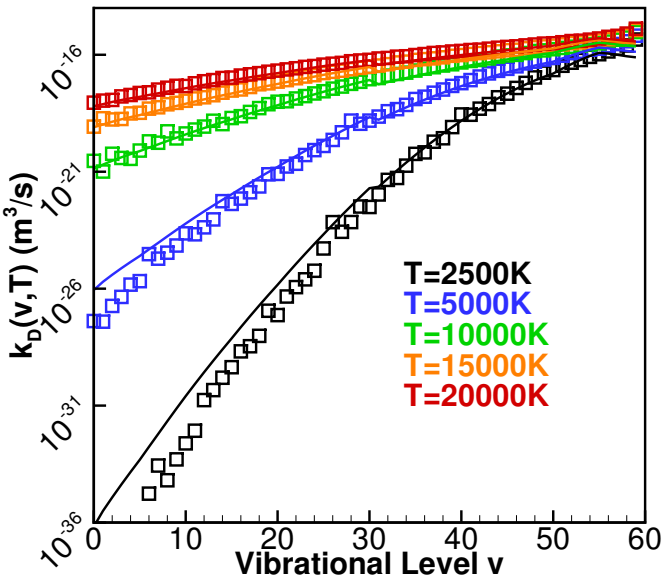

Figure 4.9. Comparison of state-specific $N_2(v) + O \rightarrow 2N + O$ dissociation rates calculated from the QCT-SSD model (shown by lines) and directly by QCT (shown with squares) for initial translational temperatures between 2,500K and 20,000K

Table 4.4. QCT-SSD dissociation model coefficient $\alpha_2(v, J)$

	Rotational Level				
Vibrational Level	0	20	50	100	150
0	2.7421	1.9663	2.4130	3.1189	2.4395
1	2.8119	2.8250	2.4530	2.6669	2.3048
5	2.8314	3.0095	2.4938	3.0070	2.4202
7	2.6106	2.5168	2.8200	2.5957	2.5188
10	2.5600	2.5917	2.6326	2.4992	2.4386
15	2.7926	2.6603	2.7038	2.4336	2.3362
20	2.7358	2.6093	2.5622	2.4924	2.0266
25	2.4224	2.5002	2.3485	2.1483	1.7466
30	2.3265	2.2610	1.9071	1.7467	1.3238
50	0.9529	0.9338	0.8428	-	-
55	0.3998	0.3449	0.1476	-	-

The equilibrium rates calculated by the model and directly from QCT are presented in Fig.4.10(a). The fitted direct-QCT calculated equilibrium rate has been shown before,

$$k_{D,\,Direct-QCT} = 2.0398 \times 10^{-13} T^{-0.4167} \exp\left(\frac{11,398\text{K}}{T}\right) \quad m^3/s \tag{3.2}$$

The relative error between the model and QCT calculations are presented in Fig.4.10(b). The model-predicted rates are within 25% of direct-QCT calculations within the entire temperature range. It should be noted that the QCT calculations have up to 40% statistical sampling noise in this temperature range. This statistical uncertainty is presented with error bars in Fig.4.10(a). Reaction rates predicted by Park [14,55] and Baulch [16] are also presented in the same figure. Keep in mind that experimental measurements for the reaction (1) are not available so current estimates are based on other rates for other species or previous theoretical work. Our calculation and

models are one order lower than the ones estimated by Park. Baulch's result is closer to QCT and QCT-SSD model's results; however, it's up to half an order higher at intermediate temperature. Nonequilibrium dissociations rates can also be obtained

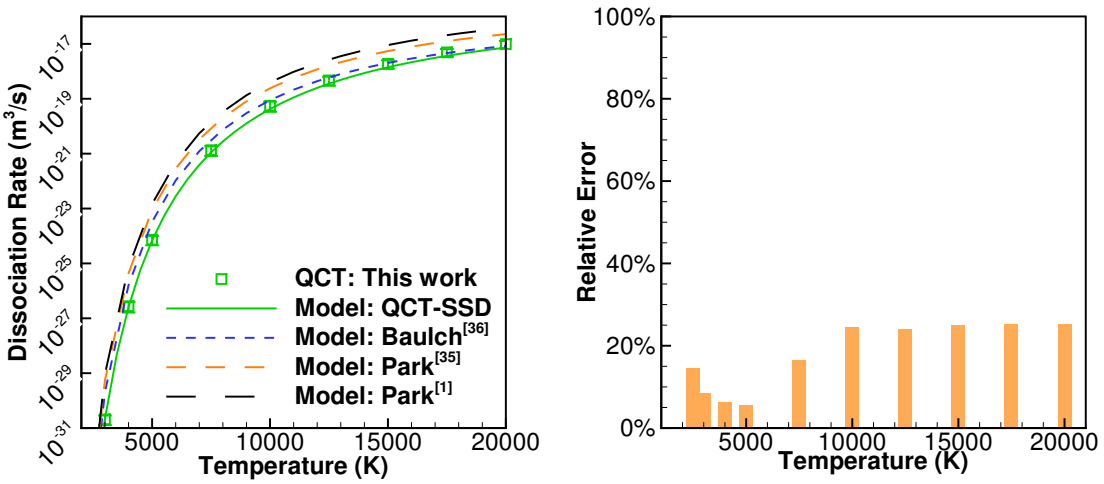

(a) Dissociation rates

(b) Model Error

Figure 4.10. Comparison of $N_2 + O \rightarrow 2N + O$ equilibrium dissociation rates calculated by the QCT-SSD model (shown with green lines), direct-QCT calculations (shown with squares) and other models by Park and Baulch

by averaging state-specific rates over a Boltzmann distribution function,

$$k_D(T, T_v, T_R) = \frac{\sum_{v=0}^{v_{max}} \sum_{J=0}^{Jmax(v)} \left[k_D(v, J, T)(2J+1) g_n \exp\left(-\frac{E_v(v)}{kT_v}\right) \exp\left(-\frac{E_{rv}(v,J)-E_v(v)}{kT_R}\right) \right]}{\sum_{v=0}^{v_{max}} \sum_{J=0}^{Jmax(v)} \left[(2J+1) g_n \exp\left(-\frac{E_v(v)}{kT_v}\right) \exp\left(-\frac{E_{rv}(v,J)-E_v(v)}{kT_R}\right) \right]} \tag{4.44}$$

with vibrational temperature, T_v that is different from translational temperature, T. The nonequilibrium factor $Z = k_D(T = T_R, T_v)/k_D(T)$ for direct-QCT calculated results and model predictions are shown in Fig.4.11 for T=5,000 K, 10,000 K and 20,000 K. The QCT-SSD model matches the QCT results perfectly for high translational temperatures or in vibrational hot ($T_v > T_t$) condition; however, the model overestimates the nonequilibrium factor for vibrational cold condition at T=5,000 K. This discrepancy is attributed to the resolution of QCT rate calculations. Although

our equilibrium rates are based on 4.9 million trajectories, each state-specific rate was calculated based on just 500 trajectories. It is difficult to use a larger number of trajectories for state-specific rate calculations because there are approximately 10,000 ro-vibrational states. As the result our QCT-calculated state-specific dissociation rates, $k_D(v, J, T)$, may be uncertain by several orders of magnitude for a few vibrational level at low temperature as shown in Fig.4.9. Even though this uncertainty is decreased in equilibrium rate calculations (because they are averaged over many ro-vibrational states), it does persist in nonequilibrium rate calculations. The minimum state-specific rate predicted by QCT-SSD model is on the order of $10^{-27}\, m^3/s$, which is much smaller than QCT resolution. Because the QCT-SSD model was fit to state-specific cross sections, it is expected to be more accurate than the direct-QCT rates shown in Fig.4.44. Better agreement can be achieved by increasing the number of sampled trajectories for low vibrational levels direct-QCT rates calculation.

Nonequilibrium factors predicted by other established dissociation models are also shown in Fig.4.44. The nonequilibrium models considered in this comparison include: the total collision energy (TCE) model [99], Macheret-Fridman (MF) model [108] and Park's model [55].

The TCE model was first proposed by Bird [99]. It assumes the reaction cross sections to be a function of the total collision energy. Thus there is no difference for the contribution to the reaction of different energy mode (translational, rotational and vibrational modes). The steric factor of the TCE model is assumed to have the following form:

$$\frac{\sigma_r}{\sigma_T} = C_1(E_c - E_a)^{C_2}\,(1 - E_a/E_c)^{\bar{\zeta}+\frac{3}{2}-\omega} \tag{4.45}$$

where σ_T is the total collision cross section modeled by variable hard sphere (VHS) or variable soft sphere (VSS) model , E_a is the activation energy ($E_a = D$ for dissociation), $\bar{\zeta}$ is average internal degree of freedom and ω is viscosity index defined in VHS/VSS model. The parameters of TCE model only depend on equilibrium reaction rate. The analytical integration Eq.3.1 of cross sections could reproduce Arrhenius form rate, which enable the model to be used in DSMC. As the original

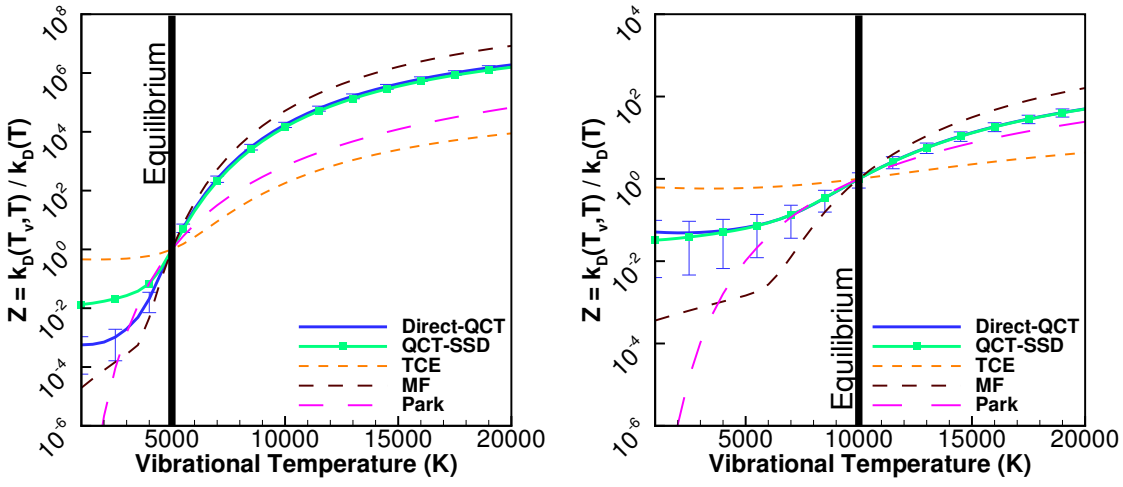

(a) $T = T_R = 5,000K$

(b) $T = T_R = 10,000K$

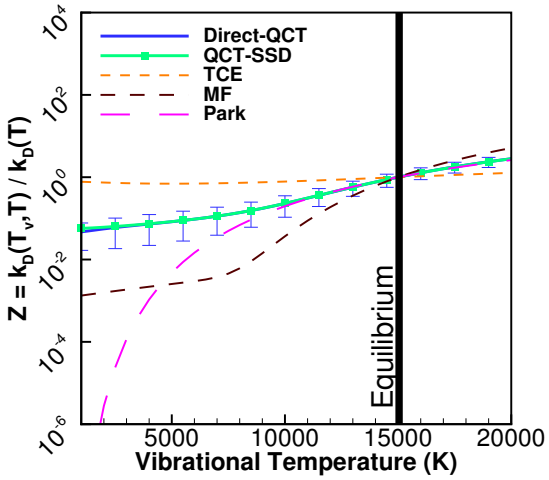

(c) $T = T_R = 15,000K$

Figure 4.11. Comparison of $N_2 + O \rightarrow 2N + O$ nonequilibrium dissociation rates calculated by QCT calculations, QCT-SSD model, discrete internal energy TCE model, Macheret-Fridman model and Park's model

TCE model assumes continuous vibrational distribution, we use Gimelshein *et al.*'s correction [106] to employ the calculated vibrational ladder in this work.

Park's two-temperature model is one of the most widely used empirical model in the nonequilibrium CFD community. It assumes the rotational mode is in equilibrium and chemical reaction rates is governed by the average temperature T_a defined as

$$T_a = T_v^s \, T^{1-s}, \tag{4.46}$$

where T_v is the instantaneous vibrational temperature and T is the translational temperature. The parameter s is chosen to be 0.5 for most cases. The reaction rate is expressed as $k_{eq}(T_a)$, where k_{eq} is the equilibrium Arrhenius rates. For the dissociation reaction $\mathrm{N_2 + O \rightarrow 2N + O}$, we use Eq.3.2. It should be noticed that Park's model is only valid for weakly nonequilibrium flow ($|T_v - T|/T \ll 1$) and has non-physical behavior for extreme vibrationally cold condition.

MF model is based on the classical solution for the atom-homonuclear molecule head-on collision with instantaneous collision approximation. It assumes the dissociation happens once the kinetic energy reaches the minimum energy barrier. The minimum energy barrier is gotten by minimizing the energy barrier of different initial molecule states and collision configurations. This model considers of two dissociation mechanisms: (1) dissociation from upper vibrational levels and (2) dissociation from lower ones; and it doesn't require additional parameters. The nonequilibrium factor of the model is as follows:

$$\begin{aligned} z(T, T_v) &= \frac{1 - \exp(-\theta/T_v)}{1 - \exp(-\theta/T)}(1 - L)\exp\left[-\frac{D}{k}\left(\frac{1}{T_v} - \frac{1}{T}\right)\right] + L\left[-\frac{D}{k}\left(\frac{1}{T_a} - \frac{1}{T}\right)\right] \\ L &= \frac{9\sqrt{\pi(1-\alpha)}}{64}\left(\frac{kT}{D}\right)^b\left[1 + \frac{5(1-\alpha)kT}{2D}\right] \\ T_a &= \alpha T_v + (1-\alpha)T, \qquad \alpha = \left(\frac{m_N}{m_N + m_O}\right)^2 \end{aligned} \tag{4.47}$$

where θ is characteristic vibrational temperature of N_2 (3,352 K) and other parameters were presented before. The detail derivation for the MF model can be found in Ref. [63, 109]. Again, we use Eq.3.2 to calibrate nonequilibrium factor of MF model.

Just as was observed earlier by Kulakhmetov *et al.* [11, 28] for the $O_2 + O \rightarrow 3O$ reaction, the TCE model significantly over predicts rates at vibrational cold condition and under predicts rates at vibrational hot condition. MF model deviates from QCT result by less than an order of magnitude for vibrational hot condition but around two orders of magnitudes for vibrational cold condition. However, this model doesn't introduce any empirical coefficients and can it can be used when state-specific data is not available. The rates predicted by Park's model continuously drops as T_V decreases. Physically, at low vibrational temperatures only ground vibrational states are populated. Therefore decreasing vibrational temperature further shouldn't significantly affect rates. At all conditions, the QCT-SSD model matches direct-QCT rates better than any other considered model.

4.2.2 State-Specifc Exchange Model

The $N_2 + O \rightarrow NO + N$ exchange reaction is the second reaction studied in this work. We also calculated exchange reaction cross sections using QCT method with translational energies ranging between 0.1 eV and 23 eV, rotational levels [0,20,50,100,150] and vibrational levels [0,1,5,7,10,20,25,30,50]. Cross-sections for all initial states, (E_t, v, J), were calculated with over 1 million trajectories. The rates were calculated directly from QCT for temperature ranging between 1,000 K and 20,000 K. A selected set of exchange cross sections are shown as square symbols in Fig.4.12. Just as with dissociation reactions, exchange cross sections show strong vibrational and rotational favoring. At low collision energies, exchange cross sections for ground vibrational states are slightly higher than for excited states but at higher collision energies ($E_c > 8$ eV) exchange cross sections for excited vibrational levels become larger. At $E_c = 10$ eV, the cross section for the $v = 30$ level are five times larger than for the ground level. A similar observation was made by Kulakhmetov *et al.* for the $O_2 + O$ exchange reaction. [28, 110] The cross sections for the $J = 100$ rotational level are also approximately twice as high as for the ground rotational level.

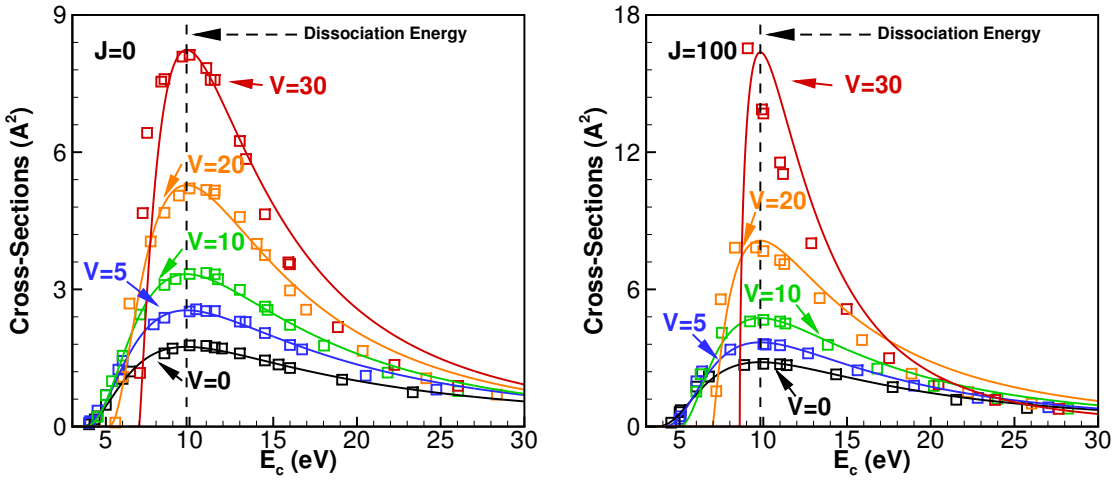

(a) $J = 0$ (b) $J = 100$

Figure 4.12. Comparison of $N_2(v, J) + O \rightarrow NO + N$ exchange cross sections from the QCT-SSE model (shown by lines) and QCT calculations (shown with squares) for initial vibrational levels between 0 and 30.

The exchange cross sections have a threshold energy, below which no exchange reactions occur. This energy is equal or larger than the energy barrier of the exchange reaction (i.e. reaction endothermicity for this case). As can be seen in Fig.4.12, this threshold tends to increase with increasing initial vibrational and rotational levels. This might be related with the O-insertion channel of reaction through MINI1-TS1 on the potential surfaces, where there is an energy barrier around 5eV. If the colliding molecules have initial rovibrational energy above the threshold then the translational energy must be larger than zero to initiate the reaction. The exchange cross sections also have a maximum when the total collision energy reaches the dissociation energy, $E_c = D$. At higher collision energies, dissociation reactions become more likely and the cross sections for the exchange reaction asymptotically decay to zero.

A new state-specific exchange (QCT-SSE) model is proposed based on the observations made in Fig.4.12. This model is similar to the dissociation model used earlier,

$$\sigma_{EX}(v,J,E_c) = \begin{cases} 0, & \text{if } E_c \le E_a(v,J) \\ A(v,J)\left[E_c/E_a(v,J)\right]^{\alpha_1(v,J)}\left[1-E_a(v,J)/E_c\right]^{\alpha_2(v,J)}, & \text{if } E_c > E_a(v,J), \end{cases} \tag{4.48}$$

however, in order for the cross sections to have a maximum at dissociation energy, D, the α_2 parameter is defined as:

$$\alpha_2(v,J) = -\alpha_1(v,J)\left[D/E_a(v,J) - 1\right]. \tag{4.49}$$

In Eq.4.48, $E_a(v,J)$ is a state-specific effective activation energy and it is an additional fitting parameter. Just as for dissociation model, D and E_c are the dissociation energy and the total collision energy. The coefficients A and α_1 and the parameter $E_a(v,J)$ are fit to each calculated ro-vibrational state (v,J) and linearly interpolated for other states. These fitted coefficients are presented in Table 4.5 through 4.7. In Table 4.5 we explicitly show that the coefficient A needs to be divided by 3. As discussed in Sec. 2.3, this division is necessary to compensate for possible nonadiabatic transitions. The model fit is compared to QCT-calculated cross sections in Fig.4.12. It can be seen there that the model reproduces the exchange cross section fairly well. The discrepancies that exist at high ro-vibrational states, like $(v,J) = (30,100)$ and high collisional energy have the relative error less 30%. These states are also less likely to exist than the ground states.

State-specific exchange rates can be calculated using Eq.4.42 and Eq.4.43. These vibrational state-specific exchange reaction rates are presented in Fig.4.13 for translational temperature ranging from 2,500 K to 20,000 K. In this figure, the rates predicted by the QCT-SSE model are shown as lines while the rates calculated directly by QCT are shown as squares. As can be seen from this figure, the vibrational state-specific rates span over 6 orders of magnitude. The QCT-SSE model reproduces rates calculated directly by QCT within half an order of magnitude error for

Table 4.5. QCT-SSE exchange model coefficient $A(v, J)$ (in A^2)

	Rotational Level				
Vibrational Level	0	20	50	100	150
0	106.6040/3	104.3597/3	108.0698/3	351.2132/3	
5	266.9474/3	259.8274/3	206.4693/3	463.3182/3	53.9792/3
7	417.9959/3	385.7538/3	305.3864/3	409.3383/3	48.7572/3
10	800.0000/3	672.3581/3	240.2589/3	196.8796/3	42.5553/3
15	800.0000/3	622.1744/3	260.5081/3	160.8333/3	37.3285/3
20	321.1994/3	269.5515/3	58.4387/3	84.0821/3	36.1900/3
25	213.5262/3	100.3110/3	44.1216/3	73.1788/3	21.1884/3
30	107.6799/3	76.4448/3	93.3640/3	88.2306/3	17.3448/3
50	80.4866/3	94.9898/3	71.1551/3	-	-

Table 4.6. QCT-SSE exchange model coefficient $\alpha_1(v, J)$

	Rotational Level				
Vibrational Level	0	20	50	100	150
0	-2.1495	-2.1276	-2.0766	-2.5219	-2.3018
1	-2.0134	-1.8961	-2.3555	-2.5117	-2.3504
5	-2.4319	-2.4155	-2.2638	-2.7787	-2.5659
7	-2.6048	-2.5582	-2.4071	-2.8969	-2.5814
10	-2.8641	-2.7715	-2.2370	-2.6994	-2.6589
15	-3.1547	-3.0446	-2.6986	-2.9661	-2.8068
20	-3.0753	-2.9859	-1.9479	-2.7587	-3.1888
25	-3.2309	-2.5819	-1.9158	-3.0487	-2.9818
30	-3.0438	-2.6741	-3.1186	-3.9082	-2.9116
50	-6.6570	-7.7534	-9.3717	-	-

Table 4.7. QCT-SSE exchange model coefficient $E_a(v, J)$ (in eV)

	Rotational Level				
Vibrational Level	0	20	50	100	150
0	3.2628	3.2630	3.2628	3.2629	6.4555
1	3.2628	3.2637	3.2628	3.2632	6.5782
5	3.2629	3.2628	3.2629	3.7551	6.9618
7	3.2628	3.2635	3.2629	4.2386	7.2907
10	3.2628	3.2629	3.3366	4.9327	7.8277
15	3.9871	4.0736	4.5092	6.0078	8.5064
20	5.0910	5.1721	5.5801	6.9790	9.1292
25	6.0918	6.1672	6.5467	7.8421	9.9821
30	6.9871	7.0568	7.4069	8.5925	10.2970
50	9.4269	9.4681	9.6689	-	-

vibrational levels between 0 and 30. As discussed earlier, the rates calculated directly by QCT are likely to have sampling noise that can be reduced by including more trajectories in rate calculations. The model does slightly under predict the rates for vibrational level ranging from 30 to 40 because cross sections for these levels were not calculated and fit to the model. QCT calculations also show that exchange rates decrease for $v > 50$, possibly because these levels are significantly more likely to dissociate. Although the QCT-SSE model does not capture this trend, the deviation is not significant since the population of the highest vibrational states is expected to be low in air flows. The QCT-SSE model also predicts a dip in reaction rates at T= 2,500 K and $v \sim 40$, which is not predicted by QCT-calculated rates. This dip is likely caused by inaccurate linear interpolation between model parameters. However, at 2,500 K vibrational levels above 30 are not likely to be excited. Therefore, the regions where the QCT-SSE model deviates from direct-QCT calculations are not expected to significantly contribute toward macroscopic flow properties.

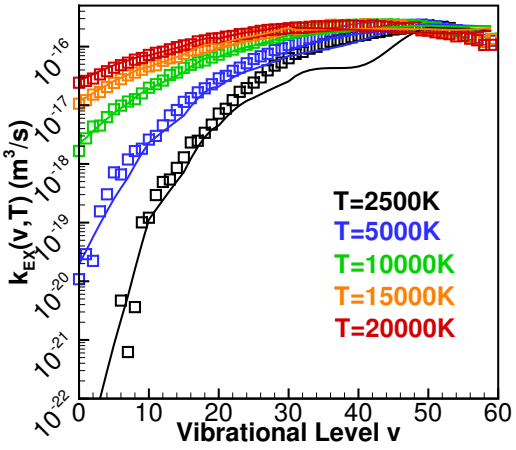

Figure 4.13. Comparison of vibrational state-specific $N_2(v) + O \rightarrow NO + O$ by the QCT-SSE model (shown by lines) abd QCT method (shown with squares) for initial translational temperature between 2,500K and 20,000K

Equilibrium exchange reaction rates are also calculated by averaging state-specific rates over the rotational-vibrational Boltzmann distribution function, as shown in Eq.3.1. Fig.4.14(a) shows a comparison between our QCT calculations, the QCT-SSE model, QCT work by other authors [22], empirical estimations [2] and experimental results [57–59]. Bose and Candler ran QCT calculations using the Walch and Jaffe's PES [36] for temperature ranging from 3,000 K to 20,000 K and fit their rates to an Arrhenius form. [23]. Livesey *et al.* studied NO formation using premixed oxypropane flames at 2,880 K. [57] Monat *et al.* obtained the equilibrium rates from shock tube experiments at temperatures of 2,384 K to 3,850 K. [58] Davidson *et al.* used a kinetic model combined with previous experimental data to estimate the rates for 2,000 K to 3,000 K. [59] Park proposed an empirical rate for arbitrary temperatures. [60] For translational temperatures below 5,000 K , both the model and QCT calculations underestimate the experimentally-computed rates by up to 94.58% but it should be noted that the experimental results do fall within the uncertainty range of QCT results. In addition, although we only consider $N_2O(1^3A'')$ PES, our results are similar to calculations by Bose and Candler's, who considered both $1^3A''$ and $1^3A'$ PESs. The Gamallo *et al.* PES used in this work includes an O-insertion mechanism, which was missing in previous calculation.

The relative error between the model and QCT calculations are also presented in Fig.4.14(b). The model is within 30% of direct-QCT calculations for temperature higher than 5,000 K. At lower temperatures, the model deviates by as much as 250%, however, at these temperatures the QCT-calculated rates have comparable sampling noise. The comparison in this temperature regime can be improved by calculating more cross sections with low translational energies, however, we focused on higher temperatures in this work.

The nonequilibrium factors $Z = k_{EX}(T = T_R, T_v)/k_{EX}(T)$ for the exchange reaction are compared in Fig.4.15 for $T = T_R$ =5,000 K, 10,000 K and 20,000 K with different models. The nonequilibrium exchange rates are also calculated using Eq.4.44. The QCT-SSE model matches direct-QCT calculations in the entire temperature

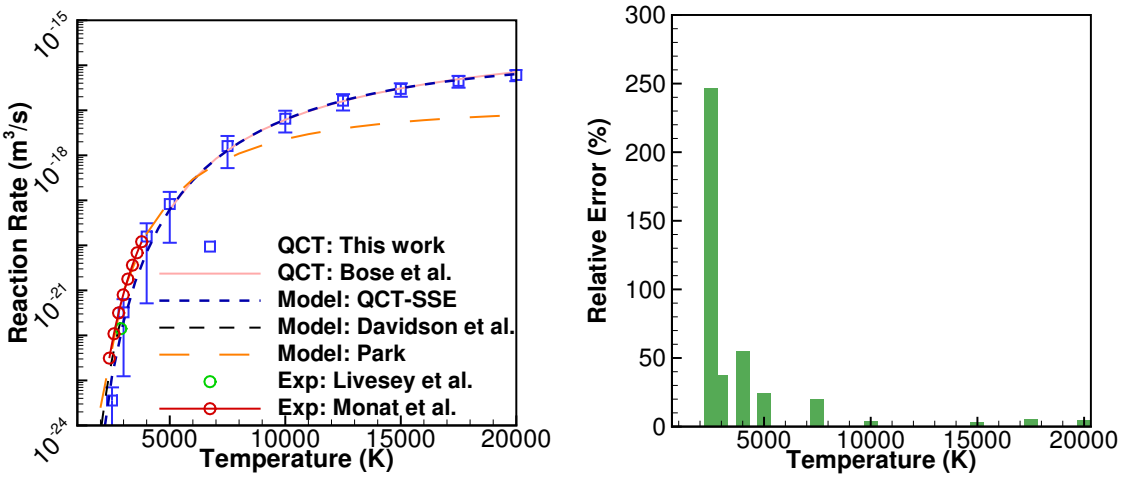

(a) Exchange rates

(b) Model Error

Figure 4.14. Comparison of $N_2 + O \rightarrow NO + N$ equilibrium exchange rates calculated by the QCT-SSE model (shown with green lines), QCT calculations (shown with squares) and other models

range. The model slightly overestimates the nonequilibrium rate at vibrational cold condition but the error falls within the QCT sampling noise. The Bose and Candler's nonequilibrium (BC) model [24] matches QCT calculations at translational temperatures above 10,000 K but it overestimates the rates at vibrational cold condition and underestimates the rates at vibrational hot condition for T=5,000 K. The TCE rate calculated by integrating TCE model cross section is also presented here. Similarly to the comparison presented for the QCT-SSD model, the TCE model overestimates exchange rates at vibrationally cold condition and underestimates them at vibrational hot condition. Within shock layers, this discrepancy would result in higher NO production rates, as was also observed by Wysong *et al.* [9].

Result predicted by Macheret's model [109,111] and Park's two-temperature model [60] are also shown here. Macheret's model for endothermic exchange reaction is based on similar threshold line theory as the dissociation model. It assumes collinear atom-molecule collisions and structureless particles. Atoms are redistributed at a time which is considerably shorter than molecular vibration period. The vibra-

tional level distribution of reacting molecules obeys the Boltzmann distribution with vibrational temperature and is not changed by reaction. For exchange reaction $\mathrm{XY + Z \rightarrow X + YZ}$, nonequilibrium factor is calculated as:

$$Z(T,T_v)\begin{cases}\exp\left[-\frac{E_a-W}{\alpha_M kT_v+(1-\alpha_M)kT}-\frac{W}{kT}+\frac{E_a}{kT}\right], & T\geq\theta\\ \left[f_v\exp\left(-\frac{\theta}{T_v}\right)+1-f_v)\exp\left(-\frac{\theta}{T}\right)\right]^{E_a/\theta}\cdot\exp\left(\frac{E_a}{kT}\right), & T<\theta\end{cases} \tag{4.50}$$

$$\alpha_M=\frac{m_Y(m_X+m_Y+m_Z)}{(m_X+m_Y)(m_Y+m_Z)},\quad W=E_a\left(1-\frac{f_v}{\alpha_M}\right)$$

where E_a is reaction heat, θ is vibrational characteristic temperature of XY and f_v is dimensionless fraction of the energy release in the reverse reaction that goes into vibrational excitation of the XY molecule (for reaction $\mathrm{N_2 + O \rightarrow NO + N}$, $f_v = 0.25$). Park's two-temperature model has been introduced in Sec.4.2.1. s is chosen to be 0.3 here. The comparison is shown in Fig.4.15. Both models are accurate near equilibrium conditions especially for Macheret's model, it predicts quite accurate result for vibrational cold condition with $T - T_v < 5,000\mathrm{K}$ at high temperature. But they deviate from our calculations at significantly cold or hot conditions. The highest deviation is found for the Park's model at vibrationally cold conditions.

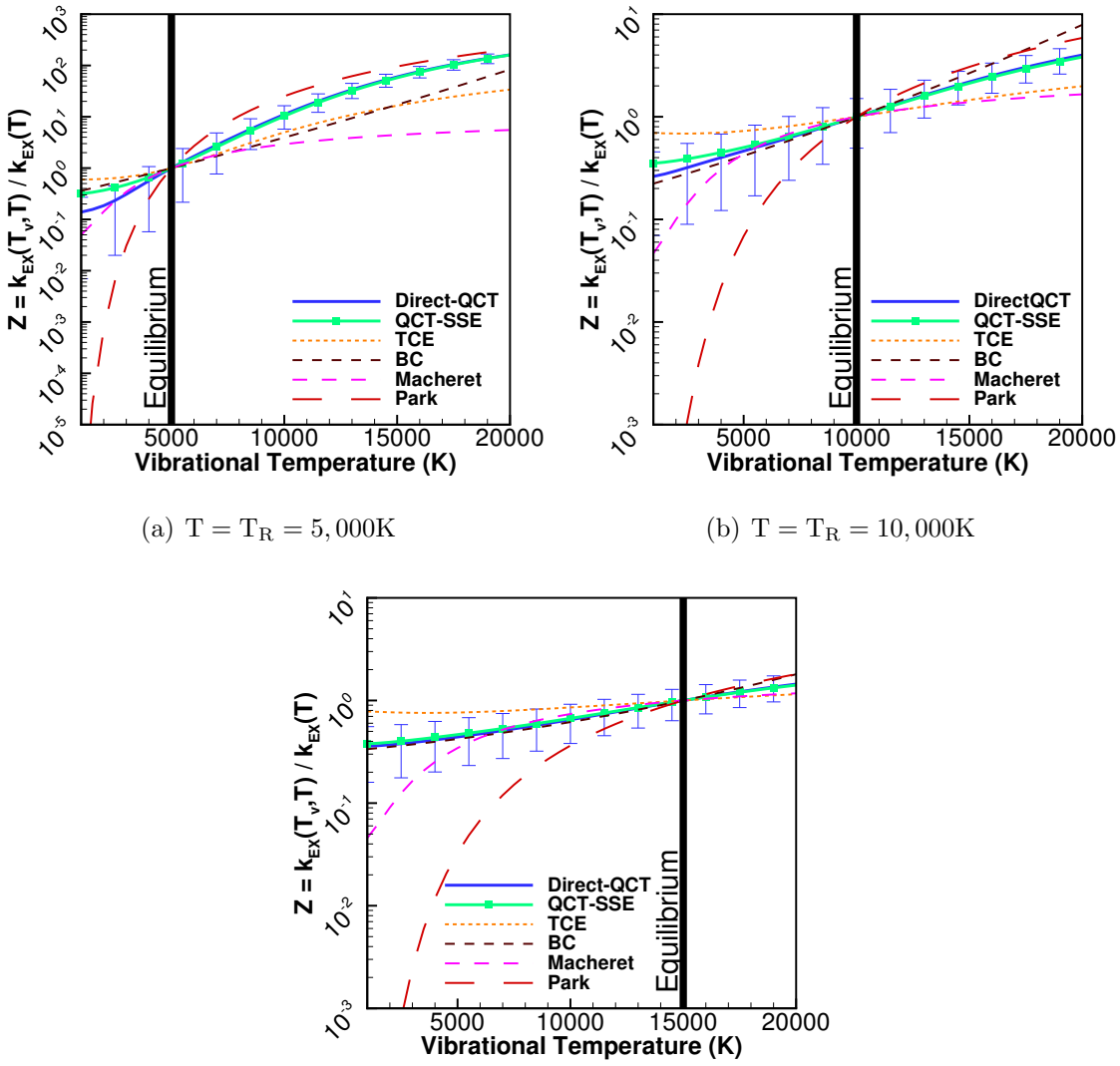

(a) $T = T_R = 5,000K$

(b) $T = T_R = 10,000K$

(c) $T = T_R = 15,000K$

Figure 4.15. Comparison of $N_2 + O \rightarrow NO + N$ nonequilibrium exchange rates calculated by QCT calculations, QCT-SSE model, discrete internal energy TCE model, Macheret-Fridman model and Park's model

5. SUMMARY

The quasi-classical trajectory (QCT) method has become an invaluable tool for studying high temperature nonequilibrium flows when experimental data are not available. Its ability to reproduce molecular collision processes, enables the understanding of potential energy surfaces' influence on chemical reaction and internal energy transition. The code developed in our group is used in this work to study nitrogen excitation/relation, $N_2(X^1\Sigma) + O(^3P) \rightarrow 2N(^4S) + O(^3P)$ dissociation and $N_2(X^1\Sigma) + O(^3P) \rightarrow NO(X^2\Pi) + N(^4S)$ exchange reactions at temperatures up to 20,000 K. Cross sections and rates are both calculated by integrating trajectories over collision orientations and geometries.

The calculated N_2 excitation/relation cross sections are used to generate ME-QCT-VT model for $N_2 + O$ system. The model uses only 11 coefficients to reproduce more than 1E4 possible VT transitions. Although the form of the model is slightly different from Kulakmetov's orginal ME-QCT-VT model for $O_2 + O$ system, it keeps the maximum entropy constraints for average vibrational energy change and vibrational favoring. It is an open topic that if these constrains hold for all atom-molecule system and the work for $N_2 + N$ system is on going. In addition, it should be noticed that electronically nonadiabatic transitions are important for VT transition. The neglect of it in QCT calculations could result in orders of difference to experimental measurements.

The $N_2(X^1\Sigma) + O(^3P) \rightarrow 2N(^4S) + O(^3P)$ dissociation reaction is calculated in this work. The calculated equilibrium rate is below previous empirical estimation. The calculated dissociation cross sections are used to generate compact state-specific dissociation (SSD) model at discrete rovibrational levels and the model coefficients are linearly interpolated at intermediate levels. The SSD model is tested by calculating state-specific, equilibrium and nonequilibrium rates from the model cross

sections and comparing these rates to those calculated directly by QCT calculations. The equilibrium rates are within 25 % of QCT calculations in the 2,500 - 20,000K temperature range. This discrepancy is within the sampling noise of the calculations.

The exchange reaction cross sections are fit to a new state-specific exchange (SSE) model. These cross sections show strong vibrational favoring and they peak at dissociation energy. When the collision energy exceeds dissociation energy, dissociation reactions cause a drop in exchange reaction cross sections. It is also shown that the cross sections of $N_2(X^1\Sigma)+O(^3P) \rightarrow NO(X^2\Pi)+N(^4S)$ reaction can not be characterized by a constant activation energy. The possible O-insertion mechanism may block the reaction at some special conditions. The QCT-SSE model is tested by comparing to state-specific, equilibrium and nonequilibrium rates. Although some discrepancies are noted in state-to-state rates, these discrepancies appear at low translational temperatures and high vibrational levels, which are not likely to exist. The equilibrium exchange rates predicted by the model and direct QCT calculations are within 30% at temperatures above 5,000 K.

REFERENCES

REFERENCES

[1] John David Anderson. *Hypersonic and high temperature gas dynamics*. AIAA, 2000.

[2] Chul Park, John T Howe, Richard L Jaffe, and Graham V Candler. Review of chemical-kinetic problems of future nasa missions. ii-mars entries. *J. Thermophys. Heat Transfer*, 8(1):9–23, 1994.

[3] Iain D Boyd. Analysis of rotational nonequilibrium in standing shock waves of nitrogen. *AIAA journal*, 28(11):1997–1999, 1990.

[4] M Karplus, RN Porter, and RD Sharma. Exchange reactions with activation energy. i. simple barrier potential for (H, H_2). *J. Chem. Phys.*, 43(9):3259–3287, 1965.

[5] Donald G Truhlar and James T Muckerman. Reactive scattering cross sections III: Quasiclassical and semiclassical methods. In R. B. Bernstein, editor, *Atom-Molecule Collision Theory: A Guide for the Experimentalist*, pages 505–566. Plenum Press, New York, 1979.

[6] M Panesi, A Munafò, TE Magin, and RL Jaffe. Nonequilibrium shock-heated nitrogen flows using a rovibrational state-to-state method. *Physical Review E*, 90(1):013009, 2014.

[7] Jae Gang Kim and Iain D Boyd. State-resolved master equation analysis of thermochemical nonequilibrium of nitrogen. *Chem. Phys.*, 415:237–246, 2013.

[8] Hao Deng, T Ozawa, and DA Levin. Analysis of chemistry models for DSMC simulations of the atmosphere of Io. *J. Thermophys. Heat Transfer*, 26(1):36–46, 2012.

[9] Ingrid Wysong, Sergey Gimelshein, Natalia Gimelshein, William McKeon, and Fabrizio Esposito. Reaction cross sections for two direct simulation Monte Carlo models: Accuracy and sensitivity analysis. *Phys. Fluids*, 24(4):042002, 2012.

[10] Tong Zhu, Zheng Li, Neal Parsons, and Deborah A Levin. State specific modeling of energy transfer in N_2-N_2 under high temperature condition. In *53rd AIAA Aerospace Sciences Meeting*, page 0477, 2015.

[11] Marat Kulakhmetov, Michael Gallis, and Alina Alexeenko. Ab initio-informed maximum entropy modeling of rovibrational relaxation and state-specific dissociation with application to the O_2+O system. *J. Chem. Phys.*, 144(17), 2016.

[12] Israel Borges Sebastiao Marat Kulakhmetov and Alina Alexeenko. Adapting vibrational relaxation models in dsmc and cfd to ab-initio calculations. In *46th AIAA Thermophysics Conference*, 2016.

[13] Paul Norman, Paolo Valentini, and Thomas Schwartzentruber. GPU-accelerated classical trajectory calculation direct simulation Monte Carlo applied to shock waves. *J. Comput. Phys.*, 247:153–167, 2013.

[14] Chul Park. Assessment of two-temperature kinetic model for ionizing air. *J. Thermophys. Heat Transfer*, 3(3):233–244, 1989.

[15] Sergey O Macheret, Mikhail N Shneider, and Richard B Miles. Energy-efficient generation of nonequilibrium plasmas and their applications to hypersonic mhd systems. 2001.

[16] Donald Leslie Baulch. Evaluated kinetic data for high temperature reactions. *Evaluated kinetic data for high temperature reactions, by Baulch, DL Cleveland, CRC Press [1972-*, 1, 1972.

[17] Deborah A Levin, Graham V. Candler, Robert J Collins, Peter W Erdman, Edward C. Zipf, and Carl L. Howlett. Examination of theory for bow shock ultraviolet rocket experiments. I. *J. Thermophys. Heat Transfer*, 8(3):447–452, jul 1994.

[18] Iain D. Boyd, Graham V. Candler, and Deborah a. Levin. Dissociation modeling in low density hypersonic flows of air. *Phys. Fluids*, 7(7):1757, 1995.

[19] Peter W Erdman, Edward C Zipf, Patrick Espy, Carl L Howlett, Deborah A Levin, Robert J Collins, and Graham V Candler. Measurements of ultraviolet radiation from a 5-km/s bow shock. *J. Thermophys. Heat Transfer*, 8(3):441–446, 1994.

[20] Devon Parkos, Alina Alexeenko, Marat Kulakhmetov, Brandon C Johnson, and H Jay Melosh. Nox production and rainout from chicxulub impact ejecta reentry. *J. Geophys. Res.*, 120(12):2152–2168, 2015.

[21] Karen F Cabell and Kenneth E Rock. A finite rate chemical analysis of nitric oxide flow contamination effects on scramjet performance. 2003.

[22] Deepak Bose and Graham V Candler. Kinetics of the N_2+O yields NO+N reaction under thermodynamic nonequilibrium. *J. Thermophys. Heat Transfer*, 10(1):148–154, jan 1996.

[23] Deepak Bose and Graham V Candler. Thermal rate constants of the N_2+O$\rightarrow$NO+N reaction using abinitio ^3A and $^3A'$ potential energy surfaces. *J. Chem. Phys.*, 104(8):2825–2833, 1996.

[24] Deepak Bose and Graham V. Candler. Simulation of hypersonic flows using a detailed nitric oxide formation model. *Phys. Fluids*, 9(4):1171–1181, apr 1997.

[25] Iain D Boyd, Deepak Bose, and Graham V Candler. Monte Carlo modeling of nitric oxide formation based on quasi-classical trajectory calculations. *Phys. Fluids*, 9(4):1162, 1997.

[26] Sinan Akpinar, Iole Armenise, Paolo Defazio, Fabrizio Esposito, Pablo Gamallo, Carlo Petrongolo, and Ramón Sayós. Quantum mechanical and quasiclassical BornOppenheimer dynamics of the reaction N_2 on the N_2O and surfaces. *Chem. Phys.*, 398:81–89, 2012.

[27] I. Armenise and F. Esposito. N_2, O_2, NO state-to-state vibrational kinetics in hypersonic boundary layers: The problem of rescaling rate coefficients to uniform vibrational ladders. *Chem. Phys.*, 446:30–46, 2015.

[28] Marat Kulakhmetov. *Upscaling Ab-initio Chemistry modes to Non-Equilibrium Flow Simulations*. PhD thesis, Purdue University, 2016.

[29] M. Hirst, D. *Potential Energy Surfaces: molecular structure and reaction dynamics*. Taylor Franci, 1985.

[30] Frank Jensen. *Introduction to computational chemistry*. John Wiley & Sons, 2013.

[31] Gabriel G Balint-Kurti and Alexander P Palov. *Theory of Molecular Collisions*. Royal Society of Chemistry, 2015.

[32] Fabrizio Esposito, Carla Maria Coppola, and Dario De Fazio. Complementarity between Quantum and Classical Mechanics in Chemical Modeling. The $H+HeH^+ \rightarrow H_2{}^+ +$ He Reaction: A Rigourous Test for Reaction Dynamics Methods. *J. Phys. Chem. A*, 119(51):12615–12626, 2015.

[33] Robert J Le Roy. LeveL 8.0: University of Waterloo Chemical Physics Research Report for Bound and Quasibound Levels. *Program*, (April), 2007.

[34] Darrel G Hopper. Ab initio multiple root optimization MCSCF study of the Cv/Cs excitation spectra and potential energy surfaces of N_2O. *J. Chem. Phys.*, 80(9):4290, 1984.

[35] Deepak Bose and Graham V Candler. Thermal nonequilibrium rates of the Zeldovich reactions. *AIAA Paper*, pages 97–0133, 1997.

[36] Stephen P. Walch and Richard L. Jaffe. Calculated potential surfaces for the reactions: $O+N_2 \rightarrow NO+N$ and $N+O_2 \rightarrow NO+O$. *J. Chem. Phys.*, 86(12):6946, 1987.

[37] P. Gamallo, Miguel González, and R. Sayós. Ab initio derived analytical fits of the two lowest triplet potential energy surfaces and theoretical rate constants for the $N(^4S)$ + $NO(X^2\Pi)$ system. *J. Chem. Phys.*, 119(5):2545–2556, 2003.

[38] P Gamallo, Miguel González, and R Sayós. Ab initio study of the two lowest triplet potential energy surfaces involved in the N (^{4}S)+ NO (X $^2\Pi$) reaction. *J. Chem. Phys.*, 118(23):10602, 2003.

[39] Wei Lin, Zoltan Varga, Guoliang Song, Yuliya Paukku, and Donald G. Truhlar. Global triplet potential energy surfaces for the $N_2(X^1\Sigma)$ + $O(^3P) \rightarrow NO(X^2\Pi)$ + $N(^4S)$ reaction. *J. Chem. Phys.*, 144(2):024309, 2016.

[40] Miquel Gilibert, Antonio Aguilar, Miguel Gonzalez, Fernando Mota, and R. Sayos. Dynamics of the $N(^4S_u)$ + $NO(X^2\Pi)$ N2($X^1\Sigma_g^+$) + $O(^3P_g)$ atmospheric reaction on the ^{3}A ground potential energy surface. I. Analytical potential energy surface and preliminary quasiclassical trajectory calculations. *J. Chem. Phys.*, 97(8):5542, 1992.

[41] Donald G Truhlar, Bruce C Garrett, and Stephen J Klippenstein. Current status of transition-state theory. *J. Phys. Chem.*, 100(31):12771–12800, 1996.

[42] Pablo Gamallo, Rodrigo Martínez, R Sayós, and Miguel González. Quasiclassical dynamics and kinetics of the N+ NO→ N_2,+ O, NO+ N atmospheric reactions. *J. Chem. Phys.*, 132(14):144304, 2010.

[43] Pablo Gamallo, R Sayós, Miguel González, Carlo Petrongolo, and Paolo Defazio. Quantum real wave-packet dynamics of the N (^{4}S)+ NO (XΠ2) →N2 (XΣg+ 1)+ O (^{3}) reaction on the ground and first excited triplet potential energy surfaces: Rate constants, cross sections, and product distributions. *J. Chem. Phys.*, 124(17):174303, 2006.

[44] Pablo Gamallo, Miguel Gonzalez, R. Sayos, and Carlo Petrongolo. Quantum wave packet dynamics of the 1 3A N (^{4}S)+ NO (X 2Π) → N2 (X 1Σg+)+ O (^{3}P) reaction. *J. Chem. Phys.*, 119(14):7156, 2003.

[45] Raphael D Levine and Richard B Bernstein. *Molecular Reaction Dynamics and Chemical Reactivity*. Oxford University Press, 1987.

[46] Andrew R Leach. *Molecular modelling: principles and applications*. Pearson education, 2001.

[47] Brian Bradie. *A friendly introduction to numerical analysis*. Prentice-Hall, 2006.

[48] AJC Varandas. Trajectory binning scheme and non-active treatment of zero-point energy leakage in quasi-classical dynamics. *Chemical physics letters*, 439(4):386–392, 2007.

[49] Graham V Candler and Robert W MacCormack. Computation of weakly ionized hypersonic flows in thermochemical nonequilibrium. *J. Thermophys. Heat Transfer*, 5(3):266–273, 1991.

[50] Fabrizio Esposito, Iole Armenise, Giulia Capitta, and Mario Capitelli. O-O_2 State-to-State Vibrational Relaxation and Dissociation Rates Based on Quasiclassical Calculations. *Chem. Phys.*, 351(1):91–98, 2008.

[51] Amy L Brunsvold, Hari P Upadhyaya, Jianming Zhang, Russell Cooper, Timothy K Minton, Matthew Braunstein, and James W Duff. Dynamics of Hyperthermal Collisions of O(^3P) with CO. *J. Chem. Phys.*, 112(11):2192–2205, 2008.

[52] Jae Gang Kim and Iain D Boyd. Thermochemical nonequilibrium modeling of electronically excited molecular oxygen. In *11th AIAA/ASME Joint Thermophysics and Heat Transfer Conference*, volume AIAA 2014-2963, 2014.

[53] David S Sholl and John C Tully. A generalized surface hopping method. *J. Chem. Phys.*, 109(18):7702–7710, 1998.

[54] Donald G Truhlar. Multiple potential energy surfaces for reactions of species in degenerate electronic states. *J. Chem. Phys.*, 56(6):3189–3190, 1972.

[55] Chul Park, Richard L. Jaffe, and Harry Partridge. Chemical-Kinetic Parameters of Hyperbolic Earth Entry. *J. Thermophys. Heat Transfer*, 15(1):76–90, 2001.

[56] HS Glick, JJ Klein, and W Squire. Single-Pulse Shock Tube Studies of the Kinetics of the Reaction N_2+O_2 →2NO between 2000–3000 K. *J. Chem. Phys.*, 27(4):850–857, 1957.

[57] JB Livesey, AL Roberts, and Alan Williams. The formation of oxides of nitrogen in some oxy-propane flames. *Combustion Science and Technology*, 4(1):9–15, 1971.

[58] JP Monat, RK Hanson, and CH Kruger. Shock tube determination of the rate coefficient for the reaction N_2+O→NO+N. In *Symp. Int. Combust. Proc.*, volume 17, 1979.

[59] N.Davidson. Selected reactions involving nitrogen and oxygen, report no. 32. Technical report, Avco Research Lab, 1958.

[60] Chul Park. *Nonequilibrium Hypersonic Aerothermodynamics*. New York: Wiley, 1989.

[61] J. P. Appleton. Erratum: Shock-Tube Study of Nitrogen Dissociation Using Vacuum-Ultraviolet Light Absorption. *J. Chem. Phys.*, 49(5):2468, 1968.

[62] Co E Treanor, JW Rich, and RG Rehm. Vibrational relaxation of anharmonic oscillators with exchange-dominated collisions. *J. Chem. Phys.*, 48(4):1798–1807, 1968.

[63] Sergey O. Macheret and J.William Rich. Nonequilibrium dissociation rates behind strong shock waves: classical model. *Chemical Physics*, 174(1):25–43, jul 1993.

[64] David A Gonzales and Philip L Varghese. A simple model for state-specific diatomic dissociation. *J. Chem. Phys.*, 97(29):7612–7622, 1993.

[65] David A Gonzales and Philip L Varghese. Evaluation of simple rate expressions for vibration-dissociation coupling. *J. Thermophys. Heat Transfer*, 8(2):236–243, 1994.

[66] L.Landau and E.Teller. Unkown. *Physik Z. Sowjetunion*, 1936.

[67] Roger C Millikan and Donald R White. Systematics of vibrational relaxation. *J. Chem. Phys.*, 39(12):3209–3213, 1963.

[68] L Pauling and EB Wilson. Introduction to quantum chemistry, 1935.

[69] Chul Park. Rotational relaxation of N_2 behind a strong shock wave. *J. Thermophys. Heat Transfer*, 18(4):527–533, 2004.

[70] D J Eckstrom. Vibrational Relaxation of Shock-Heated N_2, by Atomic Oxygen Using Ir Tracer Method. *J. Chem. Phys.*, 59(6):2787–2795, 1973.

[71] W. D. Breshears. Effect of Oxygen Atoms on the Vibrational Relaxation of Nitrogen. *J. Chem. Phys.*, 48(10):4768, 1968.

[72] E. R. Fisher. On the Quenching of O(^{1}D) by N_2, and Related Reactions. *J. Chem. Phys.*, 57(5):1966, 1972.

[73] F Esposito and I Armenise. Rovibrationally detailed cross sections of atom-diatom collisions concerning air species.

[74] M. V. Ivanov, R. Schinke, and G. C. Mcbane. Theoretical investigation of vibrational relaxation of NO($^2\Pi$),O, and N in collisions with O(^{3}P). *Molecular Physics*, 105(9):1183–1191, 2007.

[75] IWM Smith. Vibrational energy transfer in collisions involving free radicals. In *Nonequilibrium vibrational kinetics*, pages 113–157. Springer, 1986.

[76] EE Nikitin and R Stephen Berry. *Theory of Elementary Atomic and Molecular Processes in Gases*, volume 28. 1975.

[77] A. V.. Pavlov. Vibrationally excited N_2, and O_2, in the upper atmosphere: A review. *Geomagnetism and Aeronomy*, 51(2):143–169, 2011.

[78] RN Schwartz, ZI Slawsky, and KF Herzfeld. Calculation of vibrational relaxation times in gases. *J. Chem. Phys.*, 20(10):1591–1599, 1952.

[79] D. Rapp and T. E. Sharp. Vibrational Energy Transfer in Molecular Collisions Involving Large Transition Probabilities. *J. Chem. Phys.*, 38(11):2641, 1963.

[80] Igor V. Adamovich, Sergey O. Macheret, J. William Rich, and Charles E. Treanor. Vibrational Relaxation and Dissociation behind Shock Waves Part 1: Kinetic Rate Models. *AIAA journal*, 33(6):1064–1069, 1995.

[81] Sergey O. Macheret and Igor V. Adamovich. Semiclassical modeling of state-specific dissociation rates in diatomic gases. *J. Chem. Phys.*, 113(17):7351–7361, 2000.

[82] Vladimir V. Riabov. Approximate calculation of transport coefficients of Earth and Mars atmospheric dissociating gases. *J. Thermophys. Heat Transfer*, 10(2):209–216, apr 1996.

[83] Igor V. Adamovich, Sergey O. MacHeret, J. William Rich, and Charles E. Treanor. Vibrational Energy Transfer Rates Using a Forced Harmonic Oscillator Model. *J. Thermophys. Heat Transfer*, 12(1):57–65, 1998.

[84] Igor V Adamovich. Three-Dimensional Analytic Model of Vibrational Energy Transfer in Molecule-Molecule Collisions. *AIAA Journal*, 39(10):1916–1925, oct 2001.

[85] Igor V. Adamovich and J. William Rich. Three-dimensional nonperturbative analytic model of vibrational energy transfer in atommolecule collisions. *J. Chem. Phys.*, 109(18):7711, 1998.

[86] Igor V Adamovich. Three-dimensional analytic probabilities of coupled vibrational-rotational-translational energy transfer for dsmc modeling of nonequilibrium flows. *Phys. Fluids*, 26(4):046102, 2014.

[87] Divyakant Agrawal, Philip Bernstein, Elisa Bertino, Susan Davidson, Umeshwar Dayal, Michael Franklin, Johannes Gehrke, Laura Haas, Alon Halevy, Jiawei Han, et al. Challenges and opportunities with big data. *CRA white paper*, 2012.

[88] Domenico Bruno, Mario Capitelli, Fabrizio Esposito, Savino Longo, and Pierpaolo Minelli. Direct Monte Carlo simulation of oxygen dissociation behind shock waves. In *36th AIAA Thermophysics Conference, AIAA paper 2003-4059*, 2003.

[89] Katsuhisa Koura. Monte carlo direct simulation of rotational relaxation of nitrogen through high total temperature shock waves using classical trajectory calculations. *Phys. Fluids*, 10(10):2689–2691, 1998.

[90] Paolo Valentini, Thomas E Schwartzentruber, Jason D Bender, Ioannis Nompelis, and Graham V Candler. Direct simulation of rovibrational excitation and dissociation in molecular nitrogen using an ab initio potential energy surface. In *53rd AIAA Aerospace Sciences Meeting, AIAA Paper 2015–0474*, 2015.

[91] Domenico Bruno, Aldo Frezzotti, and Gian Pietro Ghiroldi. Oxygen transport properties estimation by classical trajectory–direct simulation Monte Carlo. *Phys. Fluids*, 27(5):057101, 2015.

[92] I Procaccia and RD Levine. Vibrational energy transfer in molecular collisions: An information theoretic analysis and synthesis. *J. Chem. Phys.*, 63(10):4261–4279, 1975.

[93] Sriram Doraiswamy, J Daniel Kelley, and Graham V Candler. Analysis of chemistry-vibration coupling in diatomics for high enthalpy nozzle flows. In *48th AIAA Aerospace Sciences Meeting*, pages 2010–1570, 2010.

[94] Sriram Doraiswamy, J Daniel Kelley, and Graham V Candler. Generalized chemistry–internal energy coupling model using prior recombination distribution. *J. Thermophys. Heat Transfer*, 27(3):382–390, 2013.

[95] PM Marriott and JK Harvey. New approach for modelling energy exchange and chemical reactions in the direct simulation monte carlo method. In *Rarefied Gas Dynamics*, volume 1, pages 784–791, 1991.

[96] Michael A Gallis and John K Harvey. Maximum entropy analysis of chemical reaction energy dependence. *J. Thermophys. Heat Transfer*, 10(2):217–223, 1996.

[97] Michael A Gallis and John K Harvey. The modeling of chemical reactions and thermochemical nonequilibrium in particle simulation computations. *Phys. Fluids*, 10(6):1344–1358, 1998.

[98] Lev Davidovich Landau, Evgenii Mikhailovich Lifshitz, JB Sykes, John Stewart Bell, and ME Rose. Quantum mechanics, non-relativistic theory. *Physics Today*, 11:56, 1958.

[99] Graeme Austin Bird. *Molecular Gas Dynamics and the Direct Simulation of Gas Flows*. Clarendon, 1994.

[100] Ingrid J. Wysong, Rainer a. Dressler, Y. H. Chiu, and Iain D. Boyd. Direct Simulation Monte Carlo Dissociation Model Evaluation: Comparison to Measured Cross Sections. *J. Thermophys. Heat Transfer*, 16(1):83–93, 2002.

[101] W Miller. *Dynamics of molecular collisions*, volume 2. Springer Science & Business Media, 2013.

[102] Chonglin Zhang and Thomas E Schwartzentruber. Consistent implementation of state-to-state collision models for direct simulation Monte Carlo. *AIAA Paper*, 866, 2014.

[103] Daniil A Andrienko and Iain D Boyd. Master equation study of vibrational and rotational relaxations of oxygen. *J. Thermophys. Heat Transfer*, pages 1–20, 2016.

[104] Marat Kulakhmetov. Development of a reduced C_3 NEQAIR radiation model based on ab-initio calculations. Technical Report ARC-E-DAA-TN26173, NASA, 2015.

[105] Marat Kulakhmetov, Michael Gallis, and Alina Alexeenko. Entropy considerations in ab initio modeling of rovibrational relaxation and state-specific dissociation; with application to the O_2+O system. *Submitted to J.Chem. Phys.*, 2015.

[106] SF Gimelshein, NE Gimelshein, DA Levin, MS Ivanov, and IJ Wysong. On the use of chemical reaction rates with discrete internal energies in the direct simulation monte carlo method. *Phys. Fluids*, 16(7):2442–2451, 2004.

[107] GA Bird. Setting the post-reaction internal energies in direct simulation monte carlo chemistry simulations. *Phys. Fluids*, 24(12):127104, 2012.

[108] SO Macheret and A Fridman. Mechanisms of nonequilibrium dissociation of diatomic molecules. In *AIAA and ASME, Joint Thermophysics and Heat Transfer Conference, 6 th, Colorado Springs, CO*, 1994.

[109] GG Chernyi, SA Losev, SO Macheret, and BV Potapkin. Physical and chemical processes in gas dynamics: cross sections and rate constants. volume i. *Progress in Astronautics and Aeronautics*, 196:311, 2002.

[110] M Kulakhmetov and Alina Alexeenko. Calculation and sampling of quasi-classical trajectories for nonequilibrium reacting flow simulations. In *52nd Aerospace Sciences Meeting, AIAA 2014-1077*, 2014.

[111] I V Adamovich, S O Macheret, J W Rich, C E Treanor, and A A Fridman. Vibrational Relaxation, Nonequilibrium Chemical Reactions, and Kinetics of NO Formation behind Strong Shock Waves. *Molecular Physics and Hypersonic Flows SE - 5*, 482:85–104, 1996.